Interfacial fluid dynamics inspired by natural systems

Sean William Gart

Dissertation submitted to the Faculty of the

Virginia Polytechnic Institute and State University

in partial fulfillment of the requirements for the degree of

Doctor of Philosophy

in

Engineering Mechanics

Sunghwan Jung, Chair

Jake Socha

Saad Ragab

Rolf Mueller

David Dillard

December 2, 2015

Blacksburg, Virginia

Keywords: Biomechanics, fluid dynamics, lapping

Copyright 2015, Sean Willam Gart

Sean Willam Gart

(ABSTRACT)

Many natural systems interact with the interface between air and liquids on a daily basis. Plants like the lotus that have self-cleaning leaf surfaces and animals that intake fluids in a variety of ways are all examples of these systems. Plants and animals exploit interfacial fluid dynamics in a variety of ways to survive in numerous harsh environments. In this thesis, five studies, inspired by natural interactions with interfaces are presented.

The first study explores the influence of surface wettability in the dynamics of beams struck by water droplets. This study is inspired by raindrop-leaf interaction in nature. We characterize beam behavior after impact using a simple ODE and also find that a hydrophobic cantilever experiences reduced average torque over time than a cantilever with a hydrophilic surface.

In the second study we investigate the fluid dynamics of how dogs lap water with their tongue. Dogs lap because they have incomplete cheeks and cannot suck. When lapping, a dogs tongue pulls a liquid column from the bath, suggesting that the hydrodynamics of column formation are critical to understanding how dogs drink. We measured lapping in nineteen dogs and used the results to generate a physical model of the tongues interaction with the air-fluid interface. These experiments help to explain how dogs exploit the fluid dynamics of the generated column. The results demonstrate that effects of acceleration govern lapping frequency, which suggests that dogs curl the tongue to create a larger liquid column. Comparing lapping in dogs and cats reveals that, despite similar morphology, these carnivores lap in different physical regimes: a high-acceleration regime for dogs and a low-acceleration regime for cats.

In the third study how bats drink on the wing is investigated. Bats are unique in nature in that they are one of the only animals that ingest fluids during non-hovering flight. This behavior has the advantage that bats can drink and maintain flight while hunting for food. We find that bats simply extend the tongue and drag it on the water surface while flying. The bats ingest water that coats the inside of the mouth and tongue after removal from a water bath. Bats also change their wing-beat pattern to avoid hitting the water.

We investigate the crown splash instability formed when a rounded rod impacts a fluid bath. The crown splash has been widely studied; however, it has not been seen in the configuration we present. When a rounded rod impacts water, it displaces fluid, and that fluid forms a lamella that climbs up the side of the rod. Depending on the speed of impact, rod size, and other fluid parameters an instability similar to a crown splash forms. In this study, we characterize the growth of the fluid lamella along with the wavelength of the instability.

Finally, we investigate the dynamics of squeezed fluids inspired by clapping wet hands. When water splashes, numerous water droplets, rather than fluid threads, are dispersed. This squeezing motion of the hands makes the fluid in between eject and eventually break into drops. In this study, the trajectory of a rim formed by fluid squeezed between two plates is measured and captured by a theoretical model. Additionally, the spacial distribution of the rim perturbation is predicted using Rayleigh-Plateau instability theory.

This work was supported by the National Science Foundation of the United States grants PoLS #1205642 and EAPSI #1514718.

Dedicated to my family

Acknowledgments

First, I would like to express my sincere gratitude to my advisor, Dr. Sunny Jung for his excellent guidance through my undergraduate and then graduate research. Dr. Jung was always an extremely supportive, attentive, and caring advisor and I thank him for exposing me to the wonderful world of biologically inspired mechanics. I am also thankful to have learned so much about making research appealing to a general audience, making fun and effective presentations, and how to craft an elegant scaling analysis.

I would also like to thank Dr. Socha, Dr. Mueller, Dr. Ragab, and Dr. Dillard for being on my committee and providing excellent guidance. I am grateful to Dr. Socha for pushing us and asking the tough questions, providing fantastic advice and comments on our manuscript, and for the beautiful dog drinking photos. I am thankful to Dr. Mueller for helping make the bat drinking study possible by helping with my fellowship proposal and advising me at Shandong University during the summer of 2015. Also, thanks to Dr. Ragab for being an excellent instructor in each of the four of his classes I took.

I could not have completed this work without the help of many talented colleagues. First, I'd

like to thank Talia Weiss for her help taking the initial high-speed dog drinking videos. Dr. Pavlos Vlachos provided critical experimental and paper writing advice for the dog drinking and rod impact studies. Thanks to all of the undergraduate students I have worked with over the years, especially Jalil Hasanyan who was instrumental in the completion of the rod impact work. I could not have completed the bat drinking experiments without the help of Matt Bender and my lab mate Peng Zhang. Last but not least I'd like to thank my mother for bringing our dogs to campus many times and helping me film them drinking.

I would like to thank all of my friends and lab members Brian, Peng, Seong Jin, Saikat, Ehsan, Austin, Jalil, Saurabh, Gary, Yuan, Matt, Hunter, and Florent who brightened my days with lively discussions and occasional distractions from work. I especially thank Saurabh for always asking the hard questions about life (and research) and inspiring me to read many interesting papers. Thanks to Brian for helping coin our trademark graduate student phrase: "that sucks", and Peng for many Premier League discussions.

Finally, I would like to thank my family for all of there support through the years. I truly could not have done it without you and would not be the person I am today without the support and encouragement I have received. I am forever grateful and I hope I have made you proud with my achievements.

Contents

List of Figures

List of Tables

Chapter 1

Introduction

1.1 Plant and animal interaction with fluids

Plants and animals interact with fluids for hydration [1]-[12], to disperse seeds [13], to escape predators [14, 15, 16, 23, 18, 19], and to swim. Examples of the huge range of fluid use in nature include microorganism locomotion in liquid all the way to elephants spraying water from their trunks to bathe, and California redwood trees that take fluid hundreds of feet above the ground. Many animals and plants have evolved specialized behaviors and morphology to overcome challenges or take advantage of phenomena involving fluids or an air/fluid interface.

1.2 Air/water interfaces in nature

There are a huge number of natural systems that interact with the air/water interface. One of the most famous examples is the self-cleaning surface of the lotus leaf. Lotus leaves have surfaces that are covered with micro-pillars that have a hairy nano-structure that causes the surface to be super-hydrophobic [84]. Drops are unable to stick to the surface of the leaf so they roll off, taking contaminants with them. Scientists have used the Lotus leaf as a model for the production of super-hydrophobic surfaces [82].

Another natural system that has taken advantage of air/water interfacial phenomena is the splash-cup plant. Splash-cup plants have specially shaped flowers that are able to redirect incoming raindrops at speeds three to five times faster than the droplet impact speeds [13]. The plants have seeds inside of the cups that are then spread by the splash of an incoming raindrop. This type of system has implications for raindrop energy harvesters and in ink-jet printing applications.

Splashes can also be harmful, as there is a positive correlation between rainfall and foliar disease transmission. Most leaves are covered with sessile droplets rather than a fluid film. Gilet and Bourouiba [20] show that when raindrops impact leaves they can spread pathogens in different ways: by direct contact with a sessile drop on a surface or by inertial detachment when the drop induces leaf motion which then ejects the droplet from the surface.

1.3 Animals at the air/water interface

Many animals interact with an air water interface on a daily basis. One example is the archerfish that is able to shoot a jet of fluid and knock its insect prey into the water [21, 22]. The archerfish is able to automatically adjust for the index of refraction of the water to accurately strike its prey [22]. Another famous example is the Basilisk lizard or Jesus lizard that is able to run across the water surface to escape predators [23, 18]. The animals are light for their size and have specially adapted feet that allow them to quickly strike the water surface, push the foot into the water, and retract the foot out of the water before it sinks. Three forces keep the lizard above the water: the slap impulse when the foot strikes water, the drag force as the foot is pushed deeper under water, and the hydrostatic force due to the air cavity formed by the foot [24].

Some animals, like plankton, want to jump out of the water to escape predators [14, 16, 23]. Some large plankton species reside near the surface of water, are highly pigmented, and are easily seen by predators. These types of plankton escape predators by jumping out of the water. Plankton can reach jump velocities over 800 mm/s and distances of 80 mm [16]. Jumping through the air interface is much more difficult for plankton than for a large aquatic animal because there is a large amount of kinetic energy lost from surface tension yet plankton are still able to jump long distances compared to body length [16].

1.4 Objectives of investigations

Natural interaction with fluid interfaces occurs in a variety of ways as exemplified by the diverse collection of studies presented in the following sections. Interface interaction with plants in the form of droplet impact on a leaf, animal interaction with interfaces in the form of dog lapping and bat drinking on the wing, and instability problems inspired by lapping dogs and clapping hands are all investigated.

Some leaves undergo a change in surface properties over one growing season [74] and the implications of this change in terms of raindrop impact have never been investigated. Elastic cantilevers are used as a simplified leaf model and drops are released onto the beam and the beam/drop dynamics are measured. There are limited studies on droplet impact on an elastic substrate such as droplet impact on a circular membrane [96], droplets bouncing on a soap bubble trampoline [20], and measurement of the force on impacting rain [98]. This study is the first study investigating droplet/substrate dynamics on an elastic surface with changing wettability.

In the next study, we investigate how dogs use their tongue as an open pump to transport fluids into the mouth. Animals with incomplete cheeks, like cats and dogs, cannot form a seal with the mouth and suck fluids like humans. Instead, they use their tongues to transport fluid into the mouth [11, 12]. To lap, cats and dogs extend the tongue to touch the fluid surface and then quickly retract the tongue back into the mouth bringing fluid up out of the bath and into the mouth due to inertia. Cats have been observed to lightly touch the

tip of the tongue to water [11] while dogs curl their tongue backwards and occasionally fully penetrate the water surface with a scoop shaped tongue [11]. Casual observation previously led many to believe that dogs use their tongue to scoop fluids until Crompton and Musinsky [11] showed, using x-ray video, that the fluid the dog scoops falls out of the mouth back into the bath. In this study we investigate why the tongue forms this curled shape if the dogs do not actively scoop fluids. To do this, we perform an experiment with a rounded rod that mimics tongue motion to study the dynamics of the water column formed by the dogs tongue when it retracts out of water and into the mouth. Then relate the column dynamics to the frequency of lapping for a phylogenetically diverse group of dog breeds.

Bats drinking water while flying is another example of animals interacting with the air/water interface. Bats prefer to hang upside down and are vulnerable to predators if they are lying on the ground. Therefore, they prefer to drink water while flying instead of crawling to a water source. Bats generally drink when they emerge from their cave to hunt for food [25]. Flying is an energetically demanding activity and bats require a lot of hydration. and it is advantageous for them to feed over a body of water and drink at the same time. Flying while drinking is a highly unique behavior in nature. Insect feeding bats and some species of swallows [26] are some of the few animals known to drink and fly. In this study we investigate the kinematics of bats while they fly and drink and posit the mechanism in which they transport fluids into the mouth.

The next section involves an instability inspired by dog drinking. When dogs lap, they curl the tongue backwards to create a hemispherical surface. The tongue sometimes impacts

the water surface at high enough speeds to cause a splash that sticks to and travels up the front of the tongue. The tongue impact was mimicked with rounded glass rods and at high enough Reynolds numbers fluid climbed rapidly up the rod and a crown instability was formed. The dynamics of this upward jetting along with the development of the instability are investigated in the this section.

Finally, inspired by clapping wet hands, an instability produced by squeezed fluids is investigated. Many people have seen splashing by clapping hands in a pool. Fluid sqeezed by clapped hands form fluid sheets that eventually break into many droplets. Here we investigate the dynamics of the rim and sheet formed by two squeezing plates as well as the instability mechanism that breaks the sheet and rim into smaller droplets.

Chapter 2

Droplet impact on a cantilever: a leaf-raindrop system

2.1 Introduction

Leaf shedding is one of many survival mechanisms in deciduous plants to conserve water and nutrients during low-sun, dry, and cold winters [70, 71]. The abscission process starts with the formation of a thin layer of dried dead cells at the base of the leaf stem and a change in surface property to hydrophilic [72, 73]. Eventually, the leaf is separated from the stalk in response to torque induced by wind or rain. For example, oak tree leaves are hydrophobic when young but become hydrophilic due to wax-layer erosion before the end of the growing season [74]. The abscission mechanism is inadvertently triggered prematurely

in areas with high levels of air pollution, accelerating forest decline [75, 76, 77, 78, 79]. Previous studies on this topic have focused on chemical reactions and associated wax-layer degradation [78, 80, 81]. However, the dynamic response of a contaminated leaf to high-speed drop impact may clarify the direct influence of air pollution on early leaf abscission, which has yet to be understood.

Hydrophobicity of a leaf surface plays an important role in keeping the surface clean as droplets roll, collect, and remove contaminants [82, 83]; this is known as the lotus effect [84]. Most previous studies featured gently rolling drops or rigid and immobile leaves; however, in nature, raindrops hit a leaf at high speeds exhibiting drastically different dynamics as seen in Figure 2.1. To investigate leaf-drop dynamics, we simplify the natural system by modeling a leaf using an elastic cantilever beam [85]. Droplet impact dynamics on rigid surfaces has been extensively studied [86, 87, 88, 89, 90], yet droplet impact on an elastic surface has not received much attention. These impacts can be important for industrial applications like piezoelectric raindrop energy harvesters [91, 92, 93] and can have biological implications like raindrops impacting leaves [13, 95]. Though limited, there are several previous studies of droplet impact on elastic surfaces, such as the impact on a circular membrane, [96], droplets bouncing on a soap film [97], and on the force of impacting rain [98]. Droplet impact on soft polydimethylsiloxane (PDMS) surfaces has also been studied [99, 100], but there are no studies on how hydrophobic elastic surfaces respond to droplet impacts.

In this article, we investigate coupled cantilever beam and drop dynamics inspired by large raindrops impacting a leaf orthogonally near its free end (worst-case scenario in terms of

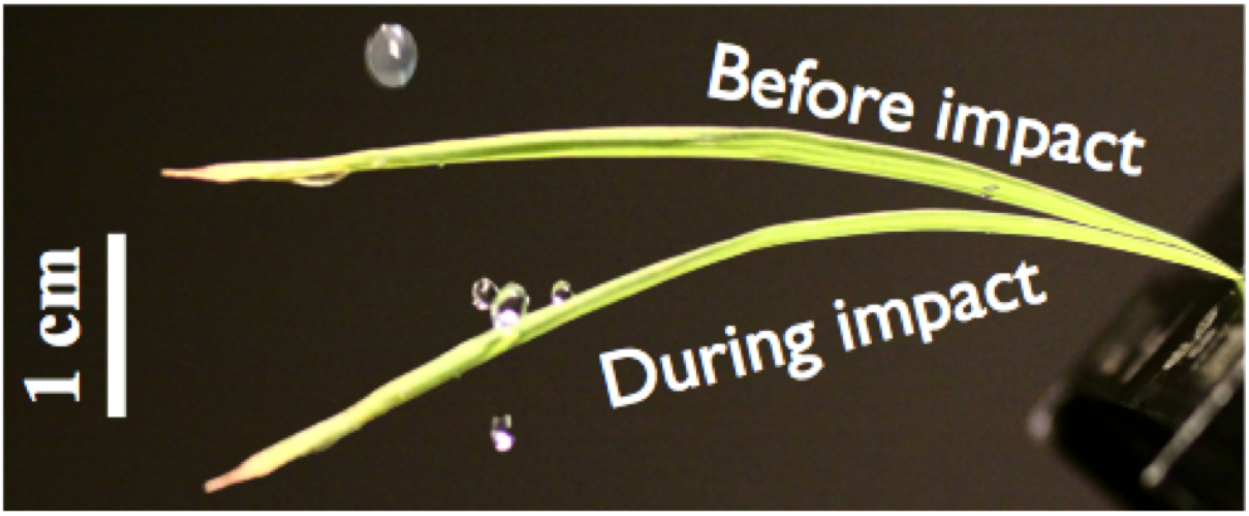

Figure 2.1: Side view of water drop impact on a natural leaf in the lab.

potential for physical damage). The high-speed dynamics of droplet impact were recorded, while the bending energy (ε), torque (τ), vibration frequency (ω), and damping ratio (ζ) of the system were measured, and a simple theoretical model was developed to explain these measurements. The results of this study can be used to understand how leaf surface wettability affects the bending energy and torque on the leaf during raindrop impact, which can cause damage and contribute to early leaf fall.

2.2 Methods and materials

Our experimental apparatus has two parts: a drop dispenser and a polycarbonate cantilever beam Figure 3.1. Water was supplied very slowly using a syringe pump and exited through a flat-tipped capillary tube producing drops of radius (R=1.73±0.04 mm) released from a height of 20 to 1300 mm, resulted in impact speeds (V) in the range 0.5 to 4.7 m/s. The drop

radius used here is at the high end of typical raindrop sizes [133, 102] and, thus, represents the worst-case scenario in terms of impact force, which scales with drop mass.

Water with surface tension $\sigma = 7.210^{-2}$ N/m is used, and a drop release height of 100 mm used for most trials produces an impact speed of about 1.3 m/s. These values give Weber numbers ($We = V^2 D/\sigma$) of O(10-1100), where ρ denotes fluid density and D drop diameter. Beam length (L) ranges from 50 to 160 mm, which is characteristic of many leaves. High-speed imaging is used to visualize droplet impacts on the beam. The elastic cantilever beam made of polycarbonate is clamped on one end, with the impact surface set at a zero angle with respect to the horizontal. The drops impact 5 mm from the beam free tip to avoid edge spilling during impact. This configuration represents another worst-case scenario for a leaf, as torque and bending energy depend on beam length and are maximized towards the free end of the beam.

Ambient air currents were minimized to reduce the deviation of impact location. For the 100 mm drop release height used in most trials ($V_{impact} = 1.31 \pm 0.04$ m/s) the impact location from the beam end varied 5.0 ± 0.323 mm, however, for a drop height of 1300 mm ($V_{impact} = 4.74 \pm 0.004$) the impact location had a greater variance (5.0 ± 3.23 mm). The maximum spreading diameter of the drop was 8.74 ± 0.79 mm at an impact speed of 1.31 m/s. For 7.75 mm-wide beams, the spreading diameter was slightly larger than the beam width, but no apparent spillage was observed from the recorded images. Spillage/splash and droplet fragmentation only occurred at high impact speeds (V_{impact} =4.74 m/s). Beams were oriented such that the droplet always impacted orthogonally on the horizontal beam surface.

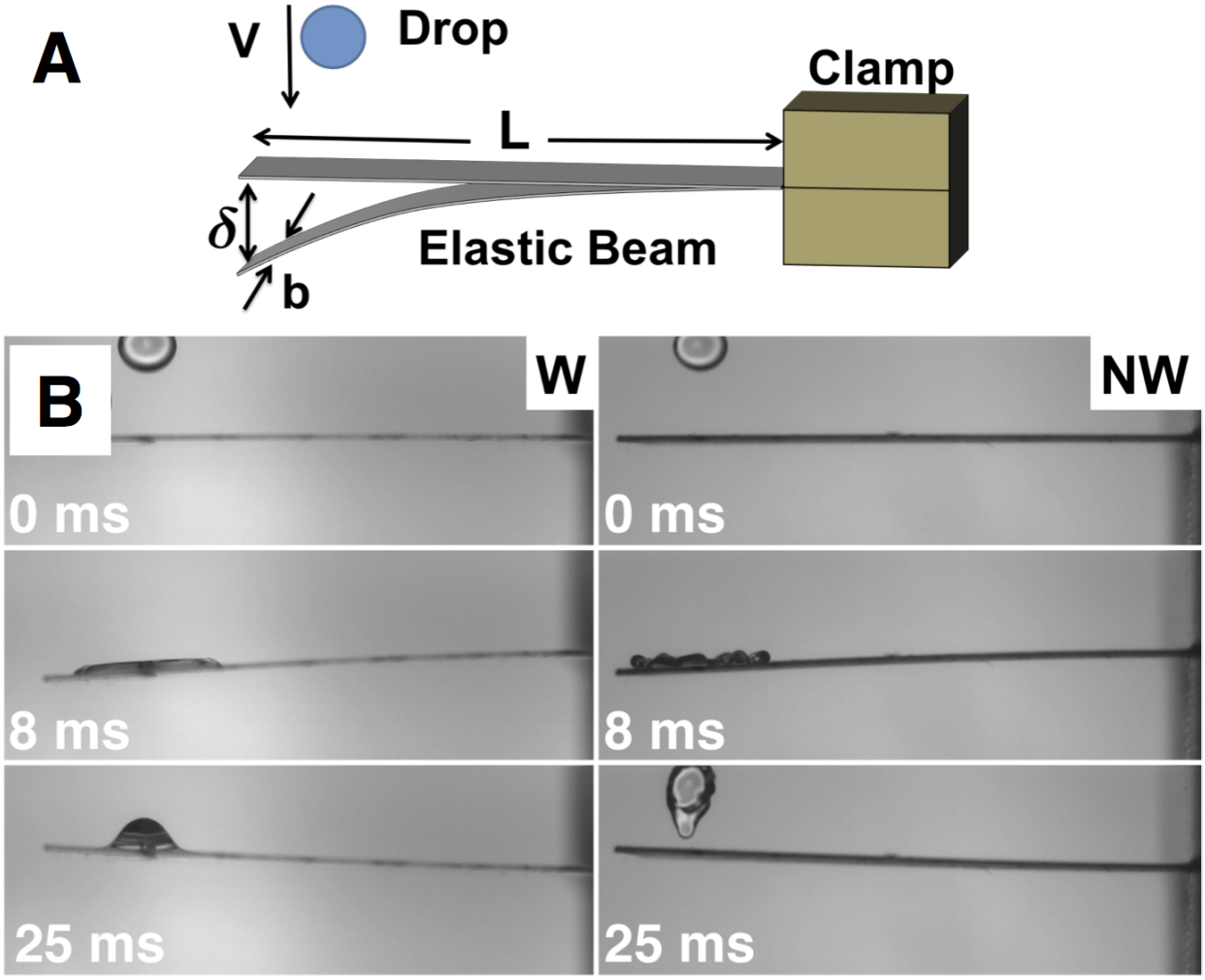

Figure 2.2: A) Schematic of the experiment setup. V denotes droplet impact velocity, δ the instantaneous beam-tip deflection, and L and b the length and width, respectively. B) Temporally captured frames during impact of a water drop on W, an 80-mm-long wettable beam and NW, an 80-mm nonwettable beam.

The wettability of the beams was changed using several different surface treatments. One group of beams tested had no surface treatment (*i.e.*, polycarbonate surface) giving sessile contact angles (θ^*) of 71.7°, another group was coated with WX-2100 hydrophobic coating from Cytonix Co giving $\theta^* \sim 153°$. Beams with $\theta^* = 82.0°$ and $= 57.7°$ were prepared via a spray-cast approach [105, 106] (Paasche VL siphon feed, 0.55 mm nozzle); coatings were composed of all poly(methyl methacrylate) (PMMA) and a 40:60 blend of SiO_2:PMMA, respectively. (SiO_2 nanoparticles, 5–15 nm, and PMMA powder, solution-processed in acetone, were both obtained from Sigma-Aldrich).

Sessile contact angles θ^* were used to label the surfaces tested and were commonly employed to denote surface affinity to liquids, but form an incomplete description of liquid wetting behavior and droplet mobility [107]. Advancing (θ^*_A) and receding (θ^*_R) contact angles were also measured to better understand droplet bouncing (hydrophobic) and adhesion (hydrophilic). An in-house goniometer was used to measure the advancing angles via a syringe-dispensed water droplet ($\approx 10\ \mu L$); receding angles were measured as the liquid was withdrawn via the same method.

When discussing surface wetting, increased surface roughness is known to amplify the intrinsic wetting behavior of any surface [108]. For example, a high-energy surface becomes more hydrophilic when texture is added. A low-energy surface becomes more hydrophobic when textured. The advancing, receding, and sessile contact angles for the untreated and coated beams are reported in Table 2.1; example images of the measurement procedure are included in Figure 2.3. With the exception of the untreated polycarbonate beams, the beams with

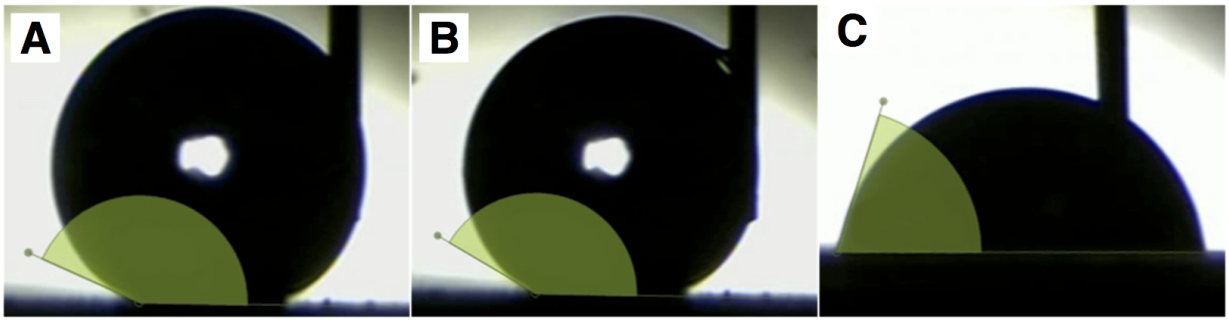

Figure 2.3: A) Advancing contact angle θ_A^* measurement on the WX-2100 treated surface, B) Receding contact angle θ_R^* measurement for the same surface. The small contact angle hysteresis, or difference between the advancing and receding angles, translates to a low adhesive force. C) θ_A^* for the PMMA:SiO_2-coated surface (θ_A^* is typically higher than θ^* since the liquid is not at equilibrium). The large hysteresis for this surface corresponds to a high adhesive force, causing droplets to "stick."

Table 2.1: Advancing (θ_A^*), receding (θ_R^*), and sessile (θ^*) contact angles for all polycarbonate beams tested (treated and untreated).

	θ_A^*	θ_R^*	θ^*
PMMA:SiO_2	75.0 ± 1.7	0.0 ± 0.0	57.7 ± 2.5
Untreated	91.3 ± 3.8	49.0 ± 2.6	71.7 ± 7.5
PMMA	91.0 ± 2.6	0.0 ± 0.0	82.0 ± 1.7
WX-2100	154.3 ± 2.1	150.0 ± 2.0	153.0 ± 3.0

$\theta^* < 82^o$ have receding contact angels of 0 due to surface morphologies causing pinning of the droplet contact line. The untreated polycarbonate beams are observed to possess an inherent receding angle of approximately 49, attributed to the smooth untextured polycarbonate surface. For the remainder of this paper, W will refer to beams on which the droplets stick, while NW will refer to beams on which the droplets bounce and fall off.

For wettable elastic beams ($\theta^* < 90°$), the drops impacted, spread and stuck to the beam; see left column of Figure 3.1B. But for non-wettable beams ($\theta^* = 153°$), the drops impacted, spread, and then fell off or bounced off the beam; see right column of Figure 3.1B. The beam continued to vibrate until damping was complete. Beam flexural rigidity (EI) values were $(2.96, 5.92, 11.61) \times 10^{-5}$ N·m^2 for beams with width (b), of 7.75, 15.5, and 30.4 mm respectively and thickness (t) of 0.25 mm, where E is the elastic modulus and I the cross-sectional inertia $I = bt^3/12$. The EI values were determined for all beams by placing a known weight on the tip of the beam and measuring tip deflection. Cross species measurement of

leaf petiole flexural rigidity has been shown to vary with length from 10^{-5} to 10^{2} Nm^2 [85], so our cantilever beams lie at the low end of natural petiole flexural rigidity.

Beam deflection was measured using Matlab image processing techniques. The images were first converted to binary so that the beam appeared as white points and the rest of the image was black. All white points in the image were found to digitize the beam along its entire length. A fourth order polynomial was then fit to the beam points and the tip position of the polynomial was recorded over time to get the beam deflection. The mean and standard deviation for droplet impact velocity at each dropping height was also calculated using Matlab image processing by tracking the position of the droplet until it impacted the beam (seen in Figure 2.4).

2.3 Experiment results

Figure 2.6a plots the beam tip position versus time for $\theta^* = 72°$ (W) and $\theta^* = 153°$ (NW) beams with lengths of 80 and 140 mm (15.5 mm width). For wettable beams, impacting droplets were observed to stick, which is consistent with the corresponding low receding contact angles θ_R^*; see Table I. As beam length increased, the mean downward deflection of the tip over time also increased. The non-wetting beams ($\theta^* = 153°$) oscillated about zero deflection, because droplets did not stick (consistent with the high receding contact angle θ_R^*; see Table 2.1).

Wetting and non-wetting trends can be explained using a simple second order differential

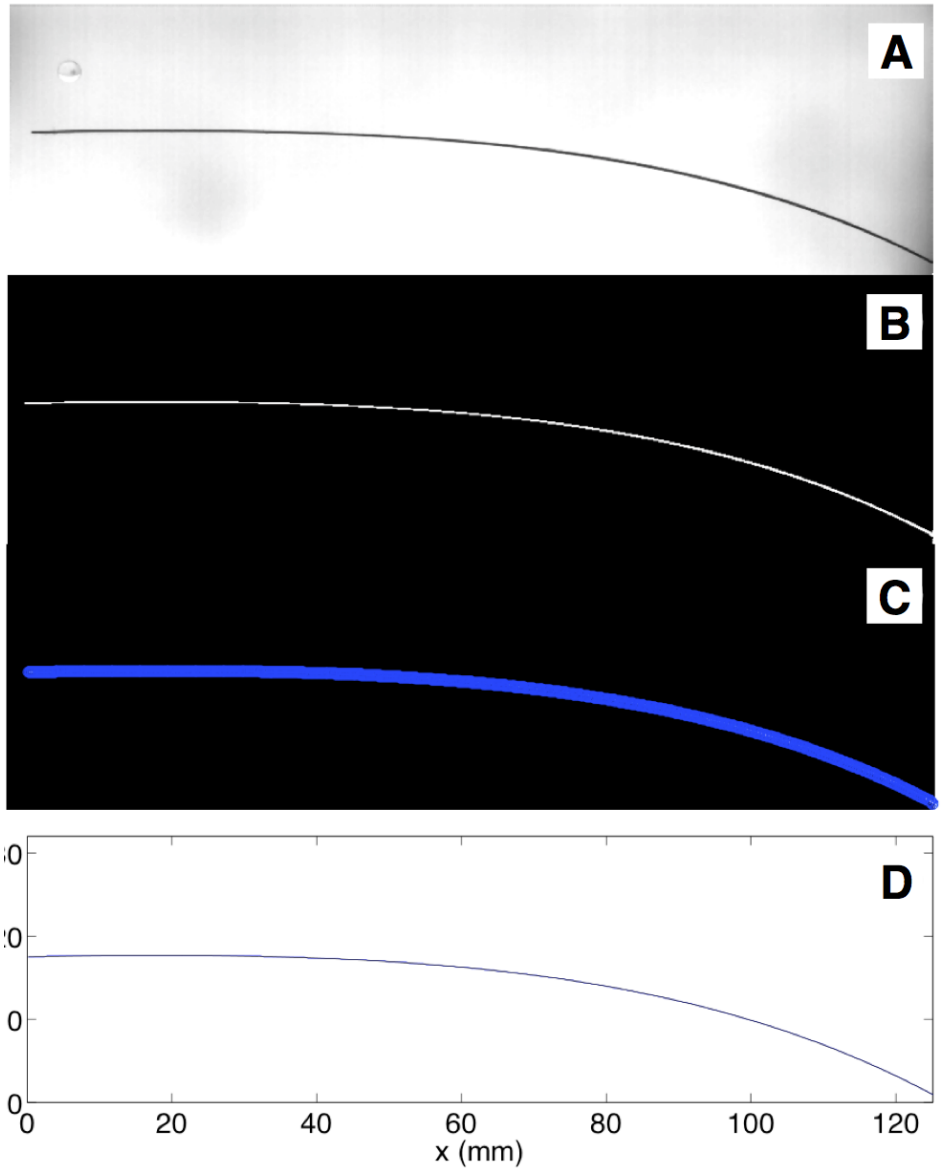

Figure 2.4: Image processing technique to calculate the beam deflection over time. A) Original unprocessed image. B) Image is thresholded to black and white. C) The beam is identified and marked with blue circles. D) A 4th order polynomial is fit to the image point data.

equation of the form

$$\ddot{\delta}(t) + 2\zeta\omega_0\dot{\delta}(t) + \omega_0^2\delta(t) = 0, \tag{2.1}$$

where $\delta(t)$ is the tip deflection of the beam, ζ the damping ratio, and ω_0 the vibration frequency. Each of these terms, as well as a solution for $\delta(t)$ will be discussed in the following paragraphs.

2.3.1 Beam Vibration

The theoretical vibration frequency can be derived from simple beam theory [103]. Start with a cantilever beam with a fixed-free boundary condition (Figure 2.5A), assume constant mass and cross-sectional inertia, and then take a short section of the beam, dx, and write the force and moment balance. Three equations arise from the free body diagram: the first equation from the force balance is

$$\frac{\partial Q(x,t)}{\partial x} + f(x,t) = m\frac{\partial^2 y(x,t)}{\partial t^2}, \tag{2.2}$$

the second equation from the torque balance is

$$\frac{\partial M(x,t)}{\partial x} + Q(x,t) = 0, \tag{2.3}$$

and the third equation from Euler-Bernoulli beam theory is

$$M(x,t) = EI\frac{\partial^2 y(x,t)}{\partial x^2}, \tag{2.4}$$

combining Equations (2.2),(2.3), and (2.4) gives

$$\frac{-\partial^2}{\partial x^2}\left[EI\frac{\partial^2 y(x,t)}{\partial x^2}\right] = m\frac{\partial^2 y(x,t)}{\partial t^2}. \tag{2.5}$$

Separation of variables can now be performed using $y(x,t) = Y(x)F(t)$. Rearranging Equation (2.5) gives

$$\frac{-1}{mY(x)}\frac{d^2}{dx^2}\left[EI\frac{d^2Y(x)}{dx^2}\right] = \frac{1}{F(t)}\frac{d^2F(t)}{dt^2} = -\omega^2. \tag{2.6}$$

Rearranging again gives

$$\frac{d^4Y(x)}{dx^4} - \beta Y(x) = 0, \tag{2.7}$$

where $\beta^4 = \frac{\omega^2 m}{EI}$. Solving for the vibration frequency gives

$$\omega_0 = \beta^2\sqrt{\frac{EI}{m_{beam}}}, \tag{2.8}$$

where m_{beam} is the beam mass per unit length and β a modal prefactor. To solve for β the

solution to Equation (2.7) is

$$Y(x) = A\sin\beta x + B\cos\beta x + C\sinh\beta x + D\cosh\beta x, \tag{2.9}$$

with boundary conditions $Y(0) = 0, Y^{'}(0) = 0, Y^{''}(L) = 0, \& \; Y^{'''}(L) = 0$. The system of equations has a nontrivial solution if

$$1 + \cos\beta L \cosh\beta L = 0, \tag{2.10}$$

which gives

$$\begin{bmatrix} \beta_1 L & = 1.8751 \\ \beta_2 L & = 4.6941 \\ \beta_3 L & = 7.8548 \end{bmatrix}. \tag{2.11}$$

The vibration frequencies of ten oak leaves (five in the spring growth season and five in the fall) are measured to compare with the current elastic beams. Leaves are collected and tested by clamping them at the end of their stem and perturbing them with a brief blow. The five leaves vary in length from 120 to 260 mm, but vibration frequencies for spring and fall leaves, respectively, are 17.15±3.02 rad/s and 31.2±7.92 rad/s corresponding to frequencies of elastic beams between 90 and 160 mm in length. Figure 2.6C shows the theoretical damping ratio (dashed line) along with the damping ratio determined from the experiments by measuring the logarithmic decay of the tip motion. A cantilever beam has several sources of damping

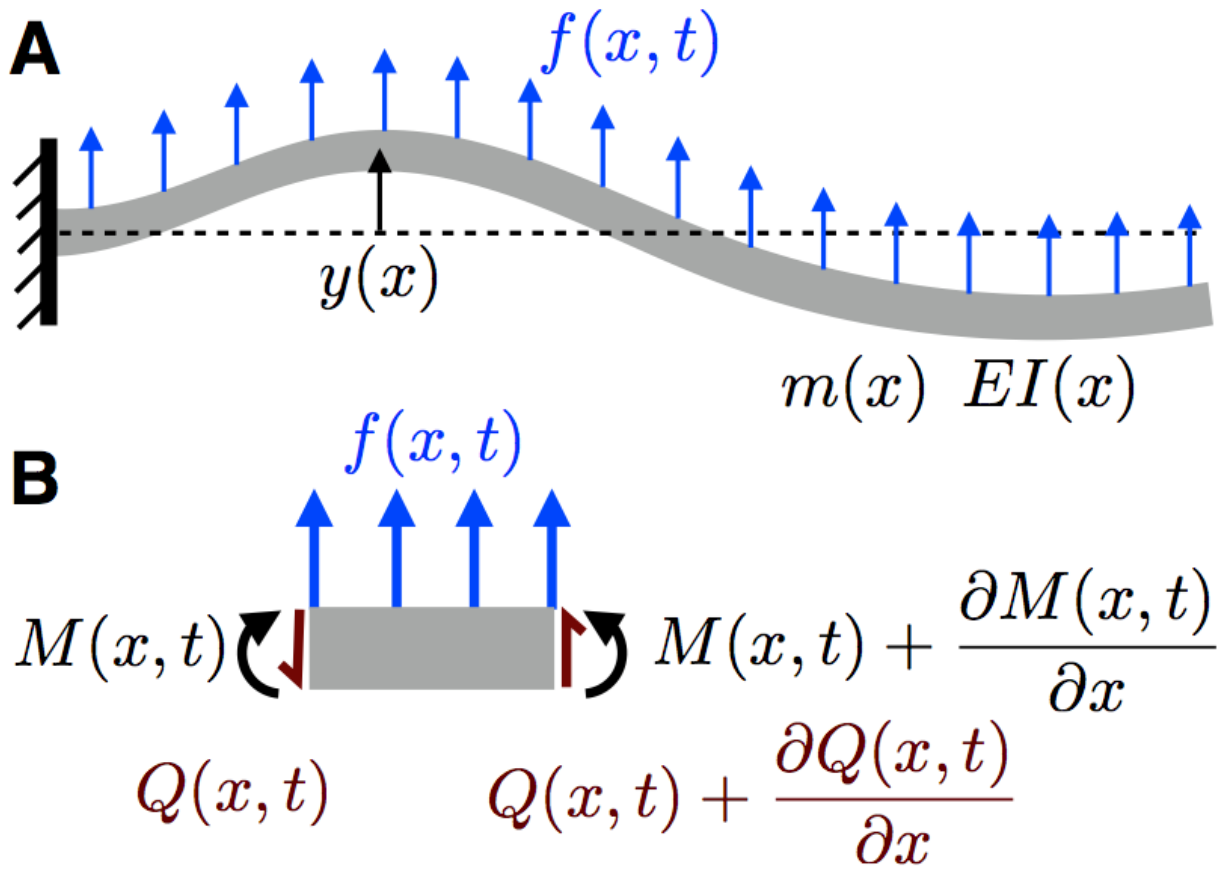

Figure 2.5: Free body diagram of a cantilever under general loading Vibration frequency (ω_0) of of each beam is calculated by averaging the time between peaks in the displacement data. All beams show good agreement with the first-mode theoretical vibration frequency shown in equation. Vibration frequency versus beam length is shown in Figure 2.6B.

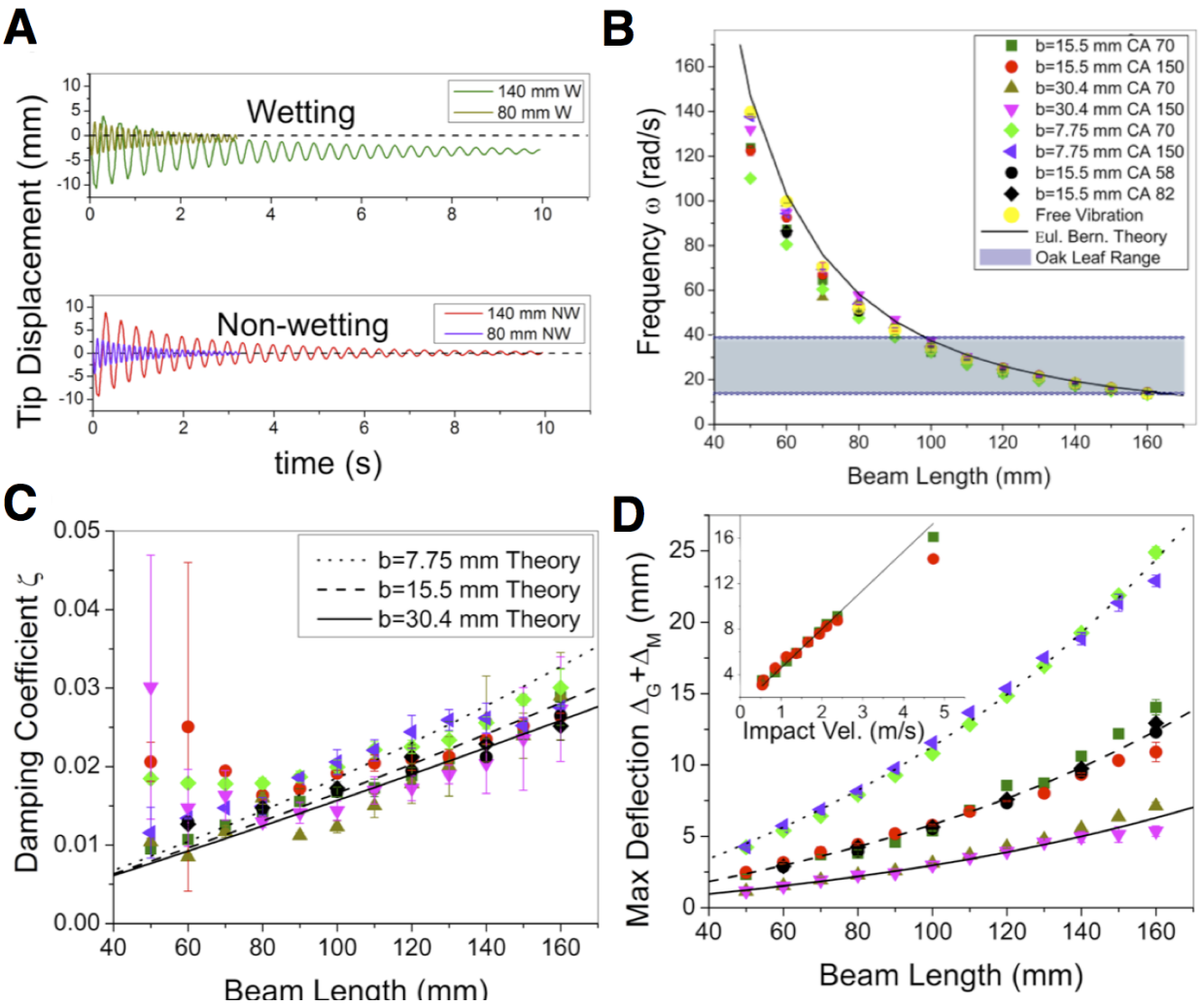

Figure 2.6: A) Beam-tip displacement versus time for 80- and 140-mm-long beams with b=15.5mm. The dashed line shows zero deflection. B) Vibration frequency versus length for beams struck by a drop, and range of measured oak leaf frequencies. Theoretical first-mode frequency is also shown (beam theory). C) Damping ratio versus beam length for beams struck by drops. The dashed and solid lines represent the theoretical ζ. D) Maximum downward deflection versus beam length. The inset plots maximum deflection versus velocity for a 100 mm beam, and the dashed and solid lines represent $\Delta_M + \Delta_G$. All symbols correspond to the legend of Figure 2.6B.

[109]: thermal, clamp, and air damping. Thermal elastic damping (TED) is defined as

$$\zeta_{TED} = \frac{E\alpha^2 T_0 \omega_0 \tau_z}{\rho_b C_p (1 + (\omega_0 \tau_z)^2)}\,, \tag{2.12}$$

where $\tau_z = \rho_b C_p t^2/(\pi^2 \kappa_{th})$, ρ_b is the beam density, C_p the specific heat, α the linear thermal expansion coefficient, κ_{th} the thermal conductivity, and ω_0 the natural frequency of the beam. Damping from the beam support follows

$$\zeta_{clamp} \propto (t/L)^3, \tag{2.13}$$

where t and L are the beam thickness and length, respectively.

For beams in this study, the air damping $O(10^{-2})$ is orders of magnitude higher than both thermal elastic damping $O(10^{-7})$ and clamp-support damping $O(10^{-5})$. To calculate the air damping ratio, the air drag on the beam must be calculated first. This can be done by approximating the beam as a series of oscillating spheres with radius $r = b/2$, where b is the beam width [110] (see Figure 2.7). The drag on the spheres is found from [111], and the air drag damping ratio is then

$$\zeta_{air} = C_\zeta \frac{3\pi\mu b + \frac{3}{4}\pi b^2 \sqrt{2\rho_a \mu \omega_0}}{2\rho_a t b^2 \omega_0}\,, \tag{2.14}$$

where C_ζ is a prefactor (in this case $C_\zeta = 3.8$), μ is the air viscosity, and ρ_a the air density. C_ζ was found by fitting the experimental data with the previous expression.

The damping ratio is determined from experiments by first calculating the logarithmic decay

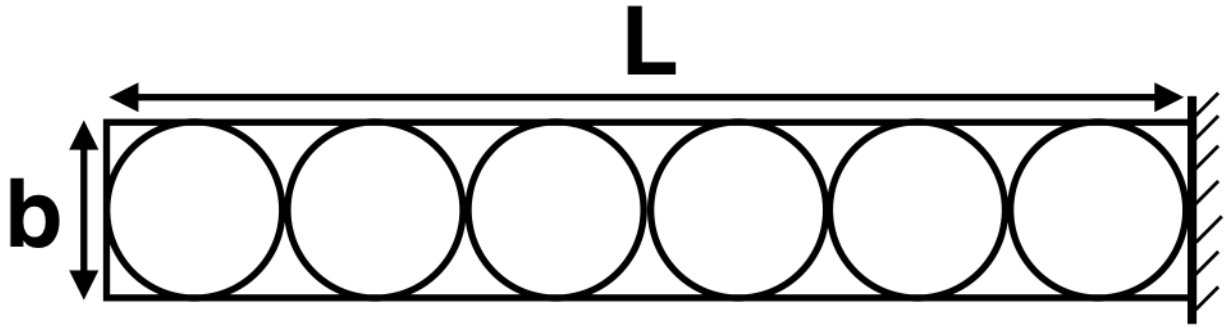

Figure 2.7: To calculate air drag the beam can be approximated using a series of spheres with radius b/2.

$$\delta = \frac{1}{p} \ln \left(\frac{a(t_q)}{a(t_{p+qT})} \right), \tag{2.15}$$

where t_q is the qth peak, T the vibration period, p the number of cycles between peaks, and a the amplitude of vibration. The damping ratio is then

$$\zeta = \delta / \sqrt{4\pi^2 + \delta^2}. \tag{2.16}$$

The predicted slope decreases as beam width increases due to a decrease in air drag for the wider beams. Experiments show good agreement with the theory, although there is considerable overlap in the error bars. The damping ratio ζ weakly depends on the length of the beam and its large variation for shorter non-wetting beams is due to the drops occasionally bouncing out of phase with the beam and quickly damping its vibration. The logarithmic decay method for calculating the experimental damping coefficient, ζ, is inconsistent when bouncing occurs.

2.3.2 Beam Deflection

We can now find the solution for deflection, Equation (2.1). For non-wettable beams, the drop bounces off of the beam, but for wettable beams, the drop sticks, meaning there is a constant downward Δ_G. Then the solutions to the equation are

$$\delta_{NW}(t) = (\Delta_M + \Delta_G)e^{-\zeta\omega_0 t}\cos(t\omega_0), \tag{2.17}$$

and

$$\delta_W(t) = -\Delta_G + (\Delta_M + \Delta_G)e^{-\omega_0\zeta t}\cos(t\omega_0), \tag{2.18}$$

where the subscript represents either non-wettable (NW) or wettable beams (W).

Δ_M is the deflection due to momentum transfer from the drop to the beam, and Δ_G is the deflection due to weight of the droplet at the end of the beam. The momentum balance between a drop and the beam at an early stage [98] shows

$$m_{drop}V = 4\Delta_M(m_{drop} + m_{beam}L/2)\frac{\omega_0}{2\pi}. \tag{2.19}$$

Then, by rearranging terms we obtain

$$\Delta_M = \frac{\pi}{2}\frac{m_{drop}}{m_{drop} + m_{beam}L/2}\frac{V}{\omega_0}, \tag{2.20}$$

where m_{drop} is the drop mass, m_{beam} the mass per unit length of the beam, and V the drop impact velocity. A simple torque balance delivers

$$\Delta_G = \frac{m_{drop} g L^3}{3EI}. \tag{2.21}$$

On a wettable surface, the drop impacts the beam causing it to move downward due to the initial momentum transfer (Δ_M), but the drop does not fall off causing a constant $-\Delta_G$. For non-wetting beams, since the drop falls off, Δ_G must be included only in the initial deflection, as the drop does not fall off until after maximum deflection is reached.

Figure 2.6D shows initial maximum deflection ($\Delta_G + \Delta_M$) of the beam versus beam length; the inset shows initial maximum deflection versus impact velocity. There is very good agreement between the model (dashed line) and experiments. It can be seen that there is no obvious difference in maximum deflection between shorter, wettable and non-wettable beams; at lengths over 120 mm, wettable beams seem to undergo a larger maximum deflection than non-wettable beams although this difference is not significant.

2.3.3 Bending Energy and Torque

After characterizing frequency, damping, and amplitudes of oscillation, we now analyze bending energy and torque of the beams. Bending (or elastic) energy is the energy stored in a material while work is being done to deform it, and can be converted to thermal or kinetic energy. For an object like a beam, the bending energy depends on the instantaneous curvature

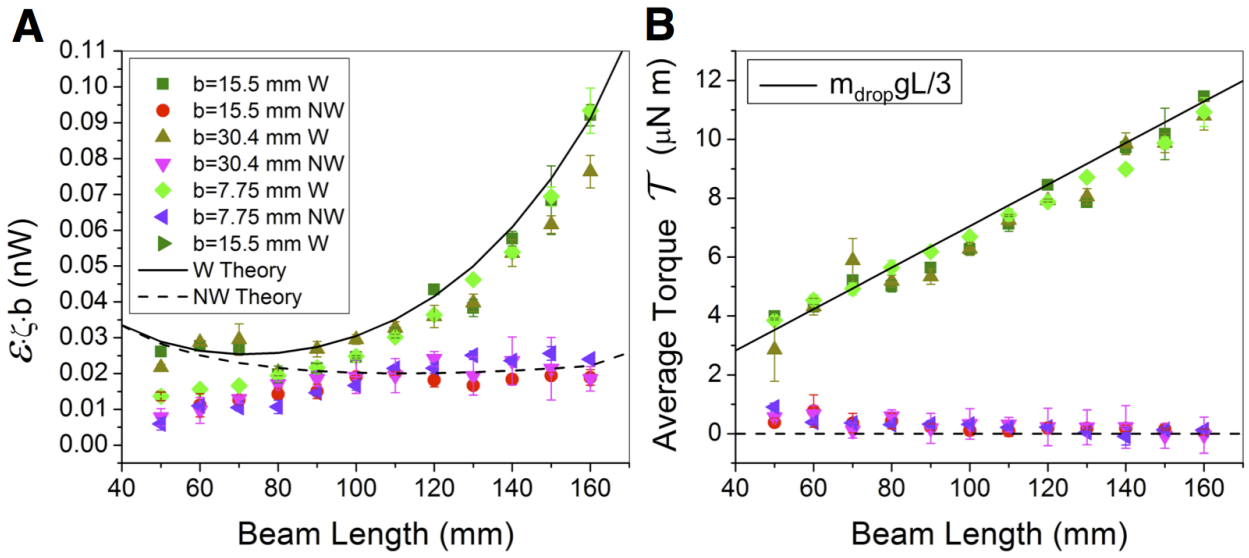

Figure 2.8: A) Measured beam bending energy multiplied by beam width b and damping ratio ζ. Theory from scaling arguments is shown with dashed (non-wetting) and solid (wetting) lines. B) Torque versus beam length for wetting (W) and non-wetting (NW) beams. The dashed line shows zero torque and the solid line shows the theoretical torque due to the droplet mass stuck to the beam.

and rigidity of the beam. If there is too much deformation, then the bending energy is not conserved and the beam, or leaf stem, can be damaged. Measuring bending energy can also offer insight on how much electrical energy could be produced by a vibrating piezo-electric beam.

The average bending energy of an elastic beam is

$$\mathcal{E} \sim \frac{1}{(t_f - t_0)} \int_{t_0}^{t_f} \frac{EI}{2} \frac{\delta(t)^2}{L^3} dt. \tag{2.22}$$

For time integration, t_0 is set at the moment of drop impact and t_f is the time required for the beam to undergo 25 vibration periods. In other words, $(t_f - t_0) = 2\pi N/\omega_0$, where N is 25. By inserting Equation (2.17) into the bending energy Equation (2.22), and if $t_f \gg t_0$, the expression for non-wetting bending energy becomes

$$\mathcal{E}_{NW} = \frac{(\Delta_M + \Delta_G)^2(\zeta^2 + 1)EI}{8t_f\omega_0\zeta L^3}. \tag{2.23}$$

For wettable beams, there is additional force from the drop mass sticking to the end of the beam and the expression for wetting displacement is seen in Equation (2.18). If we insert Equation (2.18) into Equation (2.22), the bending energy expression becomes

$$\mathcal{E}_W = (\Delta_G)^2 EI/(2L^3) - \Delta_M\Delta_G\zeta EI/(t_f\omega_0 L^3) + (\Delta_M)^2(\zeta^2 + 1)EI/(8t_f\omega_0\zeta L^3). \tag{2.24}$$

Four trials were run for each beam length, width, and impact velocity. If bending energy is multiplied by beam width b, and the damping ratio ζ, the data collapse as shown in Figure 2.8A. Regardless of beam length and width, when the drop sticks the wettable beam undergoes higher bending energy than when the drop rolls off the non-wettable beam. We also noted that for non-wettable beams, droplets fell off the beam typically after a short time ($\sim$ 160 ms) with the exception of the 50 mm-long beam where the drops did not fall off during some trials. For the 50 mm-long beams ($b = 15.5$ mm), drops tended to rebound at the same time the beam traveled back upwards after its initial deflection. This caused a

"trampoline" effect in which the drop bounced straight up and down and sometimes did not fall off.

Equations (2.23) and (2.24) are multiplied by the beam width b and damping ratio ζ and plotted in Figure 2.8A as "NW Theory" and "W Theory" respectively. The model agrees quite well with the experimental data for almost all beam lengths and widths. However, for 50-70 mm-long non-wetting beams, the experiments indicate much less bending energy than the model predicts. This is due to the droplet bouncing on the end of the beam several times and quickly damping vibration.

A tree leaf experiences torque caused by bending stresses from external forces like wind and raindrop impacts. A higher torque on a leaf means it is more likely to fail. It has been shown that the highest bending stresses occur at the base of the petiole where the leaf connects to the stem [85], so we measure the torque at the beam base where it is clamped. The average torque at the base of the beam is measured similarly to bending energy

$$\mathcal{T} \sim \frac{1}{(t_f - t_0)} \int_{t_0}^{t_f} EI \frac{\delta(t)}{L^2}\, dt. \tag{2.25}$$

The expressions for wetting and non-wetting displacement (Equations (2.17) and (2.18)) are then plugged into Equation (2.25) to deduce the theoretical torque. For the non-wetting beams Equation (2.1) oscillates about zero, hence the average torque becomes zero ($\mathcal{T}_{NW} \sim 0$). For the wettable case where the drop sticks, the torque $\mathcal{T}_W \sim m_{drop} g L/3$, which is consistent with simple cantilever beam theory. In Figure 2.8B, these trends are clearly observed. The ability of a beam to shed a drop significantly decreases the torque experienced

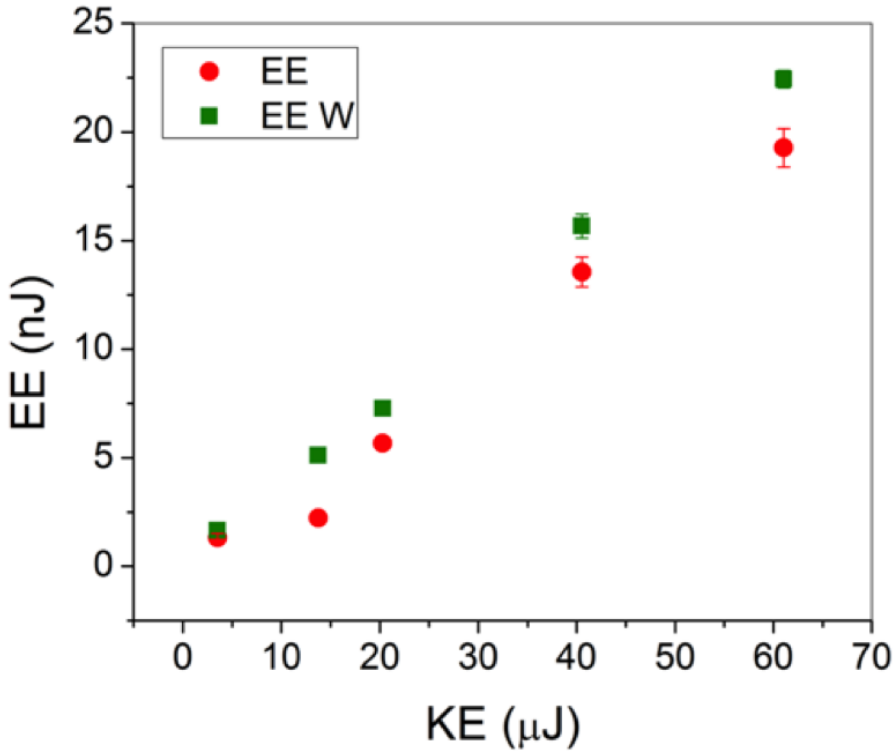

Figure 2.9: Electrical energy (EE) -as captured by a piezo-electric cantilever with either a wettable (W) or non-wetabble (NW) surface- versus drop impact kinetic energy (KE). EE is approximately one thousandth of the impact kinetic energy, a result of the energy conversion performed by the bending piezo-beam.

by the beam over time, and hence decreases potential damage from raindrop impact.

2.4 Discussion

The higher bending energy experienced by wettable beams suggests that a device intended to harvest energy from falling raindrops with a piezoelectric cantilever beam should be equipped

with a hydrophilic surface. The added mass of a drop sticking to a beam increases deflection over time and causes the beam to store more elastic (bending) energy. This was verified using a 28-mm piezo-electric cantilever beam (LDT - 028k from Measurement Specialties, Inc.). Impact velocity was varied and a piezo element with either a wetting or a non-wetting surface was used. One droplet impacting at the maximum speed produced about 23 nJ of electrical energy. Wettable piezo cantilevers produced slightly greater electric energy, especially at higher velocities, as shown in Figure 2.9.

Lastly, comparing the present bending energy and torque results to natural leaves is difficult due to the huge variation in leaf petiole stiffness and geometry found across plant species [85]. There have been limited studies on the breaking strength of a leaf petiole. One study reported a failure strength between 1.8 and 4.6 MPa for banana trees [104], which is similar to our simple tests showing failure strength between 1.5 and 3 MPa for tulip and ginko leaf petioles. The stress experienced by the beams in the present study from a single droplet impact is quite low ($\sim$ 3.5 kPa) compared to the failure strength. Naturally, it would take many droplet impacts and vibration cycles to damage the leaf petiole, therefore, fatigue tests should be performed on actual leaves to clarify the effect of increased torque on leaf petioles due to droplet impact.

2.5 Conclusion

We have performed large-droplet impact experiments on elastic cantilever beams with different surface treatments designed to modify wettability, and measured the vibration frequency, damping ratio, initial deflection, torque, and bending energy. We compared these quantities to simple theoretical models. Elastic cantilevers were used as a simple model for a natural leaf, in an attempt to elucidate whether or not leaves are protected from falling raindrops by virtue of their inherent surface properties.

We have shown that beams with a superhydrophobic ($\theta^* > 150°$) surface undergo zero average torque over time due to impacting drops bouncing and rolling off; while beams with a hydrophilic surface experience torque proportional to the drop weight and beam length due to sticking of the impacting drops. This outcome suggests that leaves with rain repellent surfaces may be better protected from falling raindrops than leaves without repellent properties. When a drop impacts a beam and sticks, the beam vibrates with a mean downward displacement that is greater than when the drop is ejected. This causes a much higher torque experienced by hydrophilic beams, even though the initial beam deflection from the drop impact is roughly the same for both cases. These findings strengthen the case for premature erosion of the leaf's wax layer as a mechanism for early leaf abscission; likely a result of environmental factors such as wind erosion and air pollution.

One interesting observation from this study that deserves a closer look is the trampoline bouncing of droplets for certain beam stiffnesses. When the droplet deformation time scale

was on the order of one quarter of the beam vibration period, droplets tended to bounce very high off of the beams. For beams with a half vibration period on the order of the droplet time scale there was minimal to no bouncing because the beam and drop motion were out of phase. The bouncing problem could be have implications for energy harvesting as it would maximize bending of the beam over several bounces. This behavior would be similar to a person jumping on a trampoline or diving board timing the jump to increase height during each jump. This work was published in Physical Review E and is titled "Droplet impacting a cantilever: A leaf-raindrop system" [145].

Chapter 3

Dogs drink using open pumping driven by acceleration

3.1 Introduction

Animals that interact with an air/fluid interface have evolved highly specialized behaviors to deal with a change in physical regime. Archerfish adjust for index of refraction when shooting water jets through the interface to catch prey [21, 22], some marine copepods leap into the air to avoid predation [14, 15, 16], and lizards and frogs run or skip across the water surface to escape predators [23, 18, 19]. However, almost all terrestrial animals interact regularly with the air-water interface when they drink or feed [1]-[12].

3.2 Animal drinking mechanisms

Due to physiological and morphological constraints animals employ a wide array of mechanisms to breach the interface and transport fluid into their bodies, including viscous dipping, capillary suction, viscous suction, licking, and lapping [8]. Animals that drink in a low Reynolds number regime, like nectar drinking humming birds and butterflies, need to overcome relatively large viscous forces [27, 28], some birds rely on contact angle hysteresis to transport droplets to the mouth [7], and cats and dogs use inertial forces generated by their tongues to transport liquid to the mouth [11, 12]. Drinking mechanisms are classified based on the principal driving and resistive forces according to Kim and Bush [28]. When an animal drinks there is a creation of a pressure difference from muscle contraction and capillarity that drives the flow combined with resistive properties like viscosity, inertia, and gravity.

Suction is the most common drinking mechanism in nature. There are two ways animals can generate suction: active suction generated by muscle contraction or capillary suction from the Laplace pressure on a curved interface. It is well known in biomechanics that an animal of characteristic size, l, can generate force, F, like $F \sim l^2$ [29]. Since the suction pressure generated by animal muscles goes like, $\Delta P \sim F/l^2$, pressure is independent of animal size. Mosquitoes [30], humans [31], and elephants [32] all generate suction pressures around 10 kPa. With this 10 kPa suction pressure, animals need to be using an extremely small drinking tube ($\sim 10\mu m$ [8]) to effectively drink using capillary pumping and thus can

raise fluids to a height of approximately 1 m.

It might make sense that animals wouldn't use capillarity since their drinking tube would need to be so small to be effective. However, butterflies are known to have pore structures in their proboscis spanning nano- and micro-scales that allow them to draw liquid into the drinking canal and then use muscular contraction to transport fluid to the head [33]. This allows butterflies to drink from irregular surfaces like rotten fruit and moist soil. Birds like the zebra finch and hummingbird [34] also use capillary suction due to geometric constraints of their beak.

A drinking strategy commonly used by nectar feeders is called viscous dipping [28]. In this method fluid is entrained on the outside of the tongue by viscosity and capillary and is used by bees, ants, and some nectar feeding bats. The amount of fluid entrained by the tongue depends on the size and extraction speed of the tongue and the thickness of the fluid layer on the tongue, $Q \sim \pi Deu$, where Q is the volume flow rate, D is the tongue diameter, e is fluid thickness, and u is tongue retraction speed. The fluid thickness depends on the capillary number $Ca = \mu u/\sigma$, where is fluid viscosity, and σ is surface tension, like $e \sim dCa^{2/3}$. Animals like lizards and rats drink using licking, a process somewhat similar to dipping. The difference is that dipping animals drink relatively high viscosity nectars that coat the tongue and licking animals drink water. This means the water layer on the tongue would be too thin for effective transport. To overcome this limitation licking animals have adapted papillae about 100 μm long that cover the tongue and trap fluid due to capillary forces [69].

The last drinking mechanism to discuss, and the focus of this paper, is lapping. For mam-

malian carnivores, their mechanism for drinking is constrained by the anatomy of their oral apparatus. Their cheeks are incomplete and they cannot form a seal to suck fluids into the mouth, and instead use the tongue to lap up fluids [8, 9, 10, 11, 12]. Lapping is a behavior that is familiar to most pet owners worldwide, but its physical mechanism is only understood in felines [11], and the underlying physics of drinking by dogs remains unexplained.

When a dog laps, the tongue first extends, and is curled backwards (posteriorly) into a ladle shape. The curled tongue impacts the liquid surface, inducing a splash. The tongue then retracts into the mouth, and the cycle is completed when the jaws snap shut. During tongue retraction, fluid adheres to the dorsal side of the tongue and is pulled upward toward the mouth, forming a water column that extends from the bath [11, 12]. Informal observations from previous studies [8, 11] have suggested that dogs scoop water with the ventral side of the tongue in the ladle, but recent X-ray imaging has shown that most of the scooped liquid falls off the tongue, and only liquid that sticks to the dorsal side of the tongue is transported to the throat [12]. Based on the lack of benefits of the curled tongue as a ladle, and general anatomical similarity, Crompton and Musinsky [12] concluded that dogs and cats share the same basic mechanism of drinking. However, the kinematics and the hydrodynamics of lapping by dogs have never been studied in detail, and it is possible that dogs and cats employ different physical mechanisms to transport liquid, despite similar morphologies. Here, we investigate the detailed hydrodynamics that enable lapping in dogs by addressing how inertial, gravitational, and surface tension forces govern the dynamics of water column formation by the tongue and the relative timing of the lapping motion.

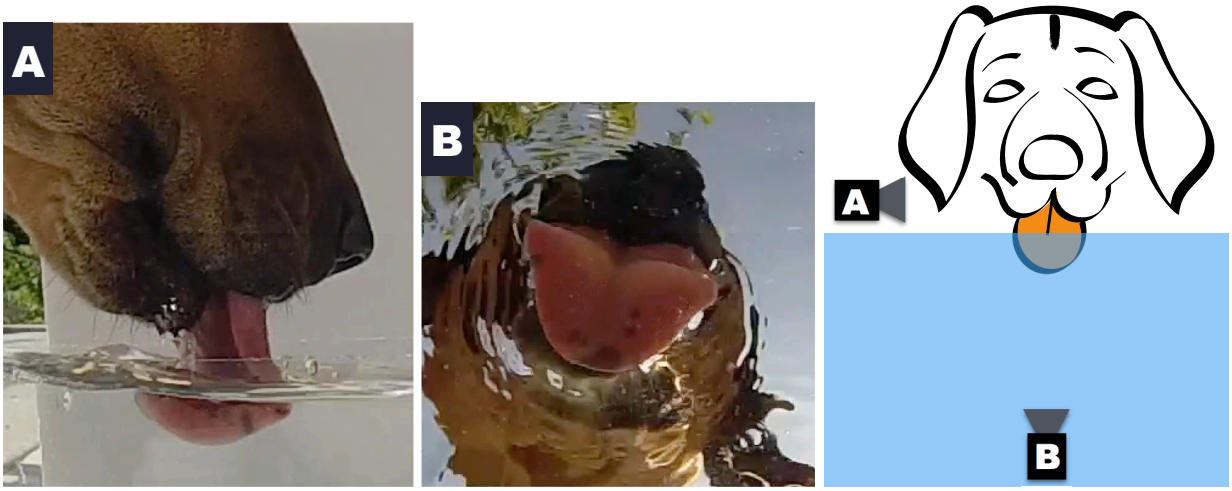

Figure 3.1: Two GoPro cameras were used to film the dogs. One camera was placed to the side (A), and the other camera was placed inside the water bowl facing upwards (B). The (A) view was used to measure tongue kinematics and the (B) view was used to measure the size of the tongue in contact with the water bath. Dogs were filmed outdoors in natural light at 120 frames/s and 720p resolution.

3.3 Measuring lapping kinematics

Nineteen dogs were filmed lapping water. Dog types included mixed and pure-bred specimens, reflecting a phylogenetically diverse sampling [35]. The owners provided the weight and breed of dogs at the time of filming. Table 3.1 shows the weight and breed and all dogs used in the study.

Dogs were filmed with two GoPro cameras at 120 frames/s during normal drinking activities. One camera was placed outside of the rectangular acrylic water container and the other beneath or in the bottom of the container as seen in Figure 3.1. No external lighting was

Table 3.1: The sex, breed, and weight of all dogs used in the study.

Number	Sex	Breed	Weight (kg)
1	F	Mixed (Boxer)	20
2	F	Mixed (Whippet)	9
3	F	Mixed (Labrador)	25
4	F	Brittany	25
5	F	Mixed (German shepherd, Belgian malinois)	35
6	F	Mixed (unknown)	14
7	M	Mixed (Labrador, pit bull)	27
8	F	Mixed (Golden retriever, poodle)	40
9	M	Mixed (Labrador, poodle)	29
10	F	Mixed (Yorkshire terrier, Bichon frise)	5
11	F	Mixed (hound)	30
12	F	Mixed (cocker spaniel, poodle)	9
13	F	Portuguese water dog	23
14	M	Rottweiler	39
15	F	Shiba Inu	9
16	M	Border collie	18
17	M	Mixed (miniature pinscher)	5
18	F	Mixed (Labrador, terrier)	20
19	M	Great dane	64

used, only natural light. 13 dogs were filmed outdoors at their owners residence and the remaining 6 were filmed outdoors on the Virginia Tech campus. If dogs refused to drink at first, they were lightly exercised by going on a five-minute run or walk with their owners and then brought back to the water container to drink. Dogs drank voluntarily or did not drink at all. No other fluid besides water was placed in the drinking container. For Figure 3.5A, a Photron APX-RS camera filmed the dog at 1500 frames/s with back lighting inside of a laboratory at Virginia Tech. Only two dogs were filmed with the Photron camera.

We hypothesized that tongue size and kinematics should vary with lapping performance. The motion of the tongue and its relevant dimensions of contact with the surface were measured. Image processing techniques were used to quantify the tongue motion, and tongue contact size was measured as the projected geometric radius (inset of Figure 3.2), $R = 1/2\sqrt{L_1 L_2}$, onto the water surface, which ranged from 12 to 20 mm. Tongue radius scaled isometrically with body mass, ($R \sim M^{1/3}$); Figure 3.2).

Tongue length was measured as the straight-line distance from the mouth opening to the anterior-most point of the curled tongue (Figure 3.3). The bottom of the curved part of the tongue was chosen as the end point because it remained in contact with the water throughout the lap and is analogous to the bottom tip of the rod. Motion of the tongue was measured by digitizing two points on each frame and measuring the distance between them until the tongue was no longer visible in the mouth. Once the tongue passed the mouth opening, which was defined by a line drawn between the nose and the tip of the bottom of the jaw, it was considered to have positive length so that there is a positive tongue velocity when the tongue

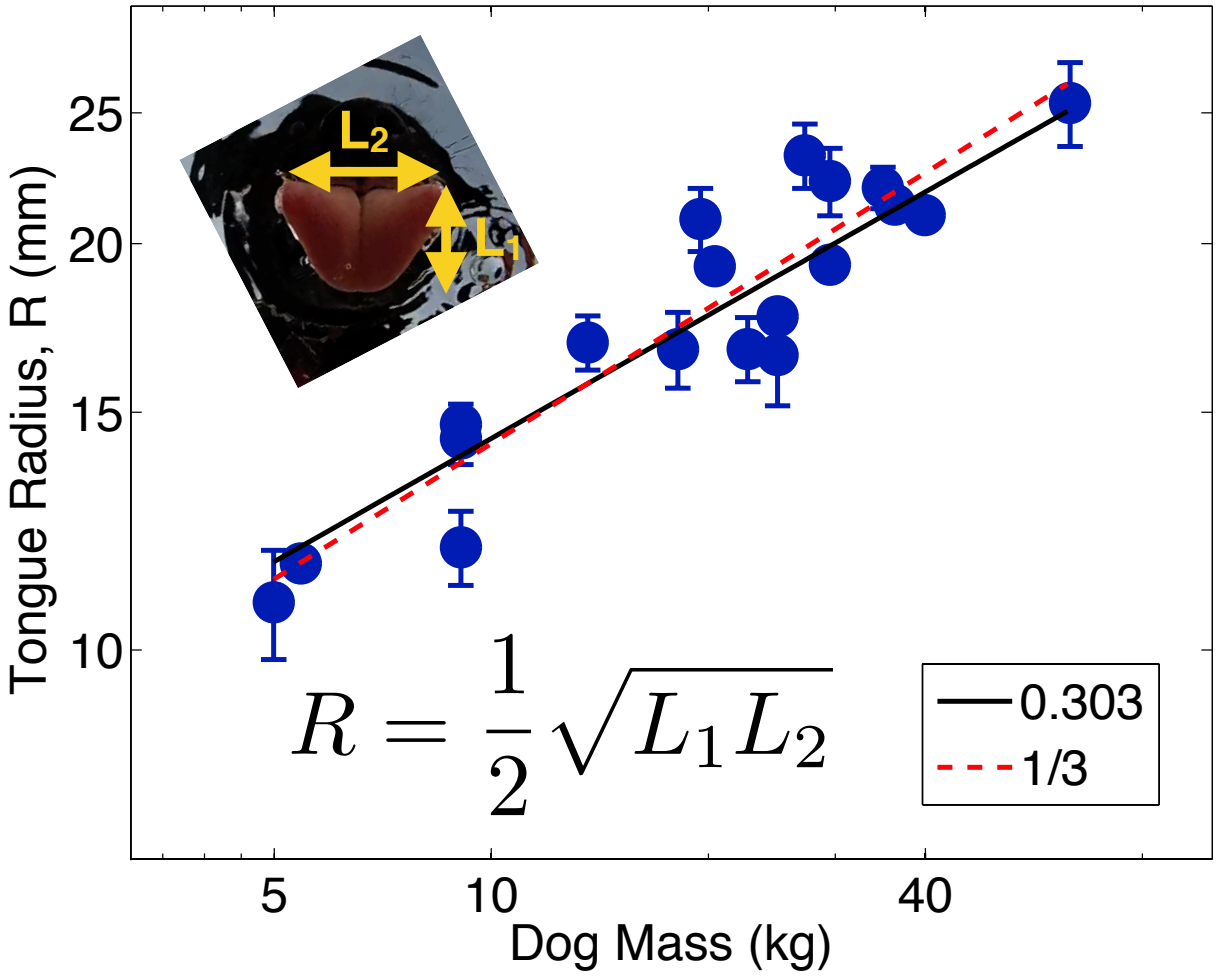

Figure 3.2: The tongue radius scaled as $R \sim M^{0.303}$ (black line) with 95% CI of the slope of 0.077 (n=19). Therefore, we assume that the tongue scales isometrically ($R \sim M^{1/3}$, red dotted line). The effective tongue radius (a proxy for tongue size) was calculated as one-half the square root of the width (L_2) multiplied by the height (L_1).

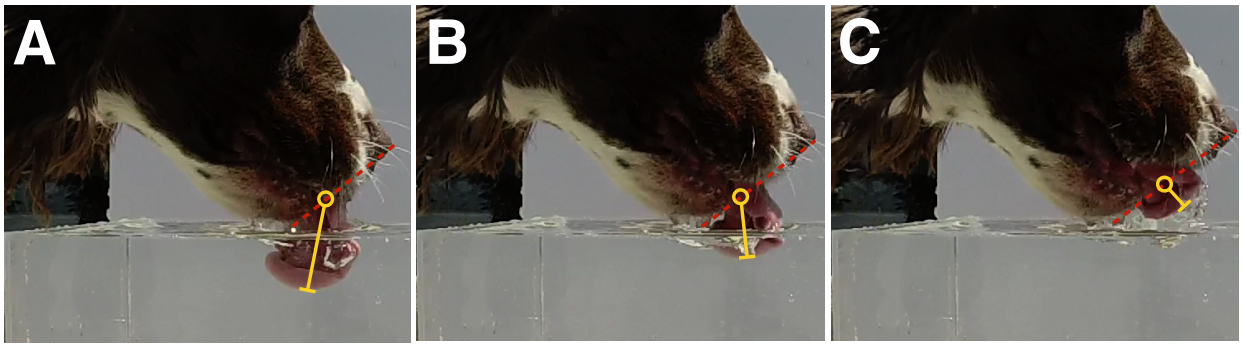

Figure 3.3: The yellow line shows how tongue length is measure for three frames of drinking. The red dashed line drawn from the tip of the nose to the bottom jaw was used to define a zero tongue length. Once the tongue passes the red line into the mouth it is said to have a positive length. This is done so that there is a positive velocity when the tongue is moving upward and into the mouth. The part of the rounded tongue that is furthest from the jaw opening is chosen for the length, as it is analogous to the rod tip.

is moving up into the mouth. Instantaneous tongue velocity was calculated as the difference in length between successive frames. To find tongue acceleration a first order polynomial function is fitted to the velocity data using least squares regression. The function is fit from the minimum velocity (when the tongue is at full extension) to the maximum velocity (as the tongue enters the mouth). This slope fitting is done to avoid potentially large errors that occur from numerical differentiation [36]. Tongue length and velocity versus time for all dogs can be seen in Figure 3.4.

Plots of tongue length and velocity through a lapping cycle for representative large and small dogs are shown in Figure 3.5B-C, which show that the dog extends its tongue into the water

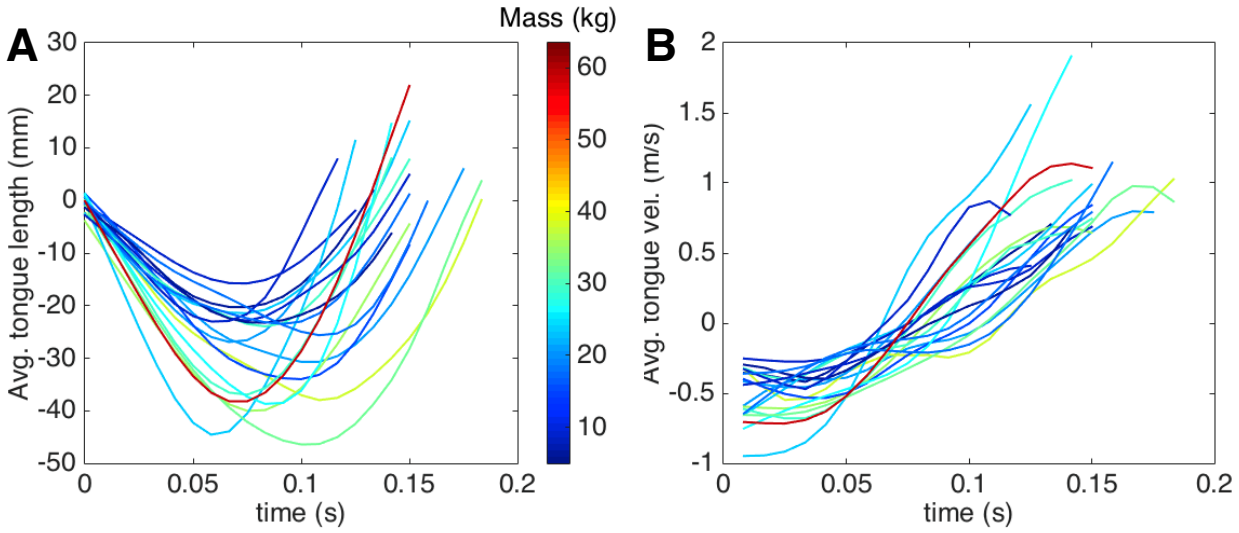

Figure 3.4: Tongue length (A) and velocity (B) versus time for all dogs. The color bar corresponds to each dogs weight in kilograms. The tongue enters the water bath at a relatively constant speed and is then accelerated out of the bath and into the mouth. Tongue extension is shown as a negative length so the velocity is positive when the tongue is entering the dogs mouth. Four laps are averaged for each dog (n=19x4) and the error bars are not shown to avoid clutter.

at a relatively low speed. However, when the tongue exits the water and returns to the mouth, high accelerations (1-4 g) and high speeds (0.7-1.8 m/s) were observed.

Such high accelerations contrast with those of domestic cats, which move their tongue upwards at approximately 1-2 g then decelerate the tongue as it enters the mouth [11]. To determine the significance of unsteady inertial effects, we modeled the fluid transport as an open fluid pump (Figure 3.12B), driven by a pressure difference between points A (on the tongue) and B (in the far field).

From our experiments, we found that the major mechanism of transport is inertia. Therefore, assuming high Reynolds number and neglecting surface tension, the flow can be considered as a potential flow, and can be written as:

$$p_A - p_B \sim \rho R_A \frac{\partial u}{\partial t} - \frac{1}{2}\rho u^2, \tag{3.1}$$

where p is pressure, ρ is fluid density, R_A is the tongue radius, and u is the fluid velocity. With the accelerating tongue, the unsteady inertia scales as

$$\rho R_A \frac{\partial u}{\partial t} \approx \rho \frac{R_A U_A}{T}, \tag{3.2}$$

where T is the time from the minimum tongue velocity to the end of the lap and U_A is the

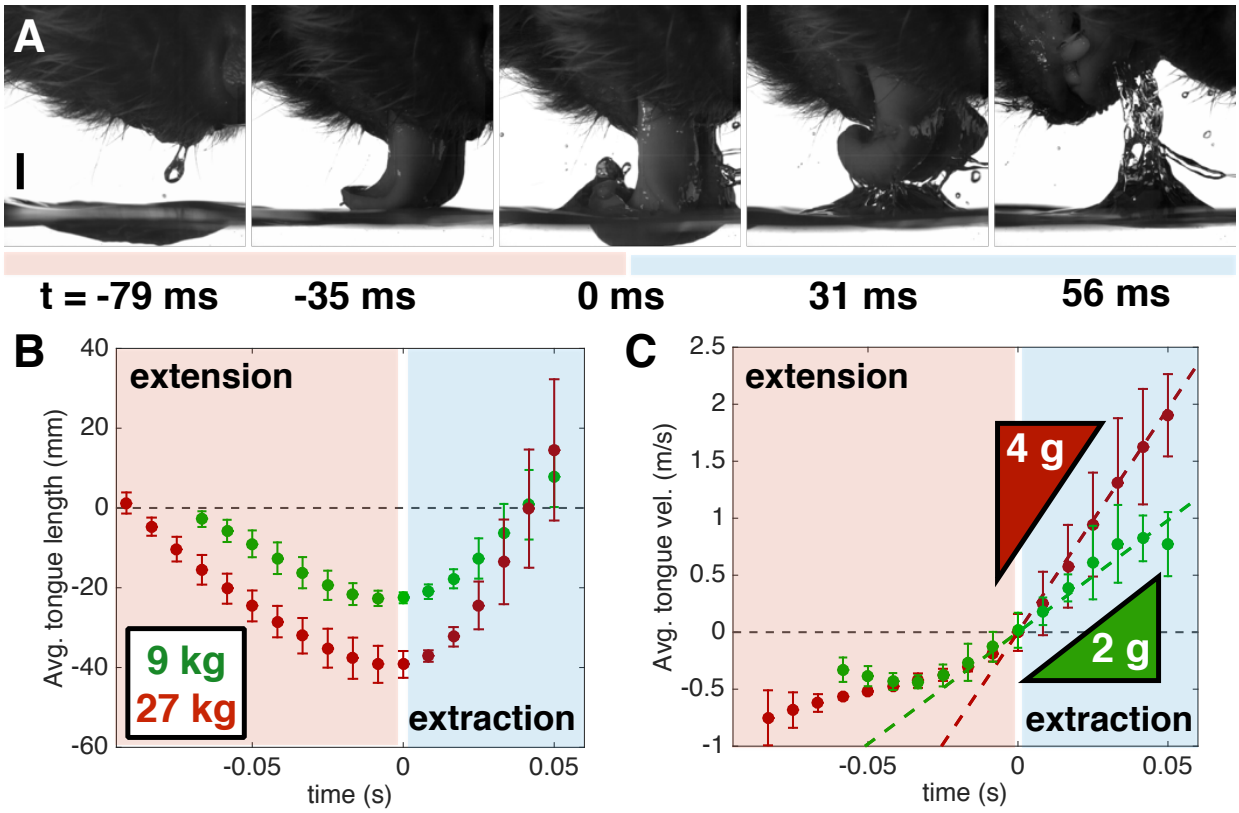

Figure 3.5: A) A dog (Labrador/poodle mix, 29.5 kg) extends and curls its tongue backwards, strikes the surface of the fluid (time zero is at maximum tongue length), and quickly withdraws its tongue to form a water column above the bath (recorded at 1500 fps). Scale bar is 10 mm. The color bar corresponds to extension and retraction as in (B) and (C). B) Length versus time of four laps for a Shiba Inu (9 kg) and a Labrador mix (27 kg). The error bars represent one standard deviation from four laps for each dog. Red shading denotes tongue extension and entry into the water, and blue shading denotes tongue exit and retraction back into the mouth. C) Velocity versus time for the two dogs. The small dog's tongue has an acceleration of $\sim$2 g, compared to the large dog's value of $\sim$4 g. Comparison to cats can be made by referring to [11].

maximum tongue velocity. Then, the effect of the steady inertia scales as

$$\frac{1}{2}\rho u^2 \approx \frac{1}{2}\rho\frac{U_A^2}{3}, \tag{3.3}$$

where the 1/3 factor is due to averaging of the velocity ($u = At$) over time. To pump, $p_A - p_B$ must be less than zero. A ratio of unsteady to steady effects scales as

$$St = \frac{6R_A}{U_A T}, \tag{3.4}$$

which is defined as the Strouhal number.

For dogs, $St = 3.7 \pm 1.4$ (mean±S.D.) and for cats [11], $St \sim 1.1$, indicating that unsteady effects drive the motion of the liquid column for dogs, but not for cats. Although both animals use their tongues to lap, dissimilar tongue kinematics result in a significantly different interplay of forces, suggesting that cats and dogs employ different physical mechanisms for drinking.

Two important questions remain to be answered. If dogs do not actually scoop water with the back of the tongue, why do they curl the tongue when they drink? And, what is the effect of high tongue acceleration on the water column formed by the tongue, relative to the timing of the lapping cycle?

3.4 Physical rod experiment

To address these questions and gather a deeper understanding of the hydrodynamics of lapping, we performed a physical experiment that simulates the hydrodynamics of liquid column formation using a rounded rod to simulate the tongue. The most crucial aspect of the lap appears to be the quick retraction of the tongue into the mouth, a motion that creates a water column that the dog drinks. In this experiment, we varied the upward acceleration and the size of the rod to capture the relevant physical regime used by drinking dogs. Dimensional analysis reveals high Reynolds $O(10^3 - 10^4)$, Froude $O(10^0 - 10^1)$, and Weber $O(10^1 - 10^3)$ numbers, suggesting that viscous and capillary forces should be negligible compared to inertia and gravity. To confirm the insignificance of surface tension effects, both water (σ = 72 mN/m) and ethanol (σ = 20 mN/m) were used as a liquid bath.

Rounded glass rods (R=8-20 mm) were positioned such that the tip was one radius below the surface of the bath, and then pulled out by stretched springs, giving the rod a near-constant upward acceleration with magnitudes (1-8.5 g) that encompass the measured values from dogs (1-4 g). To vary acceleration, springs of varying stiffness were used and stretching length was changed. A schematic of the experiment setup can be seen in Figure 3.6. To track the upward motion of the rods, a randomly generated dot pattern was placed inside the tube and the Matlab image processing toolbox was used to track the rod motion and the volume of fluid pulled from the bath. The motion of the rod and fluid was filmed using an Integrated Design Tools N3 camera at 1500 frames/s and a shutter speed of 100-200 μs.

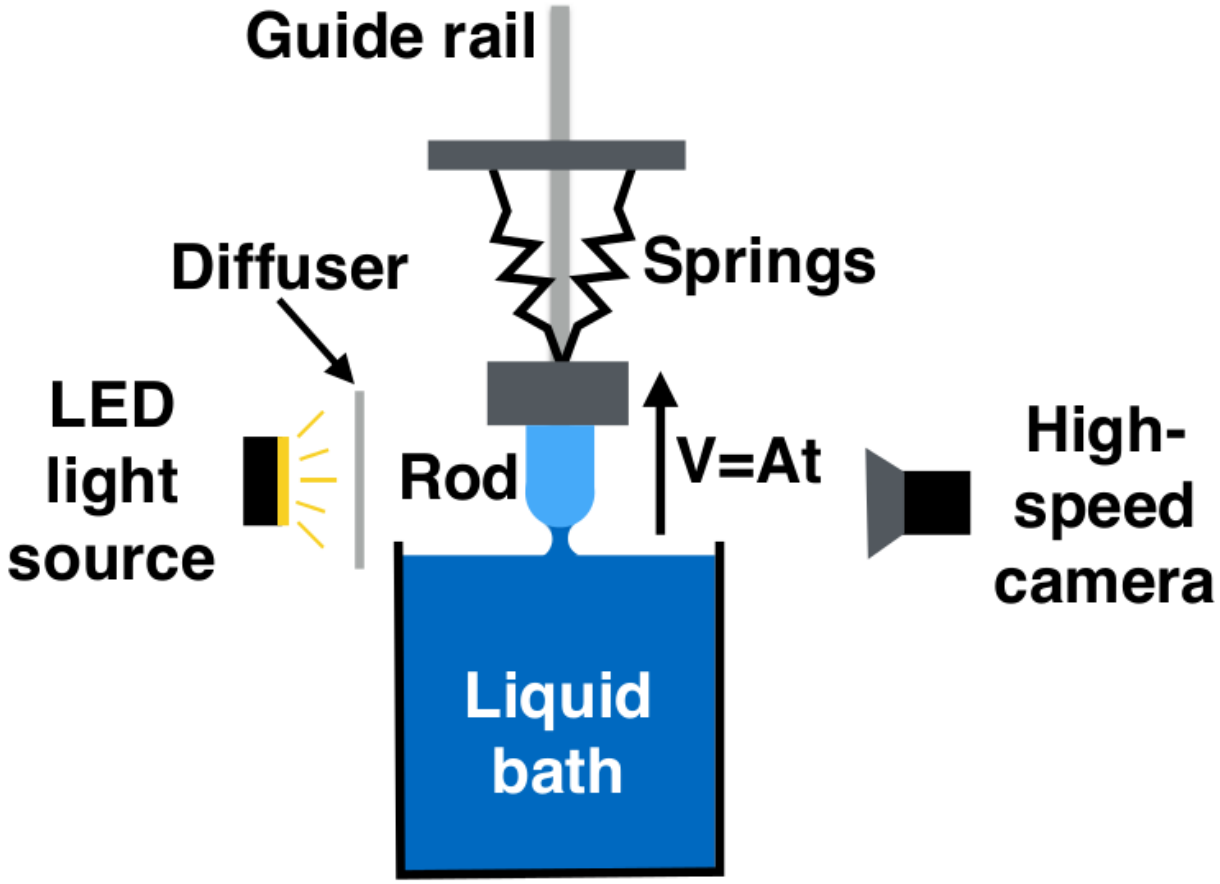

Figure 3.6: Glass rods were pulled up by two stretched springs. The strength of the springs as well as stretching length were varied to change acceleration. A pulley system was used to pull the rod down into the bath and stretch the springs. Lubricated steel guide rails prevented any lateral rod motion. In order to accurately track the rod motion a random dot pattern was placed inside the rod. An IDT N3 high-speed camera filmed the motion at 3000 fps with a shutter speed of 100-200 μs.

When the rod traveled up, a column of water was pulled out of the bath due to inertia, simulating the column formed by a dog's tongue (Figure 3.8A). The extracted volume was measured from a distance of above the bath to avoid the large bulk of liquid that quickly falls back down (seen in Figure 3.7). This is justified, as the dog is not able to drink this portion of the liquid as it falls back to the bath well before the dog bites down on the column to drink. In Figure 3.8A time zero is when the tip of the rod is just level with the surface of the liquid bath.

The measured volumes of liquid extracted from the bath were on the same order of magnitude as the volume that a dog drinks per lap ($\sim$2.5 ml) [37]. We found that the total volume of liquid extracted from the bath was positively correlated with rod size (Figure 3.9). This result suggests that a dog curls its tongue to increase the effective diameter in contact with fluid, extracting more fluid than if the tongue were withdrawn straight out of the bath.

From this physical experiment, we also see that the extracted volume is positively correlated with rod acceleration (Figure 3.9), indicating that the dog could modulate tongue acceleration to control the amount of fluid that is pulled out of the bath. However, the tongue's maximum acceleration, and hence the maximum extracted volume per lap, is limited by biomechanical constraints. Figure 3.8B shows that the pinch-off time of the fluid column largely depends on acceleration of the rod, with larger accelerations producing shorter pinch-off times. Thus to optimize the volume ingested per lap, the dog should accelerate its tongue as fast as possible, while also timing its bite so that its jaws are closing at the moment of pinch-off. These actions are bounded by the jaw muscles physiology and arrangement, and

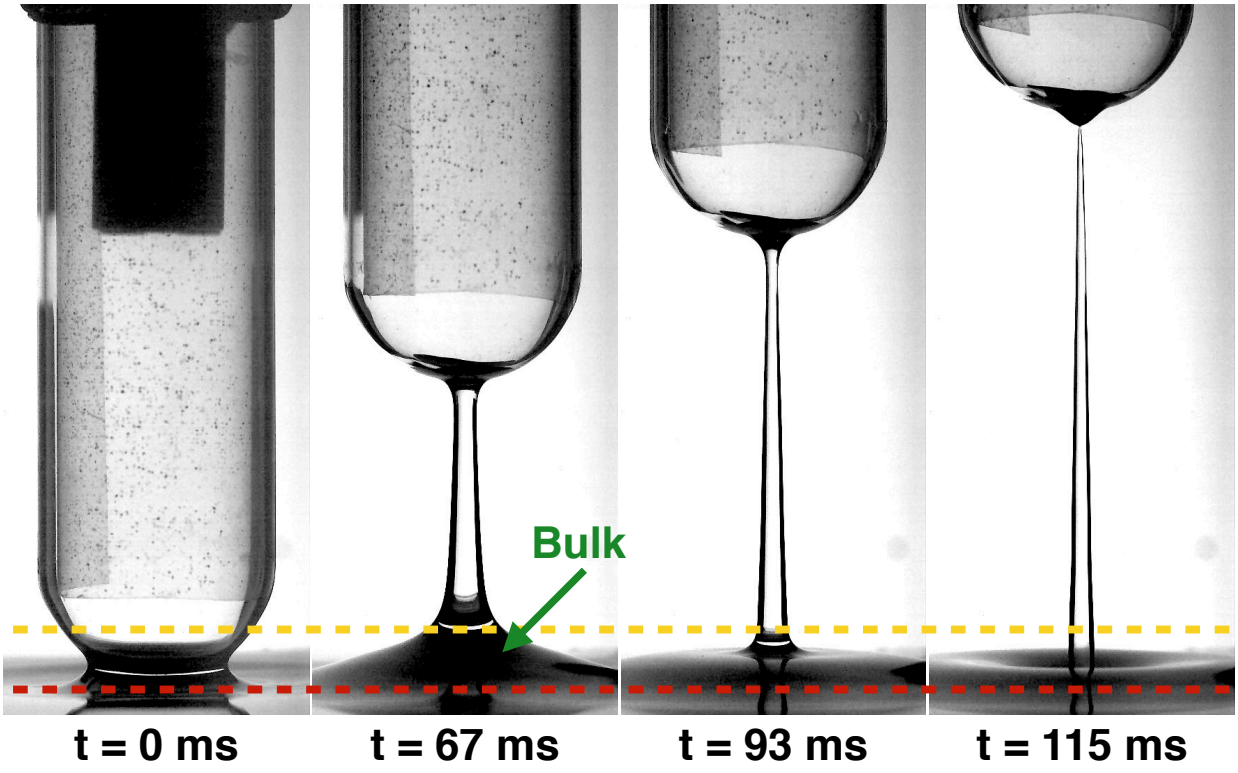

Figure 3.7: An image sequence showing the large bulk that rises and falls back to the bath. The red dashed line indicates the fluid surface and the yellow dashed is R/2 above the surface. Since the fluid quickly falls back into the bath it is unlikely a dog would be able to drink any of the volume below the yellow line.

the relative sizes of the tongue and jaws [38, 39].

We can also identify the time and volume scaling of the column volume. First, we consider the time scale of the maximum column volume. The column volume increases due to upward acceleration, and drains due to gravity. If a control volume is chosen for the liquid column, there are two pressures competing with one another: one is the pressure due to unsteady motion, $\rho\frac{\partial\phi}{\partial t} \sim \rho AR$, and the other is pressure to due gravity, $-\rho gH$, where H is the height of the column. The height of the column increases as $H \sim 1/2At^2$. These two forces are balanced at

$$t_{grav} \sim \sqrt{R/g}. \tag{3.5}$$

Rescaling time by t_{grav} gives the time of maximum volume at $t_{grav} = 1.6 \pm 0.2$ (mean±S.D.).

Next we consider the volume of the liquid column. The liquid column can be considered as a conical shape, as observed in our experiments. Also, when the liquid column reaches its maximum volume, the height of the conical shape is close to the height of the rod (as shown in Figure 3.9C. To start, we use two assumptions: that the liquid column has a conical shape with height H and that the bottom of the liquid column has radius R (the rod size). From our physical experiments, we observed that for high accelerations, the column has maximum volume at pinch-off, and for low accelerations, maximum volume occurs before pinch-off. Comparing t_{grav} with t_p^{theory} gives $\pi\sqrt{R/A} \sim 1.6\sqrt{R/g}$, and the transition from low to high acceleration is identified. When $A/g < \pi^2/1.6^2$, the column reaches maximum volume before

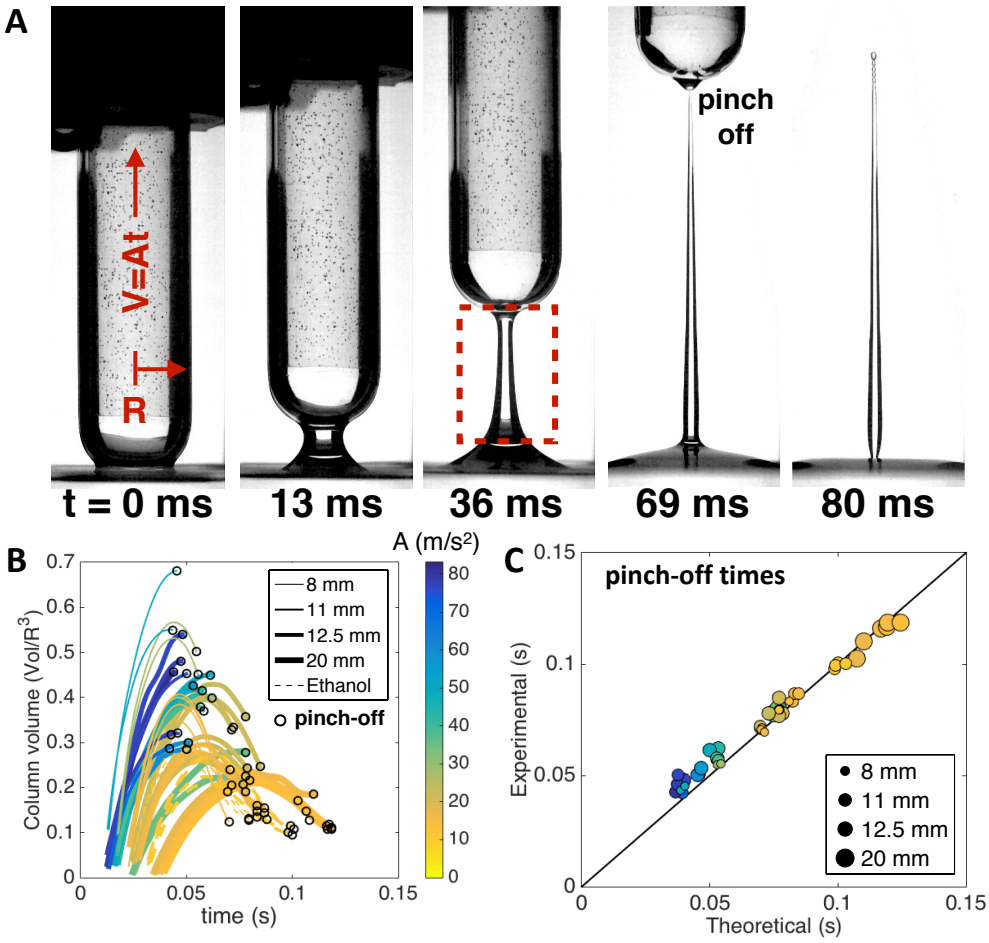

Figure 3.8: A) A rod (R = 11 mm) pulls liquid out of a bath with an acceleration of 1.6 g, the liquid then pinches off from the rod and falls back toward the bath. The red box shows where volume was measured R/2 above the surface for that frame. Pinch-off occurs at t=69 ms. B) Liquid volume in the column versus time as a rod was pulled out of the water (n=50). Liquid volume was normalized by the radius of the rod cubed (Vol/R^3) to compare across rod sizes. Line width corresponds to rod radius, color to acceleration, and dashed lines represent ethanol cases. The open circles represent the time of pinch-off. The curves are time-shifted so that t = 0 is the moment that the bottom of the rod was level with the fluid surface. C) Experimental pinch-off time versus theoretical pinch-off time (n=50). The black line has a slope of 1. Only rods with acceleration greater than 1 g are shown.

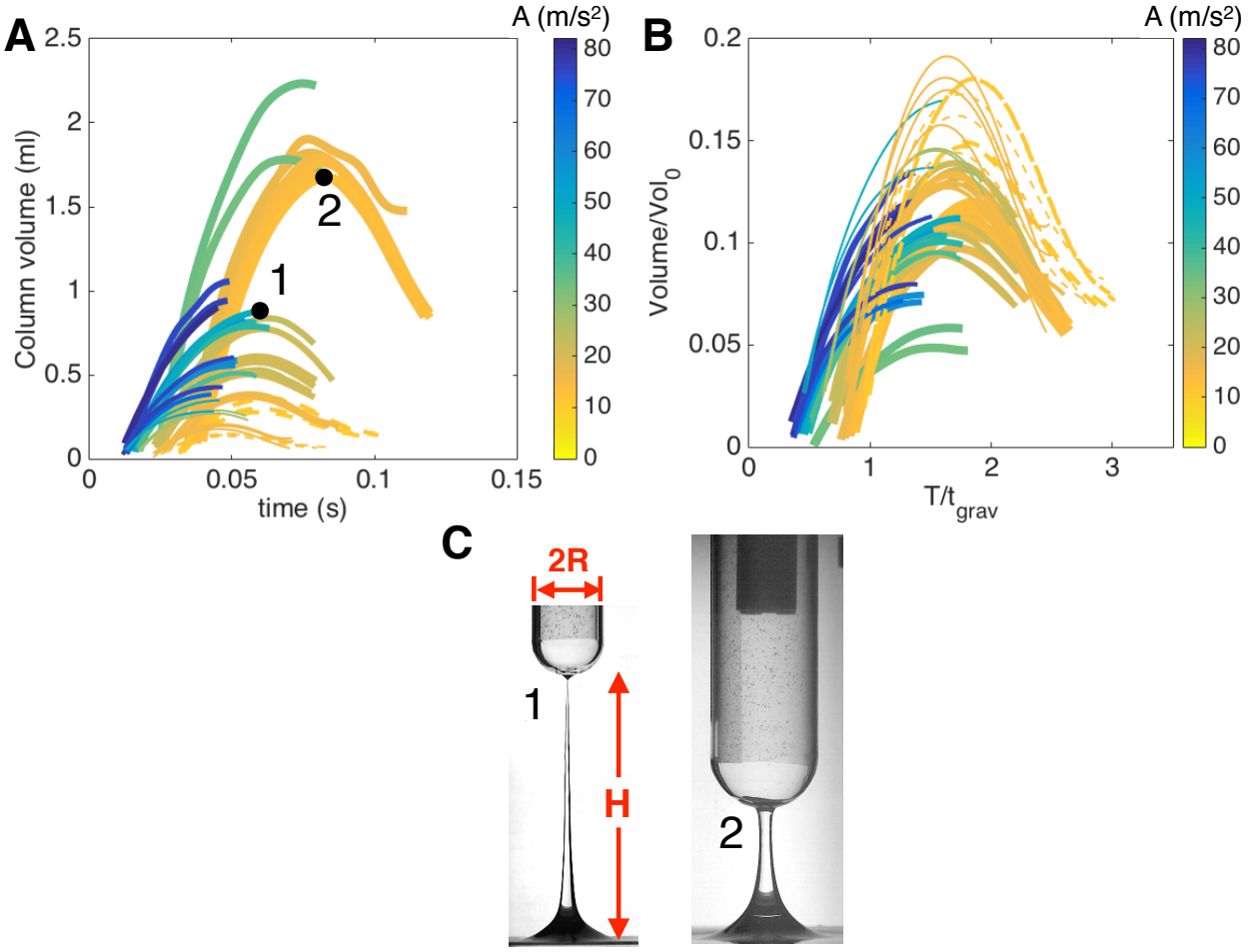

Figure 3.9: (A) Absolute volume of water in the developing column through time from the physical experiment. (B) Comparison of water column development using rescaled values. Column volume is normalized by the maximum theoretical volume, Vol_0, and time is normalized by $t_{grav} = \sqrt{R/g}$. The maximum volume occurs at 1.6±0.2 of the rescaled time. (C) Examples of how the water column was approximated as a cone with height H and bottom radius R (same as the rod radius) for (1) a high-acceleration case (A=44 m/s^2, R=12.5 mm) where maximum volume occurs at pinch-off and (2) a low acceleration (A=11 m/s^2, R=20 mm) case where maximum volume occurs before pinch-off.

pinch-off, and the maximum volume is $V_0 = \pi/3R^2H$, where $H = 1/2At^2$. Then,

$$V_0 = (\pi/6)R^3(A/g)(1.6)^2 \; at \; t = t_{grav}. \tag{3.6}$$

When $A/g > \pi^2/1.6^2$, column volume is maximum at pinch-off and

$$V_0 = (1/6)R^3\pi^2 at \; t = t_p^{theory}. \tag{3.7}$$

This scaling is shown in Figure 3.9A-B. Though the scaling works fairly well, there are some sources of error that cause inconsistencies. The bottom radius of the column is not always close to the rod radius at time of maximum volume or pinch-off. There could also be some surface tension effects that influence column volume that we do not take into account.

3.5 Comparing physical experiment to lapping kinematics

For all trials, we observed that pinch-off occurred very close to the tip of the rod. The velocity potential in fluid column due to the acceleration rod can be estimated as

$$\phi \sim \frac{1}{4}RAt \tag{3.8}$$

Using the unsteady Bernoulli relation, the radial velocity is $v_R \sim \frac{\sqrt{AR}}{2}$. To start, the equation

for the wetted length on the rounded end of the cylinder is

$$s(t) = \frac{\pi}{2}R - \int_0^{t_p} v_R dt, \tag{3.9}$$

where R is the radius of the rod, is the radial velocity of the water column, and t is the time since the rod tip exited the fluid bath. πR is used as the initial distance because the contact line of the fluid with the rod must travel along the curved portion of the rod before pinch-off. The pinch-off time was determined when $s(t_p^{theory}) = 0$. The radial velocity is then inserted into the expression for $s(t)$ to get

$$t_p^{theory} \sim \pi\sqrt{R/A}. \tag{3.10}$$

This pinch-off scaling has also been confirmed previously [40]; however, their experiments were in the stretching regime where surface tension dominates. From Figure 8C, it can be seen that our theoretical equation for pinch-off time, $t_p^{theory} \sim \pi\sqrt{R/A}$, matches well with experimental data in which there is high acceleration of the rod (above approximately 1 g).

From Figure 3.11C, it can be seen that our theoretical equation for pinch-off time, $t_p^{theory} \sim \pi\sqrt{R/A}$, matches well with experimental data except for low acceleration cases. We have also developed another theoretical relationship for low accelerations based on the pressure difference in the column pulled from a bath [11]. Similarly, the liquid column on the cylinder follows Equation (3.9). If we assume that hydrostatic pressure drives the motion of the column interface, radial velocity can be written as $v_R \sim \sqrt{gH}$, where H is the height of the

tip of the rod above the free surface and g is acceleration due to gravity [11]. The rod moves with a constant acceleration, so $H = 1/2At^2$, where is acceleration of the rod. Pinch-off occurs when s(t)=0, so the equation becomes $0 = \pi R - \int_0^{t_p} \sqrt{1/2gAt^2}dt$. Solving for t_p gives

$$t_p^{theory,2} \sim \frac{(2\sqrt{2}\pi R)^{1/2}}{(Ag)^{1/4}}. \tag{3.11}$$

$t_p^{theory,2}$ over-predicts the pinch-off time for a dogs lap at high accelerations, but it matches experimental data well for rods with small accelerations. We believe that t_p^{theory} is valid for the dogs, as most dogs lap with large tongue acceleration (1-4 g). Figure 3.10 shows a comparison between the two theoretical equations for pinch off. In this figure, both t_p^{theory} (blue line) and $t_p^{theory,2}$ (black line) have no fitting parameters.

Figure 3.8C shows that there is good agreement between experimental and theoretical pinch-off times, indicating that the theoretical model captures the physics of the physical model.

When does the pinch-off time occur relative to the dogs bite time? We defined the bite time, t_{close} , as the time between the tongues exit from the water bath to when the jaw closes, measured from the lapping videos. From four laps per dog (n=4x19), we found that the ratio t_{close}/t_p^{theory} for all dogs is 0.92±0.23 (mean±S.D. Figure 3.11A), indicating that the dogs bit down on the water column approximately at pinch-off, which should maximize the intake of water per lap. This result provides the connection between the dogs drinking behavior and our physical model, and also leads us to predict the optimum frequency for lapping.

From Figure 3.11A, the dog's jaw closing time, t_{close} , is proportional to the rod pinch-off

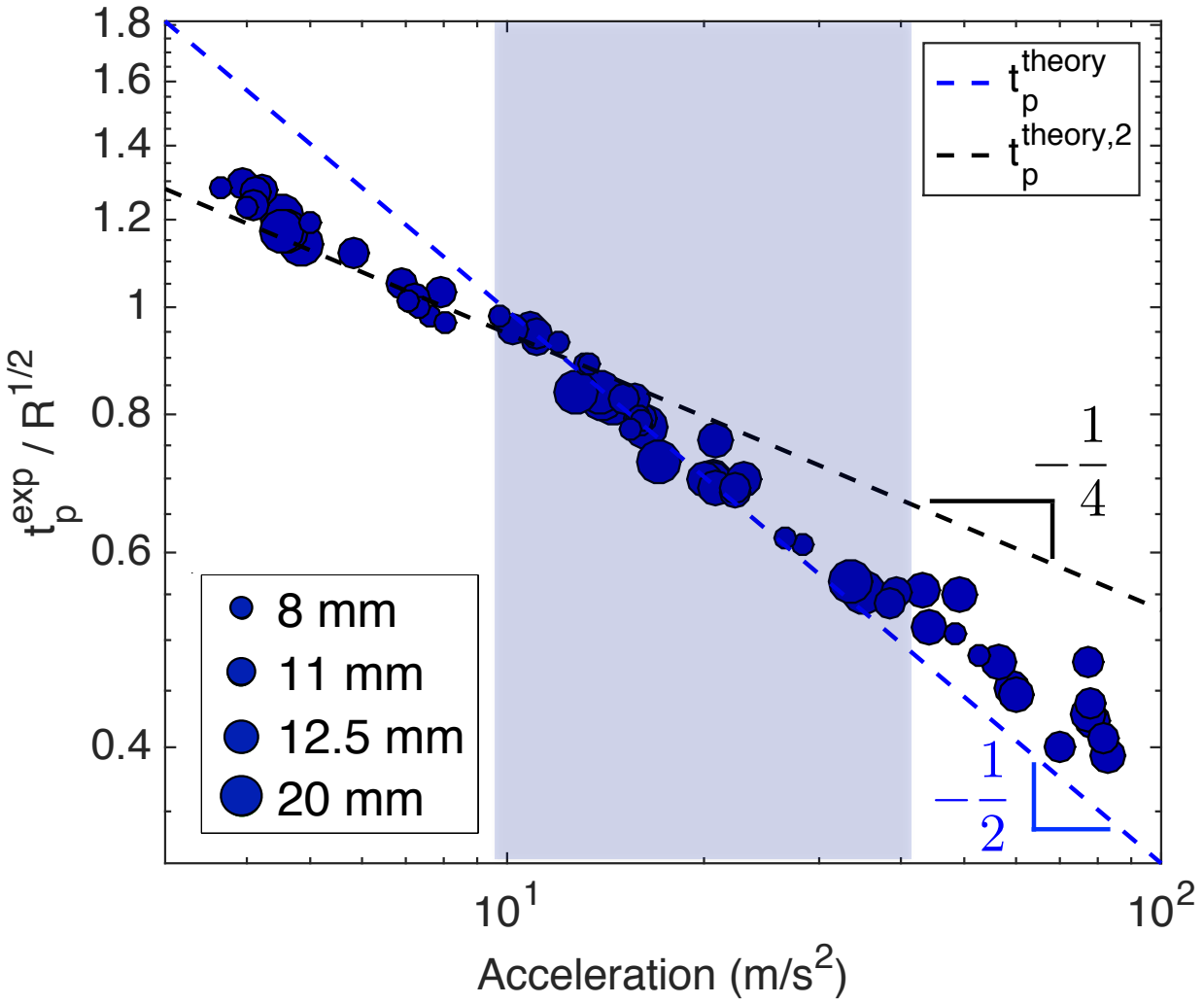

Figure 3.10: Physical experiment pinch-off time, t_p^{exp}, over $R^{1/2}$ as a function of acceleration (n=70). The blue dotted line shows t_p^{theory} and the black dotted line shows $t_p^{theory,2}$. At high accelerations, t_p^{theory} slightly under-predicts the pinch-off time, whereas $t_p^{theory,2}$ over-predicts pinch off time at high accelerations. t_p^{theory} is more valid for regime used by the dogs (blue color band).

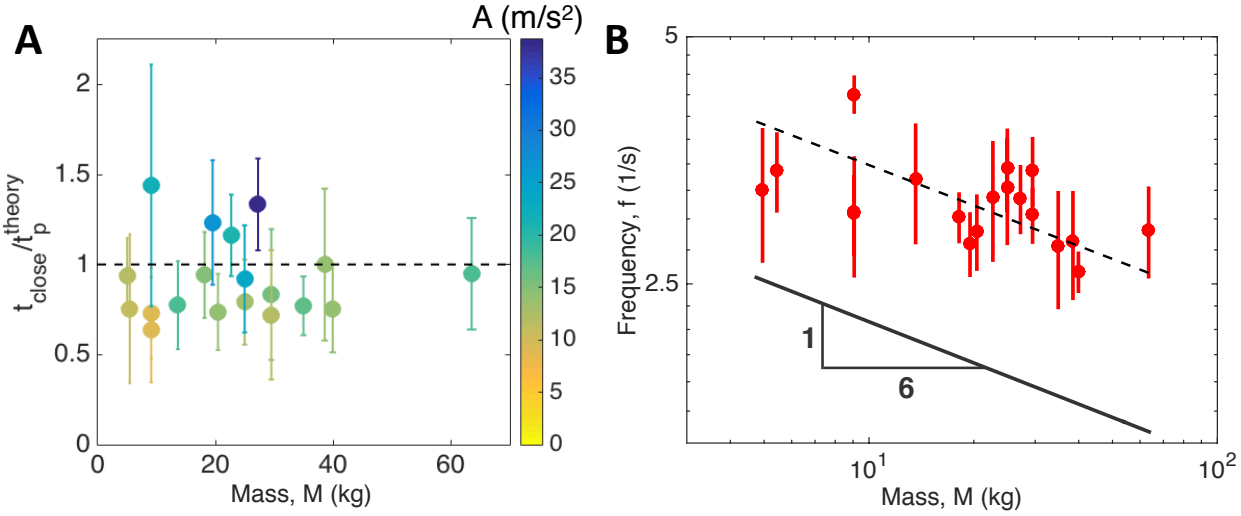

Figure 3.11: A) Jaw closing time over theoretical pinch-off time for all dogs (n=4x19). B) Frequency of lapping versus weight for dogs. $f_{lap} \sim M^{-1/6}$ is shown with the gray solid line. The line of best fit (dashed black) has slope -0.16±0.09 (95% CI). For both A) and B), error bars indicate the standard deviation for each dog (4 laps x 19 dogs).

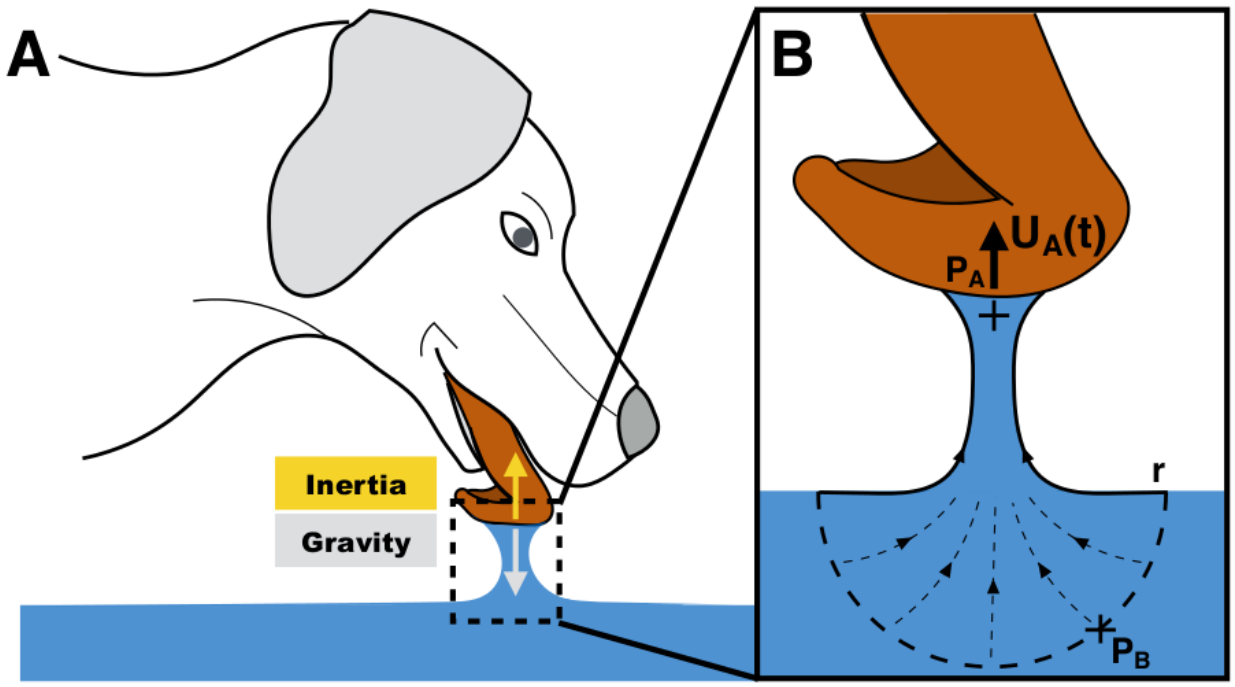

Figure 3.12: A) Schematic depicting the opposition of inertia and gravity during lapping. B) A model of open pumping, developed to understand how the dog creates a water column. In this model, the pressure difference between points A and B drives the extraction of fluid from the bath. Point A is beneath the tongue (indicated with a plus sign), point B is considered at a far field $r \to \infty$, and $U_A(t)$ is the tongue velocity.

time, t_{pinch} . Jaw closing time, t_{close}, is also proportional to $1/f_{lap}$, where f_{lap} is lapping frequency: $1/f_{lap} \propto \sqrt{R/A}$. From Figure 3.2, tongue radius scales as $R \sim M^{1/3}$ to give $f_{lap} \sim A^{1/2}M^{-1/6}$. There is also no significant relationship between A and any other parameter, so we assume that A is insignificant with respect to dog mass, tongue radius, and lapping frequency (R^2 of 0.058, 0.19, and 0.000040 respectively) which gives

$$f_{lap} \sim M^{-1/6}. \tag{3.12}$$

3.6 Conclusion

The results of this study help to explain the qualitative observations of many dog owners: dogs tend to be messy drinkers and splash water on themselves and the floor. This phenomenon may be a by-product of their lapping mechanism. The large effective area of a dog's tongue that impacts the liquid surface, the penetration of the tongue below the liquid surface, and the high acceleration of the tongue as it is raised out of the liquid bath all contribute to increasing the volume of fluid extracted per lap. However, not all of the fluid displaced by the curled tongue enters the vertical column, and some is splashed laterally. In addition, when the tongue is accelerated upward, the water in the ladle is generally tossed to either side of the dogs mouth. Though dogs do not use their tongue to actively scoop water into their mouth, it is possible that the scooped liquid has some positive effect on the water column dynamics below the tongue. In particular, the scooped liquid could spill around the

tongue and feed into the water column below, extending the formation time and increasing the volume of the column. This hypothesized role of scooping in the fluid column dynamics should be investigated further. This work was published the Proceedings of the National Academy of Sciences and is titled "Dogs lap using acceleration-driven open pumping" [146].

Chapter 4

How bats drink on the wing

4.1 Introduction

Bodies of water like lakes, ponds, and rivers provide many benefits for bats. They are a source of abundant prey, provide shelter from predators, and provide a source of hydration [41]. Bats are known to show preference towards bodies of water with high numbers of insects [41]. As explained in the previous chapter, dogs, use lapping with the tongue to transport fluid against gravity and into the body. Bats on the other hand, use a different method of drinking in that they swoop down and drag their tongue laterally across the water surface causing water to splash into the mouth. This swooping behavior has been observed in at least 15 bat species from seven genera in three phylogenetically distinct bat families [25].

Instead of standing or sitting while drinking, like most animals, bats fly through the air while

they drink. They must drink with great precision, as an error could prove fatal if they were to tumble into the water. A previous study shows how bats use echolocation to find a water source [25], but how bats transport water from a water source to the mouth is still unknown. This is a unique dynamic drinking behavior that could give insights into the development of novel engineering systems like an air vehicle capable of drawing samples from a large body of water very quickly.

In this study, multiple cameras were used to capture the kinematics and fluid mechanics of bats drinking water on the wing in a laboratory. Using Matlab image processing and computer vision techniques, a three-dimensional view of the bats drinking kinematics is reconstructed. With these imaging techniques, the velocity and water penetration depth of the tongue along with the head and wing position as the bat drinks were found. The methods bats use to transport water to the mouth were also identified. From these measurements, the forces experienced by the bat as it drag its tongue through the water were estimated. Additionally, the wing kinematics of a bat during drinking and rising flight were compared to show that drinking flight is less efficient than straight forward flight and comparable to rising flight. Finally, this is a preliminary study that is not yet finished and will be continued in the future.

Figure 4.1: A horseshoe bat (*Rhinolophus ferrumequinum*) drags its tongue through water to drink on the wing. This image was extracted from high-speed video taken in a bat aviary on the campus of Shandong University.

4.2 Experimental methods

Drinking experiments were conducted at the Virginia Tech Shandong University International Laboratory in Jinan, China. Two horseshoe bats (*Rhinolophus ferrumequinum*) were housed in a 4×3×1.25 m aviary and a 1×0.8×0.1 m water basin was placed in the middle of the cage, 1 m above the floor. Six GoPro Hero 4 cameras (GoPro, San Mateo, California, USA) filming at 240 frames/s with an image size of 840×480 px, a Southern Vision Systems (SVSi, Huntsville, Alabama, USA) high-speed camera at 500 frames/s with an image size of 1280×512 px , and two LED light panels were used to film drinking (see Figure 4.2). Three GoPro cameras were placed to the side of the tank, one was placed looking down the length of the tank, and the last two cameras were placed underneath the tank facing upwards. The high-speed camera was placed either to the side or looking down the length of the tank. GoPro cameras were not used when the high-speed camera was placed to the side of the tank.

To simulate the natural conditions of a bat emerging from a cave to drink water, the tank was drained 4 to 5 hours before filming and refilled just prior to turning the cameras on so that the bat would drink while the cameras were rolling. The bats were thirsty, however, only one of the two bats drank regularly during the time immediately following the water tank refill making approximately 10 to 20 drinking attempts in an hour. As a result, the data presented is from just one of the bats housed in the aviary. Filming took place for one to two hours to avoid exposing the bats to the bright LED lights for an extended period

of time. GoPro cameras filmed at 240 frames/s while the high-speed camera filmed at 500 frames/s. Bats were also monitored overnight with an infrared CCD camera to ensure they were able to drink and get adequate hydration from the water tank in the aviary even if they did not drink while the cameras were recording.

Multiple GoPro cameras were used to obtain a three-dimensional reconstruction of the bat, mouth, shoulder, and wing tip as it drinks water in the lab. The cameras were time synchronized by clapping hands together in view of each camera and identifying the moment two hands touched. The moment two hands touched could be identified in each camera. A calibration method [43] was used to determine each camera's relative translational and rotational positioning. To calibrate, a randomly generated pattern is waved in front of and between each camera. The calibration toolbox is able to identify features of the pattern. If the pattern was seen by more than one camera the position and rotation of one camera relative to the other was found.

Once the intrinsic and extrinsic parameters of the cameras were found, points of interested on the bat (mouth, shoulder, and wing tip) were digitized using the Matlab image processing toolbox. The position of the shoulder is frequently obscured by the wing. In order to get the shoulder position, the distance between the mouth and shoulder were measured for several frames in which both the points were visible, and an average spatial orientation was obtained. The spatial orientation between the mouth and shoulder remains relatively constant, so the shoulder location could be identified as long as the mouth was visible. Finally, the digitized points were imported into a stereo triangulation program [44], that outputs the 3D world

coordinates of the selected points. If any points are occluded in a camera view the program will skip that camera during the stereo triangulation. The program computes a triangulation if a point is seen by two different cameras and computes three triangulations if a point is seen by all three cameras. Each triangulation for a particular point does not always give the same location, so once the 3D coordinates were obtained, the program runs a trajectory estimation algorithm that smooths the output of the triangulations.

4.3 Drinking kinematics

Qualitative observations from our video show that the bats flew from their perching position down towards the water tank. As the bat approaches the water surface it extends its tongue and drags it across the water surface. The bat then flew up and away from the water basin while withdrawing the tongue into and closing the mouth. During drinking, the bat continuously flaps its wings to maintain lift, in contrast to the trawling behaviors observed in some bat species in which the bat will glide down and across the water surface [42]. This is because the bat cannot touch the mouth to the water surface while gliding as it needs a fairly high angle of attack of the wing and must position its body such that the feet are close to the water. Bats can also be seen bobbing their head up and down slightly out of phase with the beating of its wings. More observations are described in quantitative detail in the following paragraphs.

The cameras underneath the tank facing upwards were used to measure the velocity of the

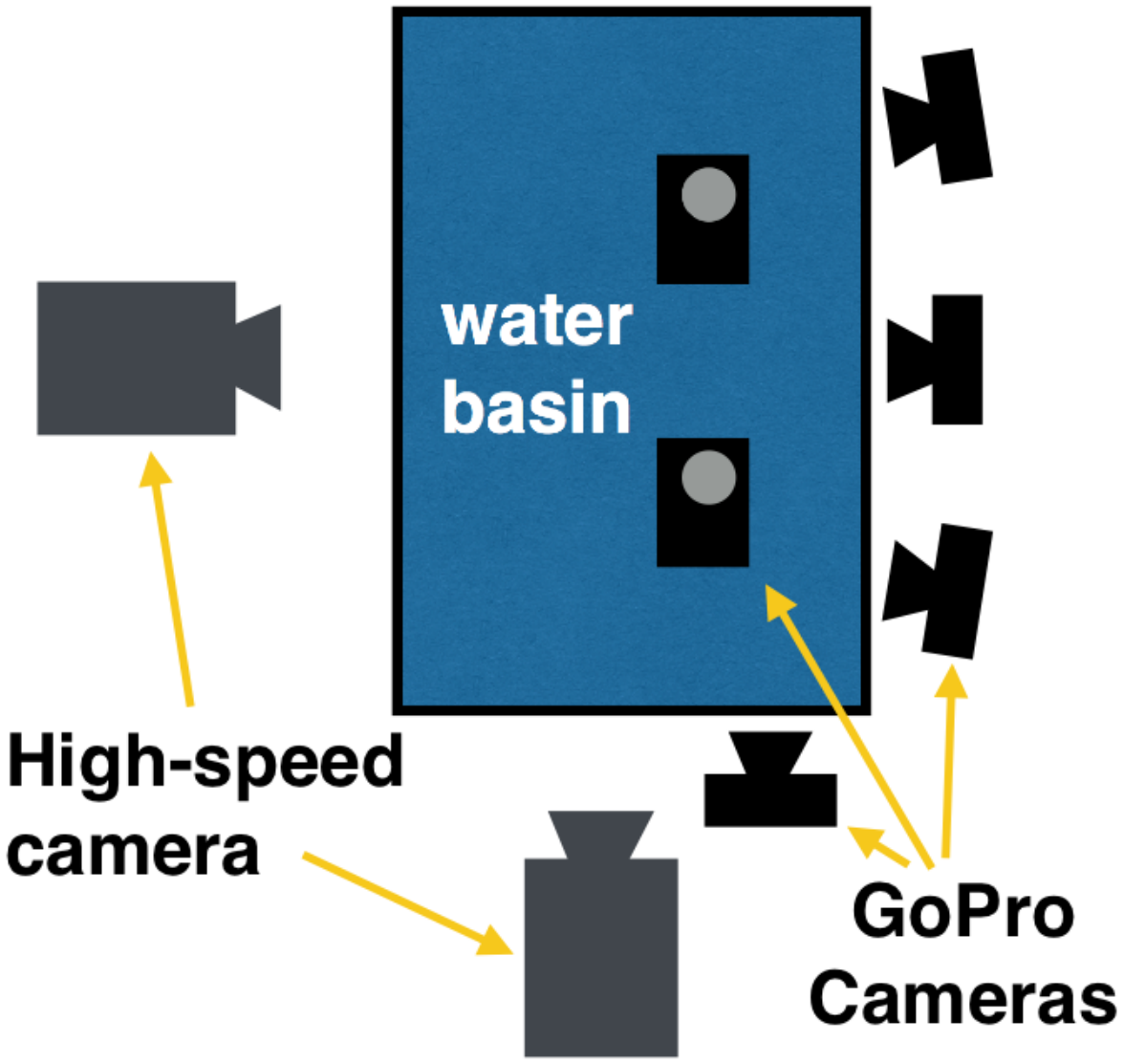

Figure 4.2: Top view of the setup of the camera and water tank in the bat aviary. Cameras were arranged to the side and underneath the water basin. Six GoPro cameras were used along with one high-speed camera in either of the positions shown. The tank was elevated on a table approximately 1 m off of the floor to make it easier than drinking from the floor.

Figure 4.3: Side view of drinking from the high-speed camera in the aviary. The bat is dragging is mouth across the water surface. In this image it is just about to pull the tongue out of the water and fly away from the surface.

bats tongue as it was dragged through the water. Velocity was measured from when the tongue touched the water until it was removed from the water. The mean and standard deviation of the velocity of 13 drinking attempts during one experiment session was 1.1±0.1 m/s. Footage from the high-speed camera front and side views were used to obtain the tongue size of the bat to calculate the approximate drag on the bat when it drinks. The tongue can be approximated as a sphere with a radius of curvature of 6 mm (show in Figure 4.9A, which gives a drinking Reynolds number of approximately 6500.

4.4 3D reconstruction of drinking kinematics

A three-dimensional reconstruction of the bats tongue and wing tip path was created using footage from three GoPro cameras. The cameras' intrinsic and extrinsic parameters were determined using a feature-detection based calibration program [43]. The calibration method was described in detail in the experimental methods section. Figure 4.4 shows the output of the calibration toolbox with the bat's flight path included for reference. The red objects show the camera positions and orientation in pixel coordinates. To convert from pixel to real-world coordinates, a grid of known size and viewable by all three cameras is placed over the water basin. Several points on the grid were triangulated to obtain a calibration value to scale pixel coordinates obtained after 3D reconstruction [44].

Figure 4.5 shows a side and top view of the tongue, shoulder, and wing tip position of a bat as it drinks (A,B) and flies away (C,D) from the water. There are several apparent

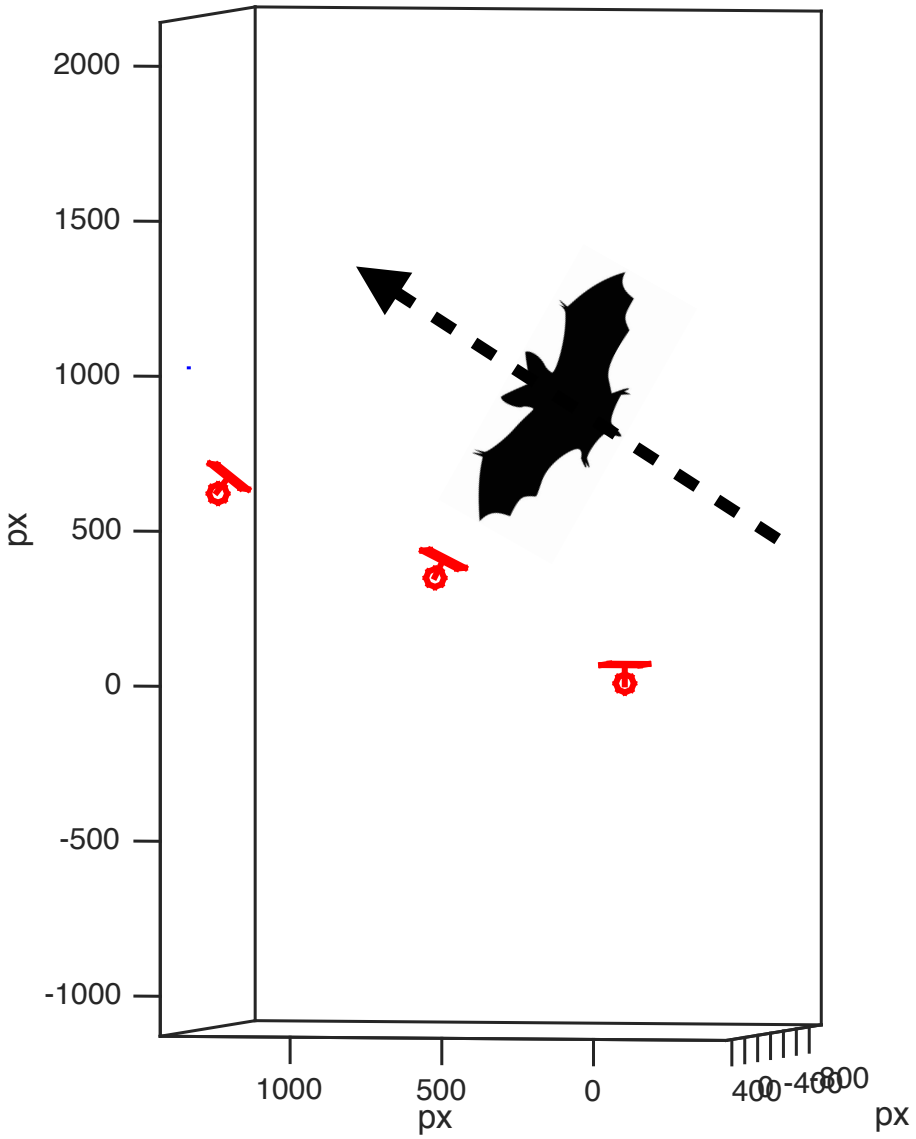

Figure 4.4: Diagram of the calibration output showing the camera orientation relative to how the bat flew across. The relative orientation and position of each camera is shown in red. Coordinates are in pixels. Scaling to real world coordinates is done by placing a grid of known size in view of all of the cameras.

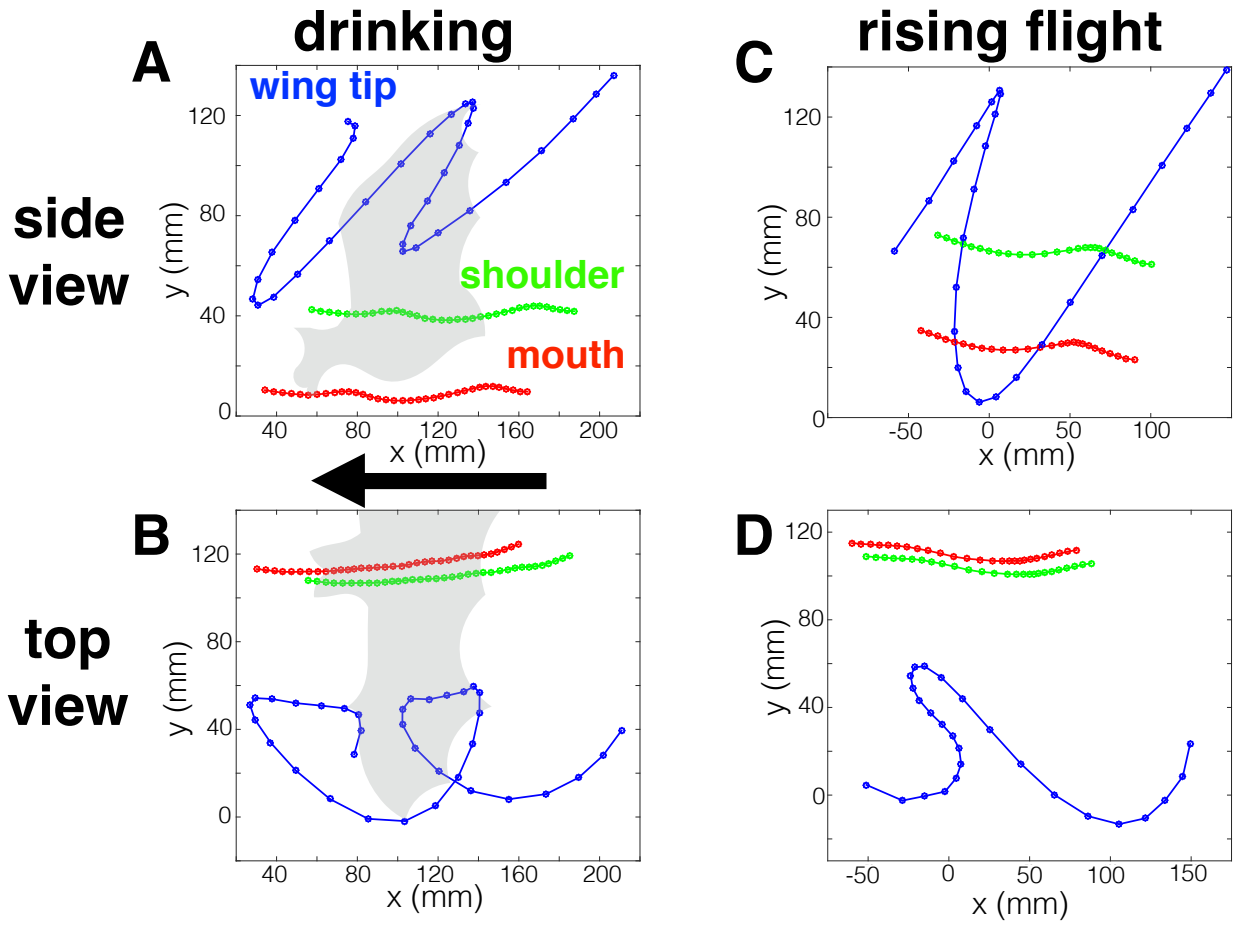

Figure 4.5: A) Side view 3D reconstruction of the mouth (red), shoulder (green), and wing position (blue) of a drinking bat in the lab frame of reference. B) Top down view of a drinking bat. C) Side of of a bat as it flies away from the water surface. D) Top down view of the bat flying away from the water. In each frame the bat is flying from right to left. The flight speed for drinking is 0.9 m/s and the flight speed for rising flight is 1.3 m/s.

differences in wing tip position from Figure 4.5. First, while drinking, the bat's wing tips remain high above the water surface and do not come down below the shoulder so that the wings do not impact the water surface. Also, the bat reverses the direction of the wing tip motion in the lab frame during the up and down stroke. This is a commonly observed behavior when bats fly close to a surface as it allows the bat to generate minimal negative lift during the upstroke [45]. During rising flight the bat's wing tips descend well below the body as it flies at a slightly faster speed of 1.3 m/s compared to 0.9 m/s during drinking. There is also much less wing tip reversal. Figure 4.6 shows the wing wing motion in the shoulder frame of reference for the same wing beats shown in Figure 4.5. Again the elevated compact motion of the wing can be seen during drinking. Relative to the shoulder, the wing stroke angle θ_w changes slightly between drinking and rising flight ($\approx 45^o$ for drinking and $\approx 56^o$ for rising). To find a measure of flying efficiency during drinking, rising, and regular flight we calculate the advance ratio, $J = V/(fA)$, where f is wing beat frequency, A is wing beat amplitude, and V is flying velocity. For drinking flight the advance ratio is 0.9±0.05 (n = 7 wing beats), for rising flight $J = 0.7 \pm 0.2$ (n = 8 wing beats), and for regular flight $J = 1.8 \pm 0.5$ showing the drinking is slightly more efficient than rising flight but much less efficient than level flight. The optimal range of advance ratio for cruising level flight has been found to be $2.5 < J < 5$ [46].

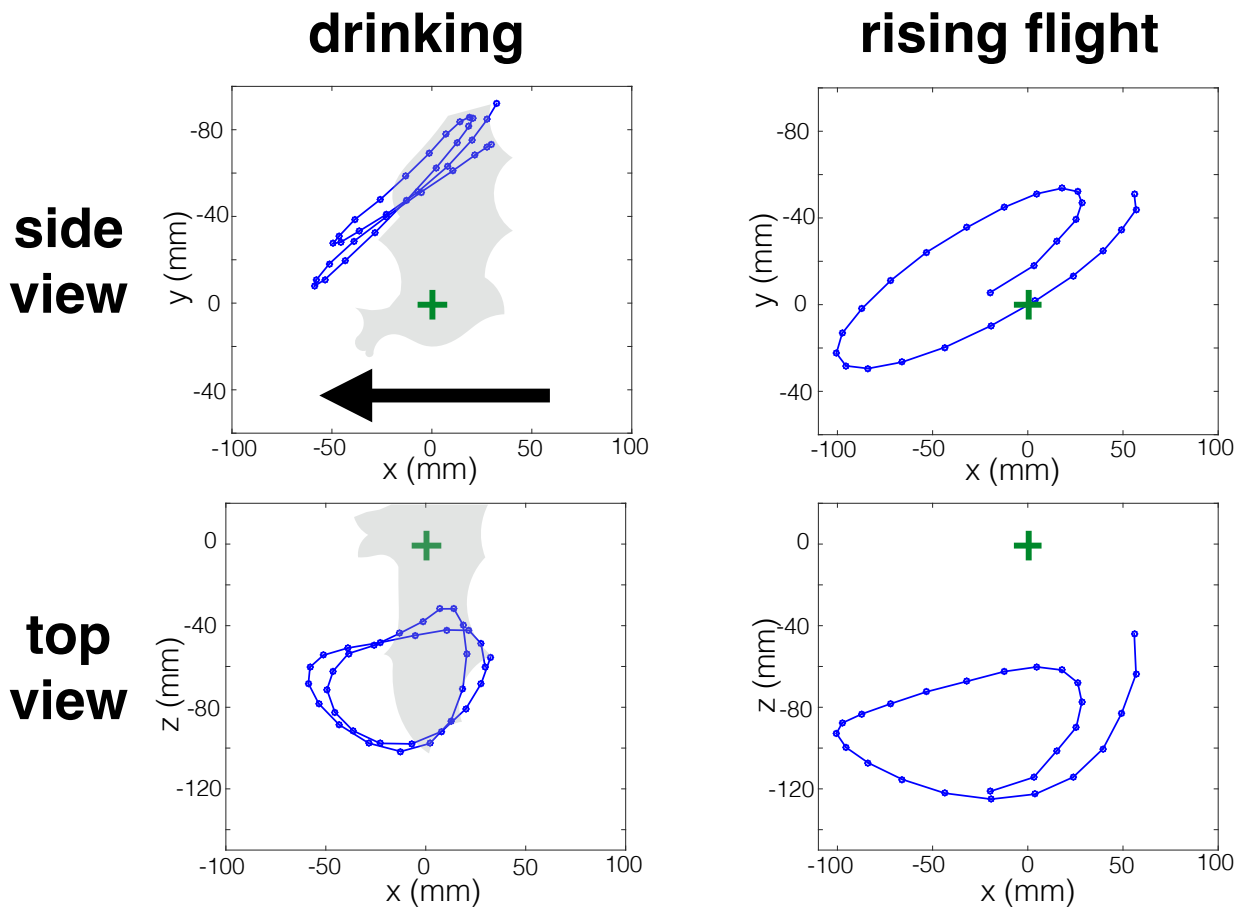

Figure 4.6: 3D reconstruction of the wing tip motion relative to the shoulder (greed cross) of the same wing beats shown in Figure 4.5.

4.5 Mouth-water interaction during drinking

It was previously mentioned that bats drink by flying down to a water surface while extending the tongue and then drag the tongue or tongue and bottom jaw through the water. When they drag the mouth along the water surface, water sticks to the tongue and inside of the mouth. The bat then shuts the mouth and swallows the liquid that sticks to the tongue and inside of the mouth. Two different methods of the drinking behavior have been observed: one where the bat only dips its tongue into the water and the other when the bat submerges most of its lower jaw while drinking. These two behaviors are called dipping and scooping respectively.

From casual observation of dipping versus scooping, it would appear that bats would prefer to the scoop water as it would transport more fluid from the bath to the mouth during a drinking attempt. However, selection of either dipping or scooping seems quite random as the bat was observed dipping its tongue on 57% of 44 drinking attempts. Therefore, it is possible that the bat is considering other factors besides how much water it can splash into its mouth when deciding what method to use. One consideration is the drag force on the bat when the tongue or mouth impacts the water bath. The tongue tip position was tracked as the bat drank (Figure 4.7). Penetration depth of the tongue was 4.1±1.8 mm (mean±S.D.).

The drag force on the bat due to the tongue and mouth can be calculated by approximating the system as a spherical skipping stone with radius R (seen in Figure 4.9). According to

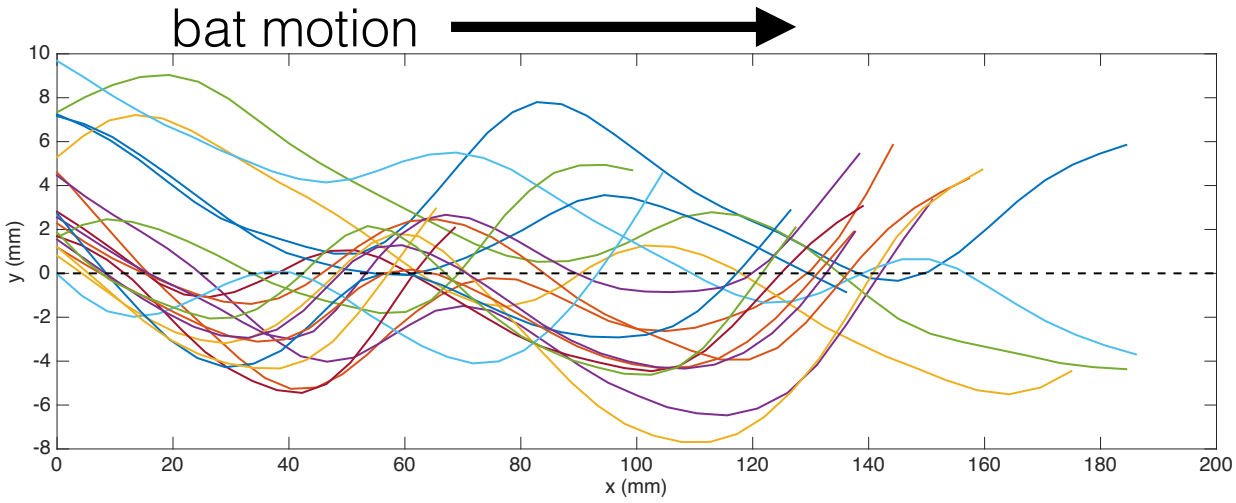

Figure 4.7: Tongue tip position for 19 bat drinking attempts. The depth average maximum penetration depth for each drinking attempt is 4.1±1.8 mm (mean±S.D.). Bats are flying from left to right and the dashed line represents the water surface.

Johnson and Reid [47], the horizontal drag force acting on a skipping sphere goes like,

$$F_D = -\pi\rho V^2 R^2 \left[\frac{\cos^2\lambda}{128}\left(12\phi_0 + \sin 4\phi_0 - 8\sin 2\phi_0\right)\right], \tag{4.1}$$

where ρ is fluid density, V is the bat velocity, λ the angle of impact, and ϕ_0 the angle of the sphere in contact with the water. First, the drag can be calculated assuming only the tongue makes contact with the water bath. From the high speed footage, if the tongue is assumed to be a sphere with diameter, R, of 6 mm, the tongue velocity, V, is 1.2 m/s, angle of impact λ is 0 degrees, and the contact angle ϕ_0 is $\pi/4$, the drag on the tongue is approximately 2 mN. For the scooping case, if the angle in contact with the water is assumed to be $\pi/2$ (meaning the tongue is submerged twice as deep) with all other parameter the same for dipping, the

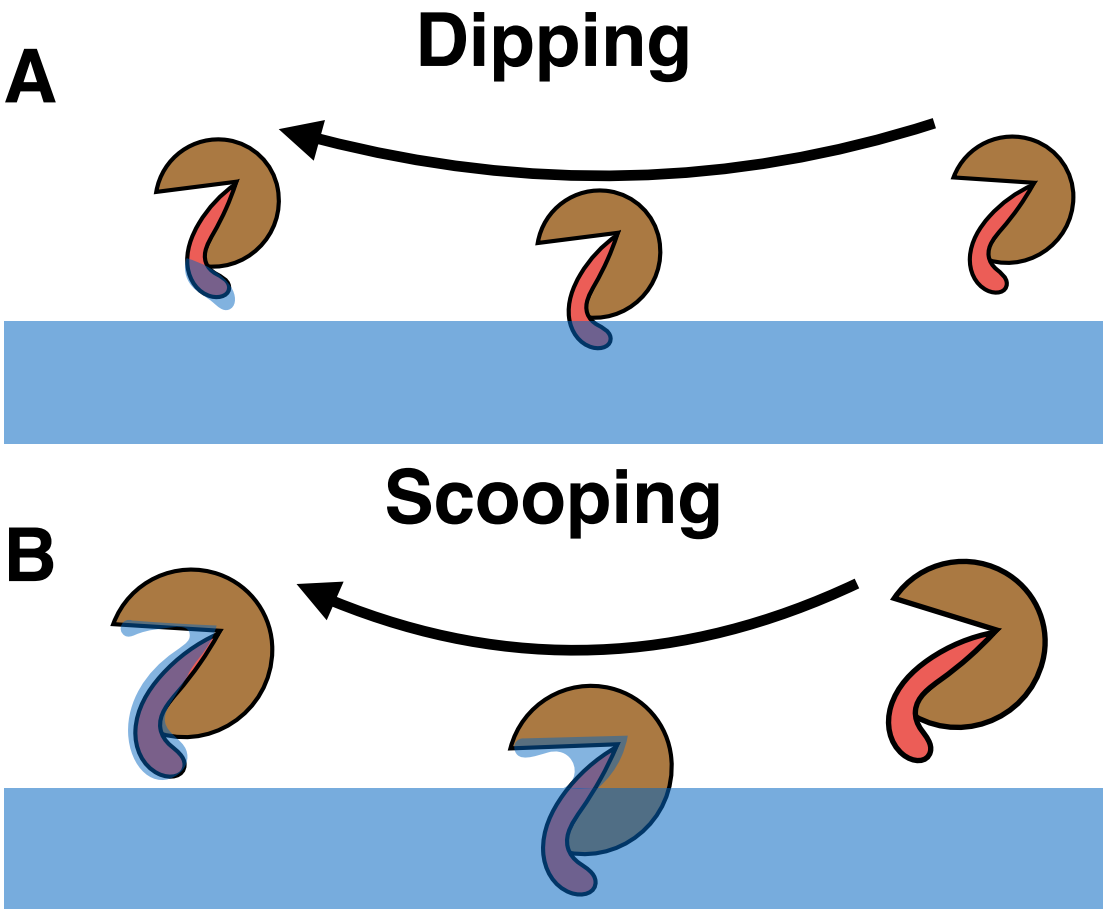

Figure 4.8: A) A cartoon bat dips its tongue into the water as it flies over the surface to drink. Upon exiting the bath, just the tongue is coated with water. B) The bat lowers its most of its bottom jaw into the bath to scoop the water into the mouth. Here, lots of water splashes into and coats the mouth.

drag force on the bat is approximately 24 mN. The bat weighs 20 grams, therefore it has to generate approximately 200 mN of lift force to fly. Increasing the scooping depth by a factor of 2 increases the drag force from 1% of the lift force to 12% of the lift force.

Because of the large force increase with depth, the bat may want to keep the mouth out of the water to avoid the rather large perturbation that occurs during water impact. Additionally, when the jaw is submerged the nose leaf of the bat comes very close to the water surface. The nose leaf of the greater horseshoe bat is used during echolocation and if it were to get wet it could disturb its ability to echo-locate water, obstacles, and insects while hunting and flying. Therefore, the bat is likely to be more cautious to avoid a potentially fatal mistake like tumbling into a water source.

Using the side view shown in Figure 4.3, the position of the tongue tip and wrist canalso be tracked as the bat flies across side the camera view. Points are digitized manually using the Matlab image processing toolbox. In this view the wing tip position cannot be tracked as it goes out of frame frequently. Footage from the GoPro cameras that is used to track wing tip position is presented later. Figure 4.10 shows the vertical position of the wing wrist and the tongue tip during a drinking attempt. It can be clearly seen from this view that the vertical motion of the wrist and tongue are approximately 180 degrees out of phase. As the bat raises its wings during the upstroke, the mouth drops towards the water surface and during the downstroke the head position is raised. Due to this motion the bat tended to make two "dips" during a drinking attempt in which the tongue or mouth impacted the water, was raised out, and then plunged back into the water a second time. If the penetration of the

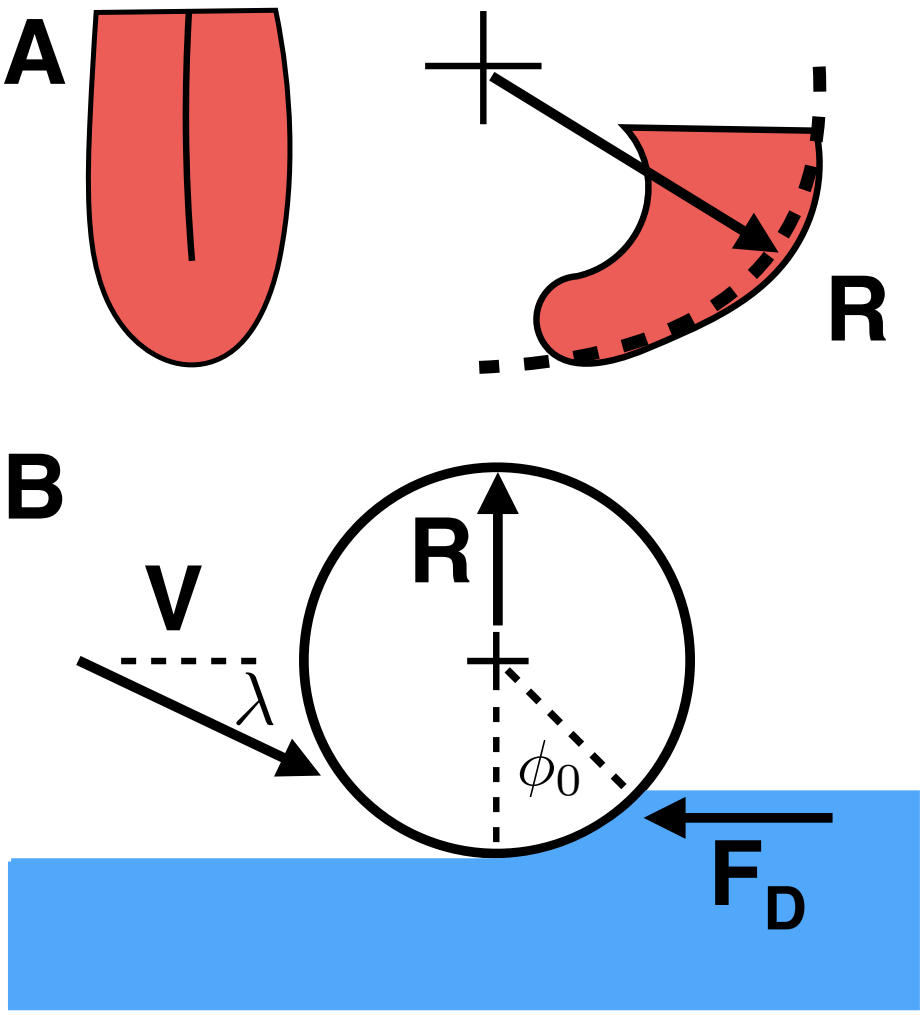

Figure 4.9: A) Front and side view of the bat tongue, recreated from high speed camera images. B) The tongue is approximated as a spherical skipping stone with radius R, angle of impact λ, speed V, and angle of water contact ϕ_0. The drag force on the sphere is shown as F_D.

mouth and tongue was far below the surface the bat never raised the tongue out of the water between the two dips.

4.6 Discussion

In this study we have explored how bats drink water while flying, a highly unique behavior in nature. The bats swoop down to the water surface while continuing to flap their wings, extend the tongue, and drag the tongue and mouth across the water. While drinking, the bat elevates the tips of the wing high above the shoulder on the upstroke, while descending the wing tips to just above the shoulder on the downstroke to avoid wing impact with the water. When the bat is flying away from the water bath it is able to extend its wings well below the body during the downstroke and does not raise the wings as high above the shoulder. It is seen that the advance ratio for the bat for drinking is much lower than for level flight, and is on the same order as rising flight, indicating that flying is relatively inefficient while the bat drinks. To drink, the bat touches its tongue and mouth to the water surface to coat the tongue and mouth and eventually swallow the water. Finally, bats are seen using two types of drinking mechanisms, scooping and dipping. During scooping, the bat submerges most of the jaw under the water surface. For dipping, the bat only touches its tongue to the water surface. It is assumed that the bat would want to use the scooping mechanism as it splashes much more water into the mouth, however, due to high drag and concerns about wetting its echolocation apparatus, it only uses the scooping method about 50% of the time.

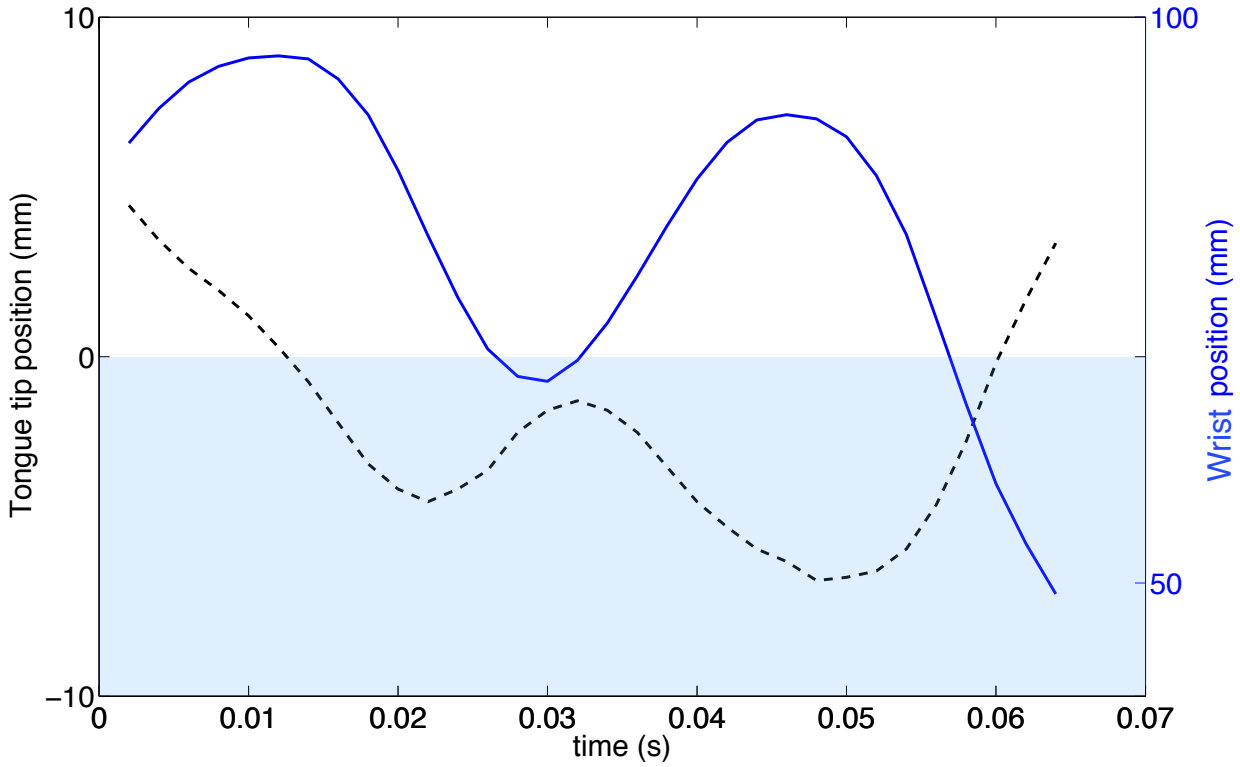

Figure 4.10: Vertical position of the wing wrist and the tongue tip during drinking. The left axis and black dashed line shows the tongue tip position with respect to the water surface and the right axis and blue line shows the wing wrist position with respect to the water surface. As the wing starts to move downward the tongue tip reaches its lowest position for that wing beat cycle. The data presented is smoothed.

One question that remains to be answered is whether or not the bat is able to swallow water without closing the mouth. We observed that the bat did not close its mouth, presumably to swallow water, until it was well away from the water basin. The bat could be drinking more water than previously thought if it is able to swallow as the water is splashed into the mouth. How bats swallow fluids should be investigated to further the understanding of the drinking mechanism. We also use a very simple model to estimate the drag force on the bat when it drinks. It may be useful to 3D print the bat's mouth and tongue shape from CT scan data to run experiments and measure the exact force that bat experiences.

Chapter 5

Crown splashes due to rod impact

5.1 Introduction

When a dog drinks it extends the tongue, curls it backwards into a ladle shape, impacts the water surface, and quickly retracts the tongue back into the mouth. During the tongue extension and impact there is often a jet that travels up and coats the tongue with water (seen in Figure 5.1B). This jetting could help increase the amount of water a dog can ingest per lap by increasing the surface area on the tongue coated by water. The impacting tongue is analogous to a rounded object impact a fluid surface (Figure 5.1A-B), therefore, we have decided to investigate the rising jet on the tongue by impacting a rounded rod on a a fluid surface. When the jet rises up the cylinder an instability is formed that is similar to the well studied crown splash. The rod impact problem combines aspects of drop spreading,

liquid-liquid impact producing crown splashes, and solid-liquid impact.

Several studies have investigated the spreading and subsequent instability that occurs during impact on a surface. When a drop is spreading on a surface there is a rapid deceleration of the spreading rim that gives rise to an instability that can also form secondary jets and droplets similar to a crown splash. Allen [58] claimed that the fingering that results from a droplet impact on a dry surface is due to the Rayleigh-Taylor instability. More recently, Thoroddsen et al. [59] studied the evolution of the fingering pattern during droplet spreading and also claimed that the number of fingers is governed by the Rayleigh-Taylor instability and show that the number of fingers does not change the diameter increases during impact. Bremond and Villermaux [61] found the Rayleigh-Plateau mechanism to be dominant in the rim instability produced by two impacting jets. Additionally, depending on fluid and surface parameters along with ambient air pressure, droplets can either spread smooth over a surface or lift off of the surface and form a corona splash [60].

An object impacting a fluid surface has been investigated with regards to ship slamming [48, 49, 50, 51], skipping stones [52, 53], and the water entry of spheres, cylinders, and disks [54, 55, 56, 57]. Depending on impact speed, object geometry and surface properties, as well as fluid properties many different behaviors are observed. When a wedge impacts a fluid surface a large vertical spray is formed due to impulsive motion of the fluid [50]. A sphere can create a large air cavity upon impact if its impact velocity is high or its surface is hydrophobic and low impact and low contact angle spheres will impact a surface with no cavity formation [54]. Impact of a flat disk onto a free surface also causes a splash similar

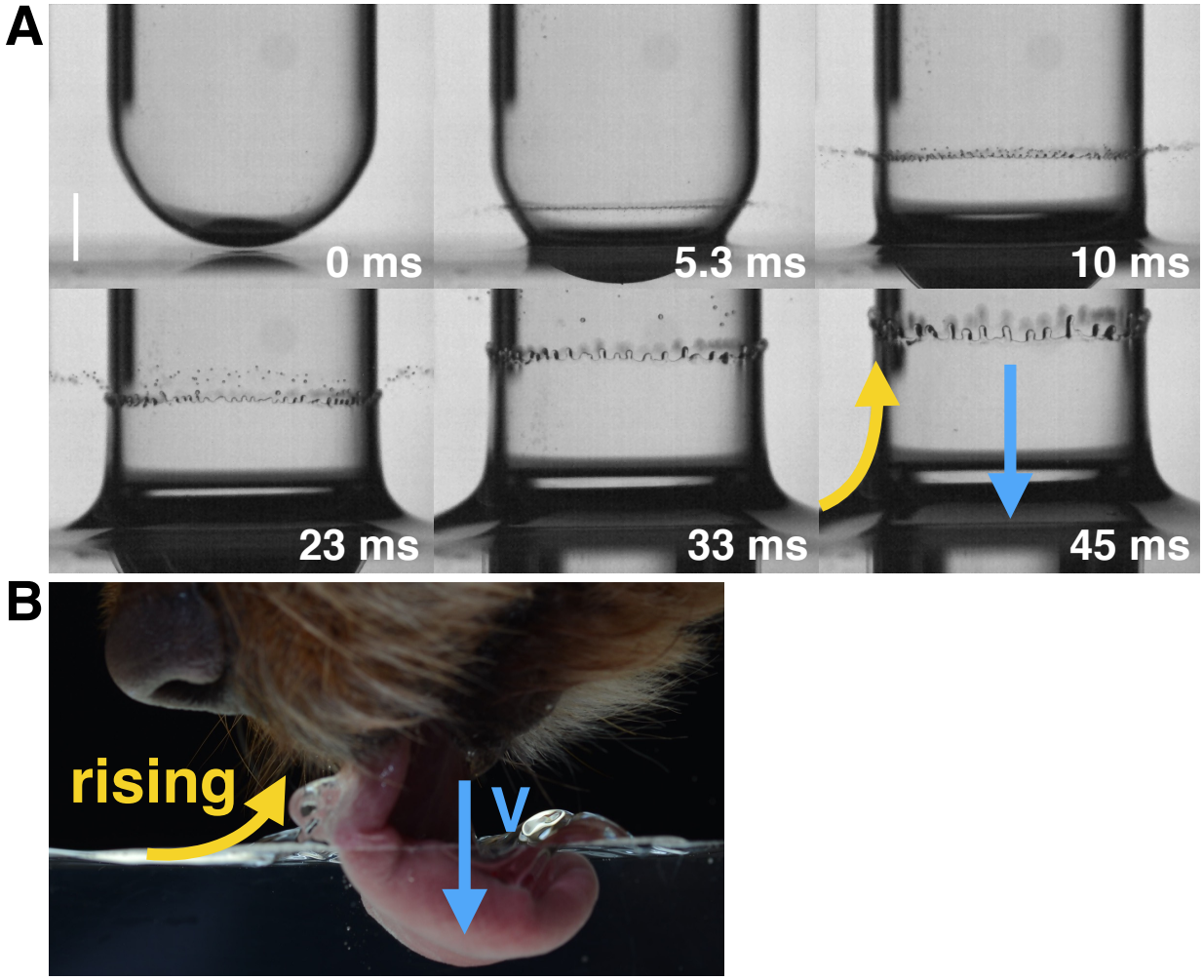

Figure 5.1: A) Rounded rod impact produces a crown splash. A 40 mm diameter rod impacts the water surface at 1.83 m/s. After impact, a thin fluid jet climbs up the side of the rod while ejecting micro-droplets. As the jet climbs it decelerates and the amplitude of the crown fingers grows until the jet reaches its maximum height and starts to fall back down.B) Fluid rises up a dog's tongue after water impact.

to the crown splash observed when a droplet impacts a thin layer of fluid [57].

The crown splash is a widely studied phenomenon that is typically known to occur when a drop impacts a thin layer of fluid and produces sheet-like jets that often eject secondary droplets similar to Figure 5.1A. Crown splashes have been observed as far back as 1897 by Worthington [129]. Before the crown is formed, a smooth sheet extends upwards and as the sheet extends surface tension pulls the leading edge of the sheet and starts accumulate fluid in a rim. The rim then develops an instability that can grow and produce secondary jets that break off into droplets.

The mechanism of instability formation of a thin sheet moving through air or over a surface has also been investigated for many years. Three mechanisms arrise most often in these studies, Rayleigh-Plateau [64], Rayleigh-Taylor [66, 58] and Richtmyer-Meshkov [65] instability theory. Rayleigh-Plateau theory states that a free cylinder of fluid in air breaks up into droplets due to surface tension. Rayleigh-Taylor theory shows how an instability is formed at the interface between two fluids due to density differences or deceleration of the denser fluid. Richtmeyer-Meshkov theory states that instabilities are formed due to impulsive acceleration of liquid. It has been argued by Krechetnikov and Homsy [65] that for a crown splash, the Richtmeyer-Meshkov instability dominates at early times scales and sets the instability wavelength while at later times when the rim is decelerating the Rayleigh-Taylor mechanism amplifies the instability. In a later study Krechetnikov [66] also stated that the instability on a liquid sheet edge cannot just be considered as a linear superposition of the Rayleigh-Plateau and Rayleigh-Taylor modes. It is the interplay of these instabilities that

determines the behavior of a sheet.

In this study, we investigate the jetting behavior and subsequent crown splash instability formed by impact of a round rod onto a fluid surface. This impact instability shares characteristics with both crown splashes and droplets spreading on a flat surface, however; the splash instability on a moving cylinder has yet to be explored. When a rounded rod with a hydrophilic surface impacts a fluid bath under certain conditions fluid rises upward along the rod surface. As the fluid climbs, a rim is formed, an instability develops, and a crown splash is created as shown in Figure 5.1A. The fluid behavior shows characteristics of both the crown splash from a drop impact on a thin fluid layer and of droplet impact and spreading on a solid surface. Specifically, we analyze the wavelength selection of the crown instability and the splash regime formed by the impact of a rounded rod on a liquid bath.

5.2 Experimental methods

Glass test tubes from Ace Glass, Inc. with diameters ranging from 10 to 40 mm are attached to a guide rail and dropped into a clear acrylic tank filled with water, ethanol, or a glycerin/water mixture. The impact speeds ranged from 0.3 to 3 m/s and the speed remained constant during the lamella rise. Prior to each test section the rods are cleaned with isopropyl alcohol and no surface coatings are applied to the rod afterwards. To stop the motion of the rod two springs are tethered to the apparatus that engage well after the initial splash behavior has subsided.

Rod impact was filmed with an IDT N3 high-speed camera at 3000 frames/s. The velocity of the rod was measured by tracking the tip motion using cross-correlation feature detection in Matlab. Several trials were completed with a random dot pattern inserted to determine if the rod decelerates as it penetrates the water surface. The rod velocity during these trials was measured using open source Prana PIV software developed at Virginia Tech [67] and shows that rod maintains a relatively steady velocity while the crown is formed (only ∼4% change, see Figure 5.2). Relevant non-dimensional numbers for a solid object impacting a liquid bath are the Reynolds number $Re = (\rho V D/\mu)$, the Weber number ($We = \rho D V^2/\gamma$), and the Froude number $Fr = \left(V/\sqrt{gD}\right)$, where D is rod diameter, V is rod impact velocity, γ surface tension, and μ viscosity.

5.3 Splash behavior

When a rod impacts a liquid surface there are three types of splashes observed: a capillary wave that is pushed away from the rod, a crown splash that rises up the side of the rod after impact, and a crown splash that ejects droplets. Variations in splash behavior are also seen for drop impact on a surface [88, 60] and for crown splashes due to liquid-liquid impacts [63, 64]. Splash behaviors depend on some combination of the Reynolds (Re), Weber (We), and Froude (Fr) number of impact. At small Re, We, and Fr numbers a capillary wave is formed. At intermediate values a crown splash with no ejected droplets is created and at higher values a crown that ejects droplets is created. The splash phase plots can be seen in

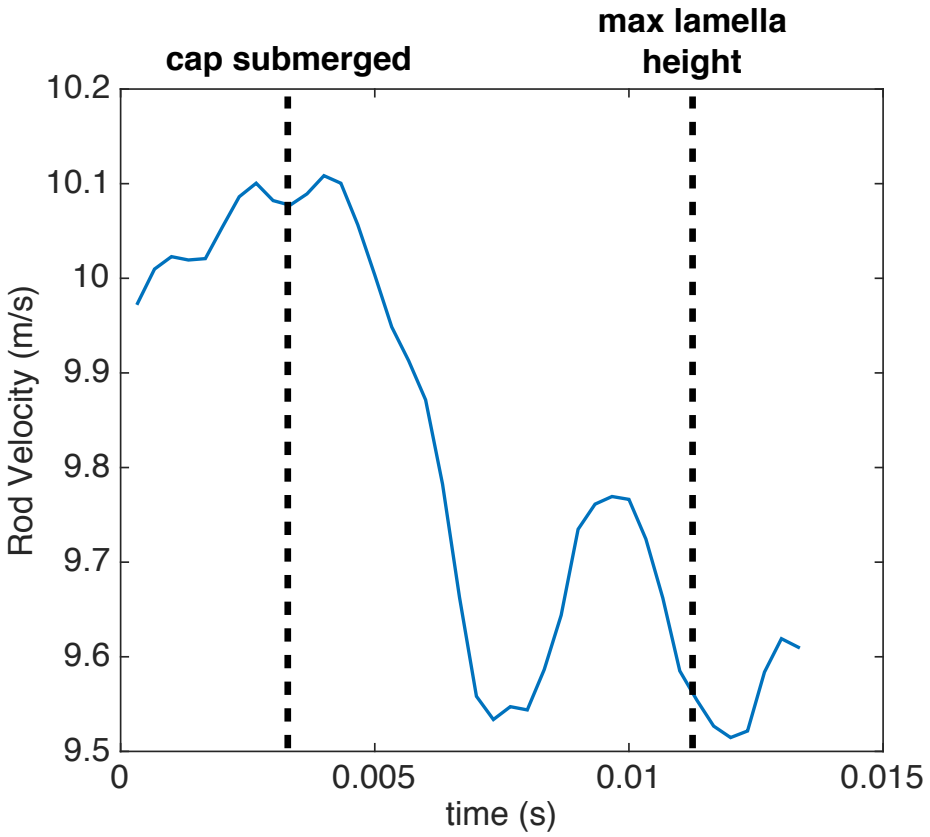

Figure 5.2: The velocity of a rod as it impacts the fluid surface. Time zero is the time when the rod first touches the fluid. The rod diameter is 11 mm. There is a slight decrease in impact speed after the hemispherical cap is submerged but the change is only 4% of the original imapct velocity.

Figure 5.3A-B. When droplets are ejected, both medium size, and very small droplets are produced, similar to behaviors observed in [63]. Drops are ejected due to fast growth rate of the instability causing ejection to occur before the sheet starts to retract. These results suggest that a dog would want to impact its tongue on the water at a high speed in order to get the jetting and crown splash behavior seen in experiments. The water jet (or lamella) would be able to coat more of the tongue in water whereas at low impact speeds a capillary wave is just pushed away from the tongue and water coats only the part of the tongue in contact with water.

5.4 Formulation of an instability problem

Next we want to predict the wavelength of the instability formed when fluid rises up cylinder after impact. The following analysis is a modification of theory presented in [68] that combines both Rayleigh-Plateau and Rayleigh-Taylor analysis of a sheet moving over a surface. Start by considering a straight rim with a semi-circular area, $A = \frac{\pi}{2}a^2$ where a is the rim radius, attached to planar sheet with thickness, h, as seen in Figure 5.4. Small disturbances with amplitude (ϵ) of the rim centerline, $y = Y(x,t)$ are considered. The rim is traveling with velocity, $\mathbf{V} = u\mathbf{e_x} + V_R\mathbf{e_y}$, and the sheet is considered to be moving with velocity V_S. The linearized mass balance, axial momentum balance, and moment of momentum equations

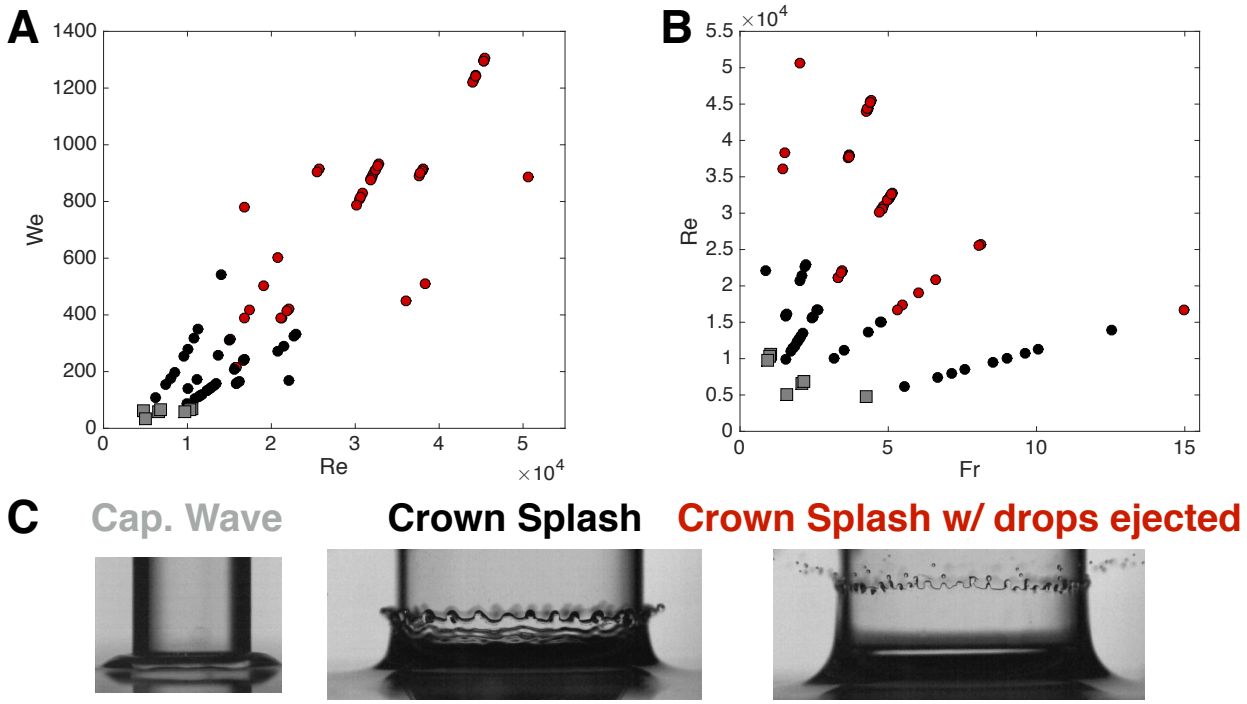

Figure 5.3: A) Weber number versus Reynolds number of rod impact. Grey points correspond to capillary waves, black points to crown splashes, and red points to crown splash with droplet ejection. B) Reynolds number versus Froude number of rod impact. C) Examples of each type of splash behavior: capillary wave, crown splash, and crown splash with droplets.

for the rim are

$$\frac{\partial A}{\partial t} + A_0 \frac{\partial u}{\partial x} - h\left(V_S - V\right) = 0 \tag{5.1a}$$

$$\rho A_0 \frac{\partial u}{\partial t} - \frac{\partial P}{\partial x} - \mathbf{f}_s \cdot \mathbf{e}_x = 0 \tag{5.1b}$$

$$\rho A \frac{\partial V}{\partial t} - P\kappa - \frac{\partial Q}{\partial x} - \mathbf{f}_s \cdot \mathbf{e}_y = 0 \tag{5.1c}$$

$$\rho \frac{\partial L}{\partial t} - \frac{\partial M}{\partial x} - Q - m_s = 0, \tag{5.1d}$$

where ρ is fluid density, $P = \pi\sigma a + \sigma A_0 \frac{\partial^2 a}{\partial x^2}$ is the longitudinal force on the rim, $\mathbf{f}_s$ is the distributed froce applied to the rim, κ is the curvature of the rim centerline, Q is the shear force in the y direction applied to the rim cross-section, L is the angular momentum of the rim per unit length length, M is the moment of cross-sectional stress, and m_s is the distributed moment of the external forces $\mathbf{f}_s$. The angular momentum and angular velocity of the rim are

$$L = I_0 \Omega, \ \Omega = \frac{\partial V}{\partial x} \tag{5.2}$$

where $I_0 = \pi a_0^4/8$ is the second moment of area of the cross-section. There is a pressure gradient in the rim cross-section that produces the moment of stress $M = -\rho I \dot{V}$ in the y direction. The distributed force on the rim is due to surface tension on the sheet surface and

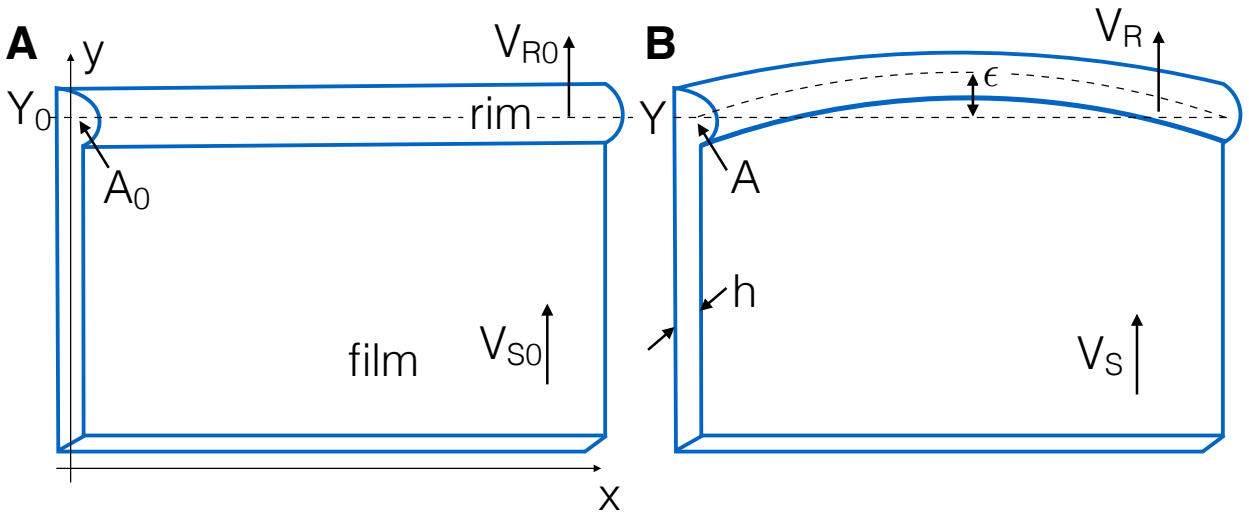

Figure 5.4: A) Base state of a rim and sheet of fluid moving over a surface. B) The rim is perturbed with amplitude ϵ. The model is adapted from [68].

inertia from fluid entering the rim

$$\mathbf{f}_s = \left[\rho h(V_S - V)^2 - 2\sigma\right]\mathbf{e}_y + \left[-\rho h(V_S - V)u + 2\sigma\frac{\partial Y}{\partial x}\right]\mathbf{e}_x. \tag{5.3}$$

The distributed moment of $\mathbf{f}_s$ is

$$m_s = -\rho h a_0 (V_{S0} - V_{R0})u. \tag{5.4}$$

The rim is disturbed in the form

$$Y = Y_0(t) + \epsilon(x,t),\ a = a_0(t) + \alpha(x,t). \tag{5.5}$$

Now we can substitute the perturbations in Equation (5.5) into Equations (5.1) and linearize

to get the first order system:

$$\pi a_0 \alpha_t + A_0 u_x + h\epsilon_t = 0, \tag{5.6a}$$

$$-\rho A_0 u_t + \pi/2\sigma\alpha_x + \sigma A_0 \alpha_{xxx} - W_0 u + 2\sigma\epsilon_x = 0, \tag{5.6b}$$

$$-\rho A_0 \epsilon_{tt} - \pi\rho a_0 \dot{V_0}\alpha + \pi/2\sigma a_0 \epsilon_{xx} + Q_x - 2W_0\epsilon_t = 0, \tag{5.6c}$$

$$2\rho I_0 \epsilon_{xtt} + \rho\frac{dI_0}{dt}\epsilon_{xt} + \pi\rho a_0^3 \dot{V_0}\alpha_x + a_0 W_0 u - Q = 0, \tag{5.6d}$$

where

$$W_0 = \rho h(V_{SO} - V_{RO}), \tag{5.7}$$

and

$$\frac{dI_0}{dt} = \frac{a_0^2 W_0}{4}. \tag{5.8}$$

The set of differential equations in (5.6) can be solved by assuming rim perturbations in the the form of

$$\epsilon = \epsilon_0 e^{\omega t + ikx},\ \alpha = \alpha_0 e^{\omega t + ikx},\ u = u_0 e^{\omega t + ikx},\ Q = q_0 e^{\omega t + ikx}, \tag{5.9}$$

where ω is the instability growth rate and $k = 2\pi/\lambda$ is the wavenumber (with λ as the wavelength).

Next, Equations (5.6) are reduced to the form

$$\mathbf{A} \cdot \mathbf{b} = 0, \tag{5.10}$$

where

$$A = \begin{pmatrix} \pi a_0 \omega & A_0 ik & h\omega & 0 \\ \frac{\pi}{2}\sigma ik - \sigma A_0 ik^3 & -W_0 - \rho A_0 \omega & 2\sigma ik & 0 \\ \pi \dot{V}_0 \rho a_0 & 0 & \rho A_0 \omega^2 - \frac{\pi}{2}\sigma a_0 k^2 - 2W_0 \omega & ik \\ \rho \frac{\pi}{2} a_0^3 \dot{V}_0 ik & aW_0 & 2\rho I_0 \omega^2 ik + \frac{a^2}{4W_0}\omega ik & -1 \end{pmatrix} \tag{5.11}$$

and

$$b = (\alpha_0 \ u_0 \ \epsilon_0 \ q_0)^T . \tag{5.12}$$

To find the dispersion relation the determinant of A is set equal to 0 to give

$$\begin{aligned} &\bar{\omega}^4 \left(-4\pi^2 - 2\bar{k}^2\pi^2\right) + \bar{\omega}^3 \left(-24\pi\bar{W}_0 - 6\bar{k}^2\bar{W}_0\right) + \\ &\qquad \bar{\omega}^2 \left(-2\bar{k}^2\pi^2 - \bar{k}^4\pi^2 - \bar{k}^6\pi^2 + 8\bar{h}\pi\bar{\dot{V}}_0 + 4\bar{k}^2\pi\bar{\dot{V}}_0 - 32\bar{W}_0^2 - 4\bar{k}^2\bar{W}_0^2\right) + \\ &\quad \bar{\omega} \left(-8\bar{h}\bar{k}^4\bar{W}_0 - 7\bar{k}^4\pi\bar{W}_0 - \bar{k}^6\pi\bar{W}_0 + 16\bar{h}\bar{\dot{V}}_0\bar{W}_0 + 8\bar{k}^2\left(-4 + \bar{h} + \bar{h}\bar{\dot{V}}_0\bar{W}_0\right)\right) + \\ &\qquad\qquad 2\bar{k}^4\pi^2 - 2\bar{k}^6\pi^2 - 16\bar{k}^2\pi\bar{\dot{V}}_0 - 8\bar{k}^4\pi\bar{\dot{V}}_0. \end{aligned} \tag{5.13}$$

The dispersion relation has been non-dimensionalized like

$$\omega = \sqrt{\frac{\sigma}{\rho a_0^3}}\bar{\omega},\ k = \bar{k}/a_0,\ h = \bar{h}a_0,\ \dot{V}_0 = \frac{\sigma}{\rho a_0^2}\bar{\dot{V}}_0,\ W_0 = \bar{W}_0\sqrt{\rho\sigma a_0}. \tag{5.14}$$

Next, the experimental wavelength and amplitude of the instability was measured using Matlab image processing techniques. Adaptive thresholding was used to detect the edge of the instability and the edge of the rod. The peaks of each of the secondary jets was found and since the location of the rod edge is known, simple geometry was used to calculate the wave length of the instability (see Figure 5.5). The wavelength data presented below is measured at maximum lamella height. θ can be calculated as

$$\theta = \arccos\frac{R-\delta}{R}, \tag{5.15}$$

and then wavelength between peaks one and two is

$$\lambda = R\left(\theta_2 - \theta_1\right). \tag{5.16}$$

The dispersion relation for values of $\bar{\dot{V}}_0$ from 0.05 to 1.2 as measured in the experiment are shown in Figure 5.6B. Figure 5.6D shows that this dispersion relation captures our experimental data well for a large range of $\bar{\dot{V}}$. For ethanol trials with small $\bar{\dot{V}}$ values the dispersion relation over predicts ka. This could be due to slight measurement errors of the rim radius as $\bar{\dot{V}}$ bar goes like $1/a_0^2$.

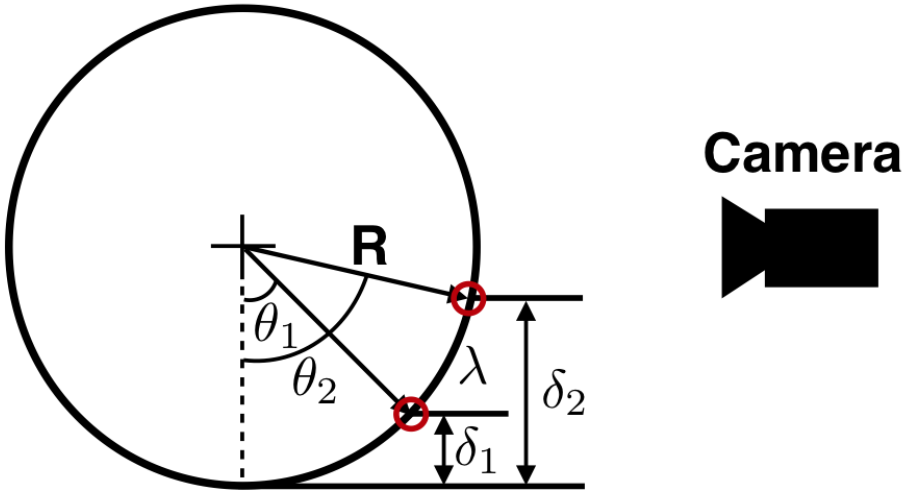

Figure 5.5: Top down view of rod to calculate the instability wavelength. Locations of the maximum amplitude of the instability are shown with red circles. The camera sees the view of the instability shown in Figure 5.1. Since the radius of the rod is known, and each wave peak distance from the edge, δ, can be found from the images, the angle of the wave peak and then the arc length between two peaks can be found. Wave peak locations are exaggerated for figure clarity.

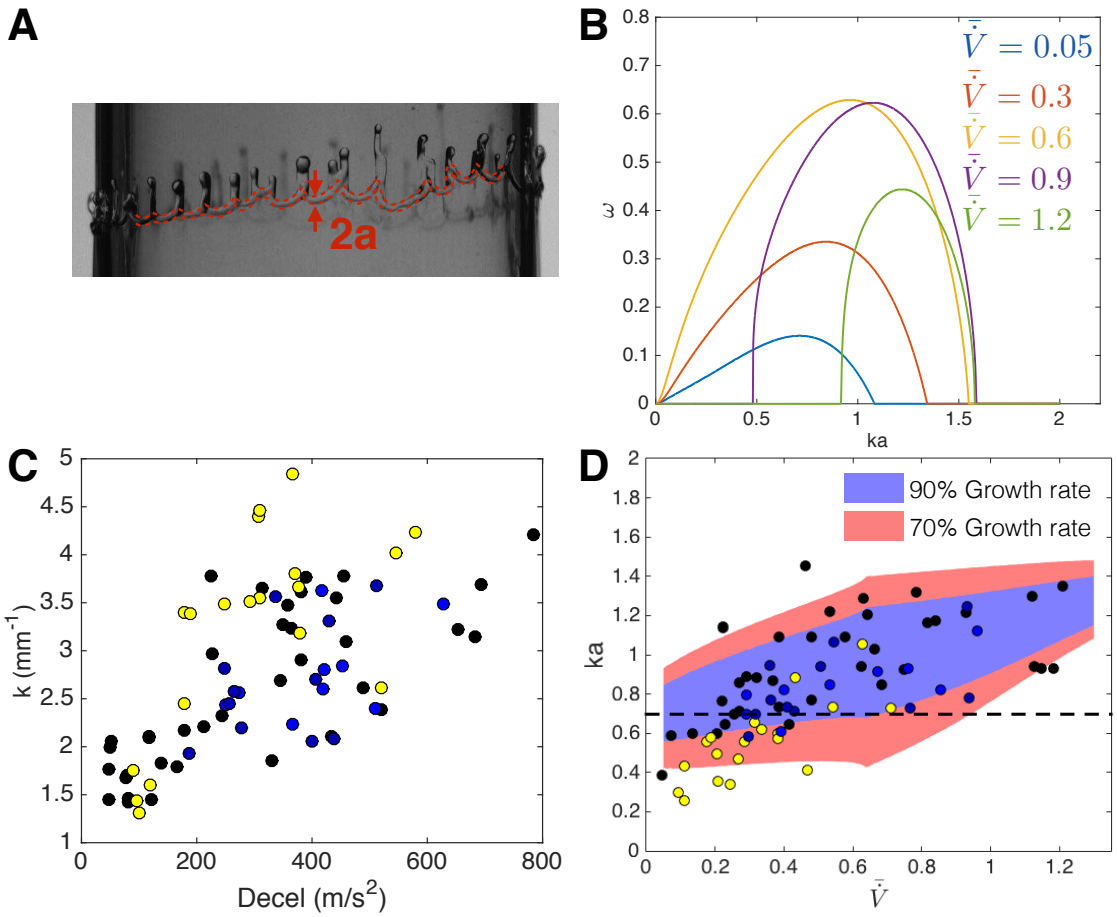

Figure 5.6: A) The radius of a rim, a, formed by a jet rising up the cylinder is highlighted by the red dashed line. For the results presented here, a was always measured at maximum lamella height. B) Instability growth rate versus wavenumber times rim radius for a decelerating rim moving over a surface attached to a sheet of fluid. $\bar{\dot{V}}_0$ is the non-dimensional deceleration shown in Equation (5.14). Experimental values of $\bar{\dot{V}}_0$ ranged from 0.05 to 1.2. C) Wavenumber k versus deceleration of the rim. D) Wavenumber multiplied by rim radius ka versus rim deceleration. The shaded blue region corresponds to the ka range at 90% of the maximum instability growth rate and the red shaded region corresponds to 70% of the maximum growth rate.

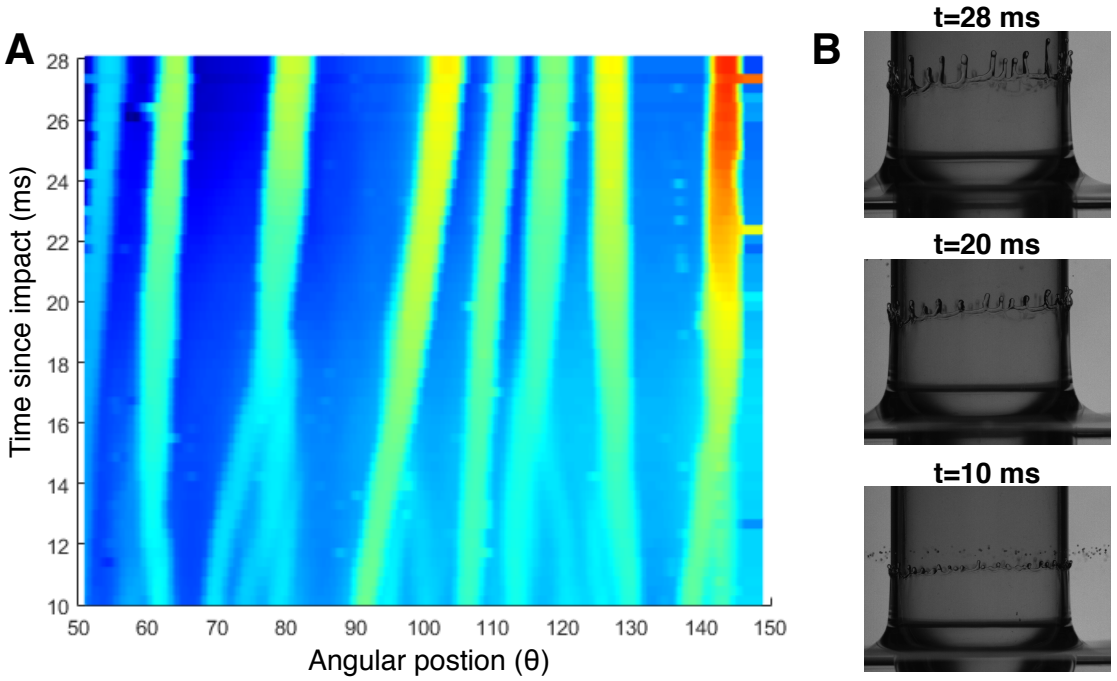

Figure 5.7: A) Spatio-temporal evolution of the instability amplitude and wavelength as it rises up the side of a cylinder. B) Snap shots of the instability. Times correspond to those in (A). The rod has a radius of 11 mm and impacted the water bath at a speed of 1.2 m/s.

5.5 Time evolution of the lamella

The spatio-temporal evolution of the instability is also measured. When the fluid jet is first formed, the wavelength of the instability is small and increases over time. This behavior was also observed for crown splashes in [64]. As seen in Figure 5.7 after the initial merging of waves, the wavelength does not change for at least 10 ms. The amplitude of the instability continues to grow until the rim of the lamella starts to move back down towards the bath.

5.6 Conclusion

In summary, inspired by a dog's tongue impact on a fluid surface we have discussed the types of splashes seen when a rounded rod impacts a body of water. Depending on the Reynolds, Weber, and Froude numbers, a capillary wave, a crown splash, and a crown splash with droplet ejection can occur. Also, by modifying a model [68] of a fluid sheet moving over a surface, the wavelength of the crown splash instability that forms can be predicted. This theory combines Rayleigh-Plateau and Rayleigh-Taylor instability theory to predict the wavelength better than just a superposition of the two theories. We show the space-time evolution of the rim instability as it moves on the cylinder surface. Deceleration of the rim is not constant, which causes the wavelength to change as the rim moves along the surface. The wavelength of the instability grows over time, however, there are long times ($\sim$10 ms) where the wavelength remains the same until fingers merge. Finally, dogs could take advantage of the rising of the fluid after tongue impact to coat more of the tongue with water while it laps.

Chapter 6

Dynamics of squeezing fluids: clapping wet hands

6.1 Introduction

The atomization process of a liquid thread is observed in many industrial applications (e.g. coating [112], cooling, etc [113, 114]) and everyday life (e.g. raindrop formation [115], clapping wet hands). In particular, we have all experienced the splashing effects of clapping with wet hands. When water splashes, numerous water droplets, rather than fluid threads, are dispersed. Such a squeezing motion of the hands makes the fluid in between eject and eventually break into drops. This outburst of fluid motion is the primary motivation behind this study.

Drop formation from a fluid sheet has been observed and studied in two notable cases: a crown splash [116, 117, 118, 119, 120, 121] and a water bell [122, 123, 125, 126, 127]. In a crown splash, the crown shape of the fluid results from an instability along a cylindrical fluid-sheet forming due to transient fluid impact. In this process, a drop of a fluid is released and impacts a bath of the same fluid at rest or a solid substrate. After impact, a cylindrical sheet forms and moves upwards, eventually creating droplets along the edge of the fluid rim [128]. Liquid crowns of various geometries have been studied extensively; on a bulk of the same fluid [129, 121], on a solid wall [130, 131] on a thin fluid layer [64, 132], on a rod [133, 134], and more. The water bell [126, 127] is another example sharing some features with our study of clapping with wet hands i.e. the fluid rim connected to the sheet. When a continuous fluid jet hits a localized solid obstacle (i.e. a rod), the jet radially spreads and forms a circular sheet called a water bell [135]. Similar to the liquid crown, the water bell has the drop-formation mechanism in which the fluid sheet radially expands and breaks into smaller droplets.

Uniqueness of the proposed work, clapping wet hands, lies in these three points; First, the flowing fluid to liquid sheet is transient and follows the inverse power-law due to a lubricating flow between two plates, which is not observed in the other two cases. Second, the thick rim in this case expands radially in a different manner than other liquid sheets. All water-bells are steadily forming both a rim and a liquid sheet without temporal dynamics due to a continuous liquid feed. Finally, an undulatory thick rim is developed at an early stage and later gravity and radial expansion amplifies this rim's waveness. But, a crown splash

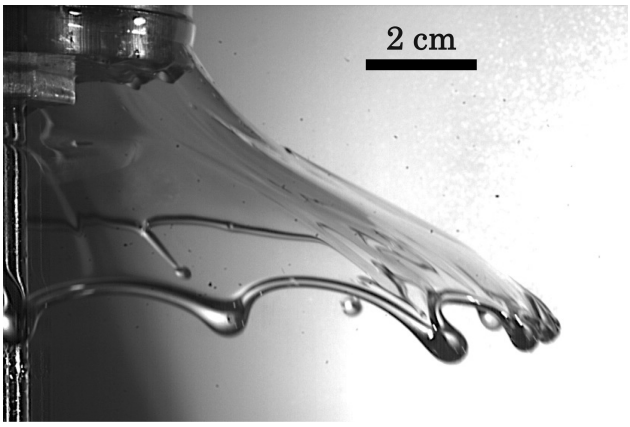

Figure 6.1: Image of a liquid sheet (silicone oil of 100 cSt) squeezed from two clapping plates at the velocity of 10.2 cm/s.

develops a decelerating liquid sheet against gravity and becomes unstable at later stage when it reaches close to its maximum position. Water-bells are either closing the fluid sheet at the lower end or splashing radially with a continuous jet.

In this paper, we investigate how a fluid sheet and rim develop and move due to the squeezing motion of disks, and how fluid droplets form from the rim due to the capillary instability as illustrated in Figure 6.1. Again, this study is motivated by the familiar act of clapping with wet hands, which has unique features compared to traditional splash problems e.g. crown splashes and water bells. First, Section 6.2 describes the experimental setup and procedure. In Section 6.3, we compare experimental data with three theoretical models: the lubrication flow, the ejecting dynamics and the capillary instability of the rim. Finally, we discuss the conclusion of our findings and the future direction in Section 6.4.

6.2 Experimental methods

The experimental setup is designed to understand and mimic the motion of clapping hands: a squeezing fluid motion caused by two circular disks (see Figure 6.2A). An upper disk is actuated to fall vertically at a fixed speed and eventually collides with a bottom disk. Both disks have the same radius (R_{disk} = 3.8 cm) and are aligned accurately in order to avoid any sliding motion. The impact speed (V_{disk}) of the upper disk varies from 5 to 13 cm/s, and is controlled by a linear actuator (Xslide XN10-0040-E04-71, Velmex Co.). The fluid motion is recorded at 1000 Hz by using either one MotionXtra N3 from the side or two Fastcam APX RS photrons from both the top and the side. The high-speed camera on the top is located approximately 2 m away from the disk to prevent any optical distortion. We experimented using silicon oil (Clearco Products) with kinematic viscosities ($\nu = \mu/\rho$; where μ is absolute fluid viscosity and ρ is fluid density) of 20, 50, and 100 cSt and surface tensions (γ) of 20.6, 20.8, and 20.9 dynes/cm respectively. We also used a mixture of 80% glycerol and 20% water of about 75 cSt to test a high surface tension fluid of 65.7 dynes/cm [136]. For each experiment, the same amount of fluid (7 mL) is first degassed and gently deposited on the top of the lower disk using a syringe to remove any initial bubbles in the bulk. The thin fluid layer deposited on the lower disk is about 1.5 mm in height.

The dimensionless parameters for describing the clapping hands experiment are the Reynolds number $\mathrm{Re} = V_{disk}R_{disk}/\nu$, the Weber number $\mathrm{We} = \rho V_{disk}^2 R_{disk}/\gamma$, and the Ohnesorge number $\mathrm{Oh} = \mu/\sqrt{\rho\gamma R_{disk}} = \sqrt{\mathrm{We}}/\mathrm{Re}$. Our experiments cover ranges of Oh = 0.02$\sim$0.1,

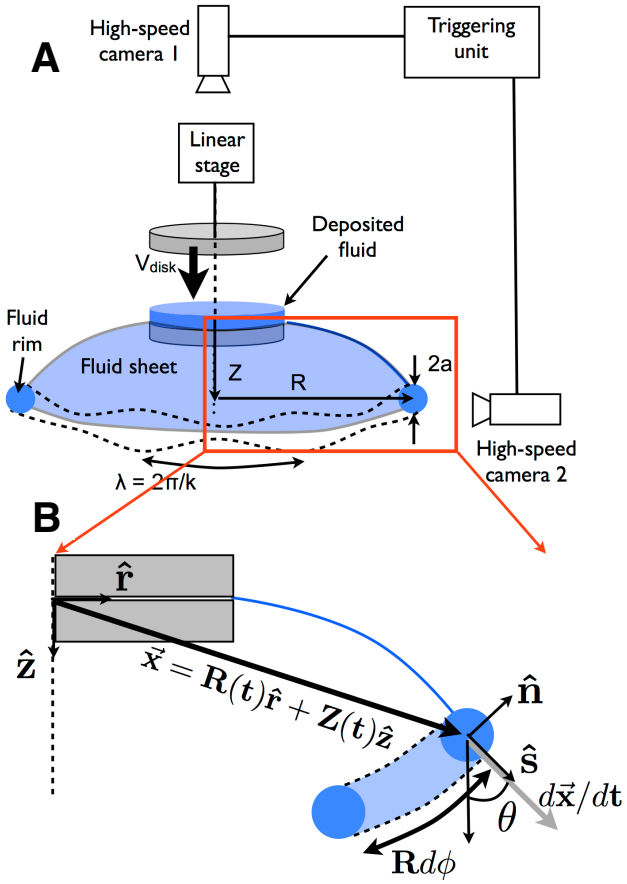

Figure 6.2: A) experimental apparatus and schematics of the sheet of fluid being ejected from the plates. B) zoomed schematics to explain coordinate system of the dynamics of a rim.

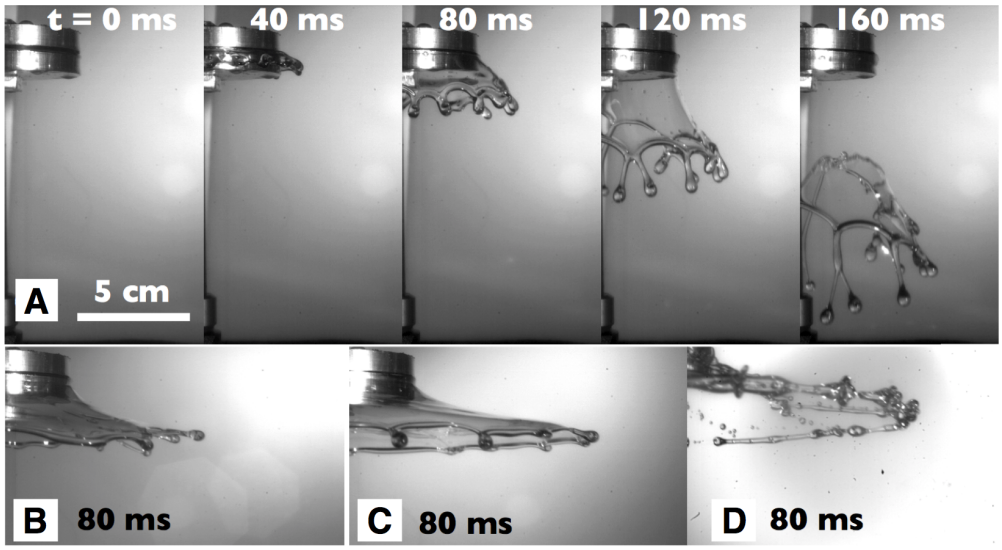

Figure 6.3: Side-viewed image sequences A) at $t = 0, 40, 80, 120$, and 160 msec with viscosity of 100 cSt and $V_{disk} = 5.08$ cm/s, at $t = 80$ msec with $V_{disk} = 12.70$ cm/s with viscosity of B) 100 cSt, C) 50 cSt, and D) at $t = 80$ msec with $V_{disk} = 12.70$ cm/s with 75 cSt water-glycerol mixture.

Re = 20∼200, and We = 2∼20.

When the two plates squeeze deposited fluids within about 10 to 30 msec, the fluid is ejected in a mostly radial direction through the small gap between the two plates. In the course of squeezing, a fluid rim is quickly formed in about 20 msec (capillary timescale; $t_{capillary} = \sqrt{\rho a^3/\gamma}$) on the edge of the sheet primarily due to surface tension. The measured rim radius (a) is about 2 mm, is independent of the disk speed, and close to the capillary length ($\sqrt{\gamma/\rho g} \approx 1.5$ mm). This indicates that the formation of the rim is mainly due to the capillary force and happens quickly in about 20 msec. In the intermediate stage, the rim and sheet curve down due to gravity and decelerate due to drag and surface tension (see images after t = 40 ms in Figure 6.3A). Eventually, an instability will be initiated along the rim and drops will form on the tip of the fluid rim as shown in the images at $t = 0, 40, 80, 120, 160$ ms in Figure 6.3A. Depending on fluid viscosities and clapping speeds, variations in the fluid sheet and rim are observed, as shown in Figure 6.3B-D.

Recorded images from the two high speed cameras are analyzed using the MATLAB image processing toolbox to determine the position, size, and wavelength of the fluid rim. This program analyzes the intensity of each rim radius; the radius is found by locating the largest peak in intensity and the location of this peak will be the distance between the rim and the disk center. Then, the program analyzes the luminosity around the rim versus the angle for a certain range of angles as the pictures are difficult to analyze on the whole semi-arc. These experimental results from image analysis will be discussed and compared with theoretical models in next section.

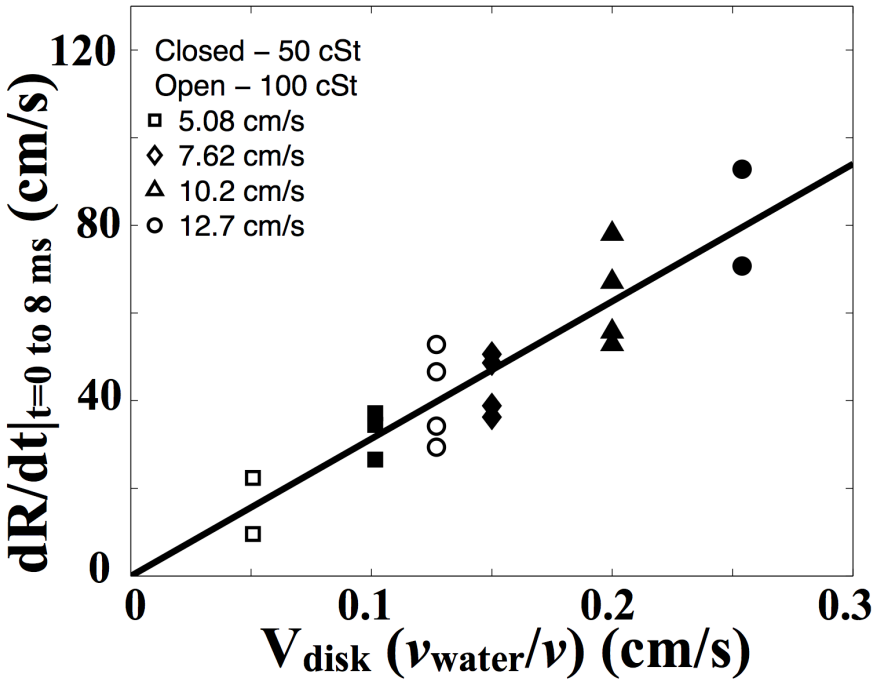

Figure 6.4: Initial radial velocity of the rim vs. normalized disk velocity with different viscosities. The solid line is the best fit line with $R^2 = 0.82$. Initial radial velocity is measured over an 8 msec interval just after the clapping.

6.3 Result

6.3.1 Squeezing flow: Early stage

When the upper plate strikes the thin fluid on the lower plate, the fluid splashes radially due to the squeezing motion of the two plates. Due to the small thickness of the fluid ($\sim$ 1.5 mm) and high fluid viscosity (20$\sim$100 cSt), the low-Reynolds number lubrication approximation [137] can be considered in our experiments. The impact force (F_0) from the upper disk is presumably proportional to the impact plate velocity (V_{disk}) [138], and is then

applied to compress the fluid in-between. We can assume that the total fluid volume is conserved ($R(t)^2H(t) = R_{disk}^2 H_0$), and then solve the lubrication equation with initial conditions ($H|_{t=0} = H_0$, $R|_{t=0} = R_{disk}$). The continuity equation in terms of radial and vertical velocities (v_r, v_z), and the non-trivial component (r) of the momentum in a cylindrical coordinate are written as

$$\frac{1}{r}\frac{\partial}{\partial r}(rv_r) + \frac{\partial}{\partial z}v_z = 0, \quad \frac{\partial P}{\partial r} = \mu\frac{\partial v_r}{\partial z^2}. \tag{6.1}$$

If one solves for the vertical velocity, then $P(r)$ yields

$$P(r) = -3\mu\frac{r^2}{H^3}\frac{\partial H}{\partial t}. \tag{6.2}$$

Integrating the pressure $P(r)$ over the plate surface ($r \in [0, R_{disk}]$ and $\theta \in [0, 2\pi]$) gives the force exerted by the plate

$$F_0 = \frac{3\pi\mu}{2}\frac{R(t)^4}{H(t)^3}\frac{\partial H}{\partial t}. \tag{6.3}$$

Finally, using the constant volume condition ($R(t) = R_{disk}\sqrt{H_0/H(t)}$) gives the fluid height

$$H(t) = H_0\left(1 + \frac{8}{3\pi\mu}\frac{H_0^2 F_0}{R_{disk}^4}t\right)^{-1/4}. \tag{6.4}$$

For reference, this height expression is different from other lubrication calculations using the constant contact area condition [139]. Combining with the linear relation of impact force

with disk speed [138], the initial radial velocity will be

$$\left.\frac{dR}{dt}\right|_{t=0} = \frac{H_0^2 F_0}{3\pi\rho\nu R_{disk}^3} \propto V_{disk}\frac{\nu_{water}}{\nu}\,. \tag{6.5}$$

It indicates that the initial radial velocity of the ejecting fluid is proportional to the clapping speed and inversely proportional to the fluid viscosity, which is in good agreement with the experimental observations with $R^2 = 0.82$ as shown in Figure 6.4.

6.3.2 Expanding Rim: Intermediate stage

One of the fascinating features in this experiment is the spreading of a thick fluid rim caused by the collision of two plates. The static shape of a closed fluid sheet, like a flowing fluid balloon, have been studied in [127, 135]. Here, we will develop our model for the rim dynamics by considering the various effects on a fluid rim in a coordinate system described in Figure 6.2B.

The mass of a small section of rim $\rho\pi a^2 R d\phi$ is moving in a curved trajectory where ϕ is the azimuthal angle in a cylindrical coordinate. Hence, the centrifugal force acts outwards as

$$\vec{F}_c = \rho\pi a^2 R d\phi \frac{|d\vec{x}/dt|^2}{R_c}\hat{n}\,, \tag{6.6}$$

where $\vec{x}(= R\hat{r} + Z\hat{z})$ is the position vector of a rim, $\hat{n}$ is the unit vector normal to the rim's trajectory, $R_c = (-d\theta/ds)^{-1}$ is the radius of curvature of the rim's trajectory, and the drag

force acts opposite to the rim's trajectory as

$$\vec{F}_d = -\frac{1}{2}\rho C_D |d\vec{x}/dt|^2 (2aRd\phi)\hat{s}\,, \tag{6.7}$$

where $\hat{s}$ is the tangential unit vector along the rim's trajectory, r is the radial distance of the rim, and C_D is the drag coefficient. There are different models of a drag coefficient describing drag on a drop or a liquid film [140], but we have chosen $24/\mathrm{Re}_{\mathrm{air}}$ using air kinematic viscosity for simplicity. Since a thin fluid sheet is connected to the back side of the rim, the tangential capillary force can be expressed as

$$\vec{F}_{\gamma 1} = -2\gamma R d\phi \hat{s}, \tag{6.8}$$

where the factor of 2 is due to the upper and lower sides of a liquid sheet. Also, the capillary force acts along the cylinder's surface due to the curved cylindrical rim. The resultant force points in the negative normal direction as

$$\vec{F}_{\gamma 2} = -\gamma a \frac{R}{R_a} d\phi \hat{n}\,, \tag{6.9}$$

where $R_a = R/\cos\theta$ is the azimuthal curvature of the rim. Lastly, gravity pulls the rim downward as

$$\vec{F}_g = \rho g \pi a^2 R d\phi \hat{z}. \tag{6.10}$$

After adding all above forces, we write the governing equation for the liquid rim as

$$\rho\pi a^2 R d\phi \frac{d^2\vec{x}}{dt^2} = \vec{F}_c + \vec{F}_d + \vec{F}_{\gamma 1} + \vec{F}_{\gamma 2} + \vec{F}_g \,, \tag{6.11}$$

Then, we can solve this equation numerically using the following boundary conditions: $R|_{t=0} = R_{disk}, z|_{t=0}, dz/dt|_{t=0} = 0$ and $dR/dt|_{t=0}$ is from the mean radial velocity in Figure 6.4 at given fluid viscosity and clapping speed as a result of lubrication force which is described in the previous section.

Simulation results are compared with experiments in Figure 6.5. Here, trajectories of only gravity (open squares), the full model solving Equation (6.11) (open circles), and experiments (closed circles) exhibit a similar parabolic profile. In experiments, the position of the end tip of the silicone oil sheet is tracked instead of the undulating rim-tips. We found that the rim trajectories solving Equation (6.11) including centrifugal force, drag, surface tension, and gravity are quite close to experimental trajectories. However, the parabolic trajectories ($R(t) = dR/dt|_{t=0}\, t$ and $Z(t) = \frac{1}{2}gt^2$) considering only gravity exhibit longer travel distances than the other two due to the lack of drag and surface tension, and rapid downward trajectories due to the lack of centrifugal force.

The numerical result solving Equation (6.11) still exhibits a slight mismatch with experiments especially at later times. One possible explanation is that our assumption of a smooth cylindrical rim is not valid at later times due to the capillary force causing the straight rim to undulate and further turn into drops. This drop formation due to the capillary action

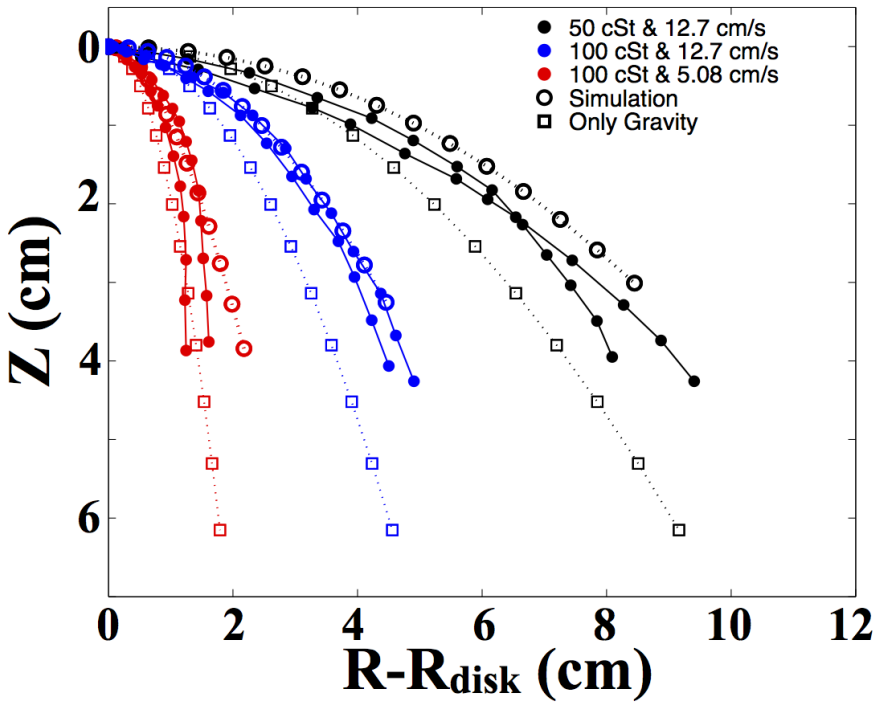

Figure 6.5: Positions of fluid rims with different velocities and viscosities. Open symbols are from experiments and closed symbols are from numerically solving Equation (6.1). Each line with different symbols shows a trajectory over 112 ms, and symbols are separated by 8 ms.

will be discussed in the next section.

To remark on the water-glycerol cases, experiments with a water-glycerol mixture show a very short fluid sheet life-time mainly due to high surface tension (see Figure 6.3D). Therefore, no water-glycerol data is presented in this rim-dynamics section.

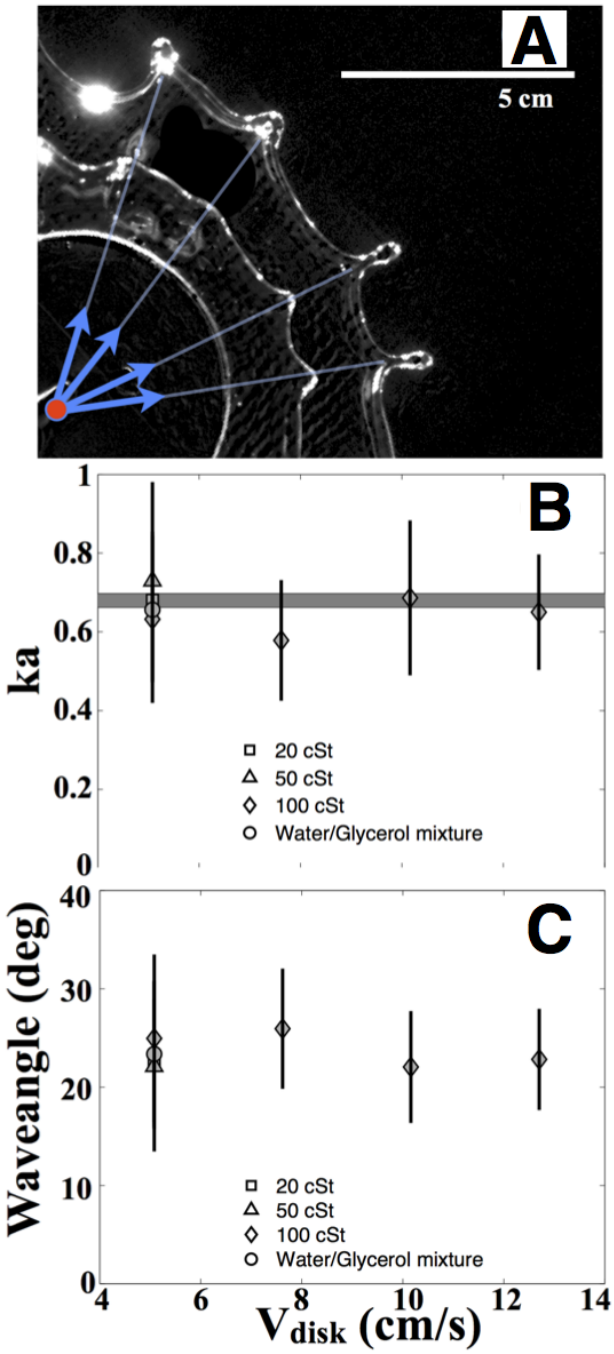

Figure 6.6: (A) Two super-imposed snap-shots at 30 & 70 msec with viscosity of 100 cSt and V_{plate} =12.7 cm/s. The invariable waveangle of undulations in the course of rim expansion. Plots of B) non-dimensional wavenumber (ka) and C) waveangle (ϕ in degrees) with different fluid viscosities and varying plate velocities. The gray area in (B) is the non-dimensional wavenumber predicted by the Rayleigh-Plateau instability with viscous effects.

6.3.3 Unstable rim: Final stage

The traditional Plateau-Rayleigh instability [141] shows that a cylindrical jet becomes unstable and breaks into droplets. In our case, although the rim is shaped like a torus, it can be approximated as a straight cylinder because the radius of the liquid sheet is much larger than the radius of the rim (about 100 times bigger). We also assume that the attached liquid sheet does not affect the instability of the rim.

In this falling cylindrical fluid rim, we evaluate three time scales to find dominant forces for the drop formation at later times in the frame moving with the rim. First, the capillary break-up time ($t_{capillary}$) scales as $\sqrt{\rho a^3/\gamma} \approx 20$ ms where the measured rim radius ($a \approx 2$ mm) is used. The next is the extension time which scales as $R/(dR/dt) \approx 0.1 \sim 1$ sec measured in experiments. Lastly, the viscous time scale ($a^2/\nu = 40 \sim 200$ ms) is slightly higher than the capillary timescale and lower than the extension timescale. Therefore, the primary force controlling the instability breaking a fluid rim into drops is the capillary force while the viscous force is a secondary cause of the instability. This viscous effect slows the dynamics of capillary instability, and weakly affects the most unstable mode as its growth rate is $(\omega)_{predict} = 1/(t_{capillary}(2\sqrt{2} + 6\mathrm{Oh}))$ and its unstable wavenumber is $(ka)_{predict} = 1/\sqrt{2 + 3\sqrt{2}\mathrm{Oh}}$ [143, 142].

In the experiments, we have observed apparent undulations from the smooth surface of the rim after approximately 15 ms, which is close to the capillary time scale. As this perturbation grows in time, clear drops hanging on a fluid rim are formed after about 80 ms. Within this

time scale, the rim becomes unstable due to the capillary force, however, the rim's position is not very far from the disk perimeter. Hence, the characteristic length scale is chosen to be the disk radius for further calculations.

Capillary instability sets an initial drop spacing in the beginning of this squeezing fluid on the order of the capillary timescale ($\sim$ 20 msec). Figure 6.6A shows the formation of both the undulating rim and drops from the top view. Locations of thick and protruding rim sections due to capillary force at the very beginning ($\sim$ 20 msec) further develop into drops as time goes on. While they fall downward and expand radially, this spacing does not change noticeably.

The Plateau-Rayleigh instability by considering viscous effects predicts $(ka)_{predict} = 1/\sqrt{2 + 3\sqrt{2}\mathrm{Oh}}$, where Oh ranges from 0.02 to 0.1 for silicone-oil experiments. While our experiment changes viscosity from 20 to 100 cSt (80% changes), the corresponding predicted $(ka)_{predict}$ range from 0.69 to 0.64 (only 7% changes). This result is compared with experimental measurements in Figure 6.6B.

Assuming small radial expansion of the rim when capillary force determines the most unstable waveangle, the Plateau-Rayleigh instability also predicts the wave angle as $(\phi)_{unstable} \sim \frac{2\pi a}{(ka)_{predict} R_{disk}} \sim \pi/6.32 = 28.5^o$, which is close to the mean value of measurements shown in Figure 6.6C. However, some distributions in measured ka and wavelangle are observed. One major source of uncertainty might come from the fluid rim interacting with a connected sheet and surrounding air. Due to small Ohnesorge numbers, the liquid rim is formed and propagates interfacial waves along the liquid sheet, and then this rim-sheet coupled system

become unstable [124, 144], which we do not take into account in this study.

6.4 Conclusion

In this paper, we have studied the dynamics of a fluid squeezed by two circular disks. First, the initial spreading velocity is estimated using lubrication theory. Secondly, the position of a rim is described by balancing inertia with drag, centrifugal, and surface tension forces. Finally, the most unstable wavelength (or wave angle) is estimated using the traditional Rayleigh-Plateau analysis of capillary instability. Experimentally, we have tested with different clapping speeds, fluid viscosities, and surface tensions to understand the effect of fluid and kinematic properties on the dynamics and have shown that theoretically predicted rim position and drop spacing are in good agreement with experimental measurements. This study explains how sparse droplets are generated when a fluid is squeezed. This study was published in Physical Review E and is titled "Dynamcis of squeezing fluids: clapping wet hands" [147].

Chapter 7

Discussion and future directions

7.1 Discussion

Our investigations were designed to explore interfacial fluid dynamics problems experienced and inspired by natural systems. We found that a leaf with a hydrophobic surface may be better protected from droplet impacts by studying the impact of a droplet on a cantilever with variable surface properties. Average torque for nonwetting beams is close to zero but increases with drop mass and beam length for wetting beams. Bending energy experienced by a beam due to droplet impact is also much higher for wetting beams suggesting that a raindrop energy harvesting device may be more efficient if it has a hydrophilic surface. Finally, the maximum deflection of a beam from droplet impact is found to be due to a transfer of momentum and the static weight of the drop.

From a kinematic study and analogous physical experiment mimicking lapping dogs we found that dogs maximize drinking volume per lap by curling the tongue and timing the bite to occur when or before a water column pinches off from the tongue. From the physical experiment we can identify the time a water column pinches off from an accelerating column as well as the time maximum volume occurs. This study also explains that the difference between the generally clean and gentle lapping of a cat and the messy lapping of a dog is due to the large surface area and accelerations of the dog tongue. Lastly, it was found that dogs and cats have the same drinking frequency scaling with weight ($f \sim M^{-1/6}$).

We found that bats drink on the wing by dragging the tongue or bottom jaw across the water surface thereby splashing water into the mouth that it later swallows. About 50% of drinking attempts bats will drag just the tongue across the surface while it submerges much of its bottom jaw the other 50% of drinking attempts. Bats also change their wing pattern to avoid hitting the water surface. This wing pattern is much less efficient than what is used for regular straight flight.

We found that the wavelength of a crown splash instability produced by a rounded rod impact on a fluid bath can be predicted using a combination of Rayleigh-Plateau and Rayleigh-Taylor instability theory. There are also three types of splashes that occurred when the rod impacted the liquid surface: a capillary wave that gets pushed away, a jet rises up the side and forms a crown splash, and a crown splash in which many micro-droplets are ejected. The behaviors depend on the Weber, Reynolds, and Froude numbers of the rod impact.

Finally, the dynamics of squeezed fluids were investigated. We were able to predict the

trajectory of the rim as it is ejected from two circular squeezing plates. A fluid sheet was formed, a rim grew on the sheet, and then eventually broke into droplet. We were able to predict the instability wavelength using Rayleigh-Plateau instability theory.

7.2 Future Directions

Possible future directions for the droplet cantilever study include droplet bouncing on a hydrophobic elastic surface. It was found, but not reported in detail, that at certain beam stiffnesses droplets would bounce very high or very little on the beam. This behavior was due to the timescale of droplet and beam vibration being comparable. Large bounce heights occurred when the droplet reached maximum spreading factor when the beam was starting to travel back upwards. The droplet retracted and jumped off of the beam as it was traveling upwards making a diving board or trampoline for the droplet. Droplet bouncing could have implications in a raindrop energy harvesting mechanism.

In the dog drinking study the role of the tongue scoop should be investigated further. It is possible this scooping behavior has a positive effect on drinking even if the dog does not drink the scooped water. The scooped water may travel around the tongue and continue to feed the water column, thus delaying pinch-off. In the study domestic cats were compared to dogs, however, there is no detailed kinematic data for lapping in large cats (lions, tigers, etc.). It is possible these animals lap in a regime similar to dogs rather than small domestic cats. A kinematic study on large cat lapping would have a significant impact on our understanding

of lapping animals.

In bats, it is still unclear exactly how much drag is experienced when the tongue and mouth are dragged across the surface of water. To get further insight, a model of the mouth of the bat can be made, attached to a force sensor, and dragged across water to determine the exact forces a bat experiences when it drinks. Additionally, a systematic study of the splash formed by a tongue and jaw shaped object could help identify the best configuration for maximizing water splash into the mouth. All of these results can be used to help design an air vehicle capable of sampling bodies of water on the fly.

The exact mechanism causing finger instabilities to merge as liquid moves over a surface is still not yet known. Finger merging has been seen when a drop spreads out over a surface and in our case where a film moves axially over a cylindrical surface. In our case, it is possible merging is caused by surface tension and viscous effects. Behavior of the interface has been described as similar to the natural oscillations of a spring [59] and should be investigated further. Additionally, it would be useful to develop a model to predict the lamella length over time. The length likely depends on some combination of volume conservation and viscous drag and dissipation.

In future squeezing studies, we will continue to investigate the dependence on the diameter or shape of the plates. At the beginning of our experiment, we tested using rectangular shaped blocks and noticed that the control of initial fluid thickness on large circular or rectangular plates is rather difficult. It may also be possible that different shapes could allow for tuning of the instability wavelength along with other fluid parameters.

Bibliography

[1] J.A.W.M. Weijnen, Licking behavior in the rat: measurement and situational control of licking frequency. *Neurosci. Biobehav. Rev.* **22**(6), 1998.

[2] H.C. Bennet-Clark, Negative pressures produced in the pharyngeal pump of the blood sucking bug, Rodnius prolixus. *J. Exp. Biol.* **40**(1), 1963.

[3] H. Berkhoudt, K.V. Kardong, G.A. Zweers, Mechanics of drinking in the brown tree snake, *Boiga irregularus. Zoology* **98**(2), 1995.

[4] W. Kim, T. Gilet, J.W.M. Bush, Optimal concentration in nectar feeding. *PNAS* **108**(40), 2011.

[5] A. Rico-Guevara, M.A. Rubega, The hummingbird tongue is a fluid trap, not a capillary tube. *PNAS* **108**(23), 2011.

[6] J.G. Kingsolver, T.L. Daniel, On the mechanics and energetics of nectar feeding. *J. Theor. Biol.* **76**(2), 1979.

[7] M. Prakash, D. Quéré, J.W.M. Bush, Surface tension transport of prey by feeding shorebirds: the capillary ratchet. *Science* **320**(5878), 2008.

[8] W. Kim, J.W.M. Bush, Natural drinking strategies. *J. Fluid Mech.* **705**(1), 2012.

[9] A.J. Thexton, A.W. Crompton, R.Z. German, Transition from suckling. *J. Exp. Zool.* **280**(5), 1998.

[10] A.J Thexton, J.D. McGarrick, Tongue movement of the cat during lapping. *Arch. Oral Biol.* **33**(5), 1988.

[11] P. Reis, S. Jung, J.M Aristoff, R. Stocker, How cats lap: water uptake by Felis catus. *Science* **330**(6008), 2010.

[12] A. W. Crompton, C. Musinsky, (2011) How dogs lap: ingestion and intraoral transport in Canis familiaris. *Biol. Lett.* **11**(7), 2011.

[13] G.J. Amador, Y. Yamada, M. McCurley, D.L. Hu, Splash-cup plants accelerate raindrops to disperse seeds, *J. R. Soc. Interface* **10**(79), 2012.

[14] E. Buskey, P. Lenz, D. Hartline, Escape behavior of planktonic copepods in response to hydrodynamic disturbances: high speed video analysis. *Mar. Ecol. Prog. Ser.* **235**(01718630), 2002.

[15] R.J. Waggett, E.J. Buskey, Calanoid copepod escape behavior in response to a visual predator. *Mar. Biol.* **150**(4), 2007.

[16] B.J. Gemmell, H. Jiang, J.R. Strickler, E.J. Buskey, Plankton reach new heights in effort to avoid predators. *Proc. R. Soc. B* **279**(1812), 2012.

[17] J.W. Glasheen, T.A. McMahon, Size-dependence of water-running ability in basilisk lizards (Basiliscus basiliscus). *J. Exp. Biol.* 199(12),1996.

[18] J.W.M. Bush, D.L. Hu, Walking on water: biolocomotion at the interface. *Ann. Rev. Fluid Mech.* **38**(1), 2006.

[19] C. Gans, The process of skittering in frogs. *Ann. of Zoology* **12**(2), 1976.

[20] T. Gilet, J.W.M. Bush, The fluid trampoline: Droplets bouncing on a soap film, *J. Fluid Mech.* **625**(167), 2009.

[21] K. Lüling, The Archer fish. *Sci. Am.* **209**(1), 1963.

[22] P. Gerullis, S. Schuster, Archerfish actively control the hydrodynamics of their jets. *Curr. Biol.* **24**(18), 2014.

[23] J.W. Glasheen, T.A. McMahon, Size-dependence of water-running ability in basilisk lizards (Basiliscus basiliscus). *J. Exp. Biol.* **199**(12), 1996.

[24] R.M. Alexander, Principles of Animal Locomotion (Princeton University Press, Princeton, NJ, 2003).

[25] S. Greif, and B.M. Siemers, Innate recognition of water bodies in echolocating bats. *Nature Comm.* **1**(197), 2010.

[26] J.T. Emlen Jr., Social behavior in nesting cliff swallows, *The Condor* **54**(4), 1952.

[27] J.G. Kingsolver, T.L. Daniel, Mechanical determinants of nectar feeding strategy in hummingbirds: energetics, tongue morphology, and licking behavior. *Oecologia* **60**(2), 1983.

[28] W. Kim, T. Gilet, J.W.M. Bush, Optimal concentrations in nectar feeding. *PNAS* **108**(40), 2011.

[29] T.A. McMahon, J.T. Bonner, On Size and Life. (Scientific American Library, 1983)

[30] S.J. Lee, B.H. Kim, J.Y. Lee, Experimental study on the fluid mechanics of blook sucking in the proboscis of a female mosquito. *J. Biomech.* **42**(7), 2009.

[31] N.J. Morrison, J. Richardson, L. Dunn, R.L. Pardy, Respiratory muscle performance in normal elderly subjects and patients with COPD. *Chest* **95**(1), 1989.

[32] J.B. West, Snorkel breathing in the elephant explains the unique anatomy of its pleura. *Respir. Physiol.* **126**(1), 2001.

[33] D. Monaenkova, M.S. Lehnert, T. Andrukh, C.E. Beard, B. Rubin, A. Tokarev, W.K. Lee, P.H. Adler, K.G. Kornev, Butterfly proboscis: combining a drinking straw with a nanosponge facilitated diversification of feeding habits. *J. R. Soc. Interface* **9**(69), 2012.

[34] W. Kim, F. Peaudecerf, M.W. Baldwin, J.W.M. Bush, The hummingbirds tongue: a self-assembling capillary syphon. *Proc. Roy. Soc. B* **282**(1814), 2012.

[35] B.M. vonHoldt, et al., Genome-wide SNP and haplotype analyses reveal a rich history underlying dog domestication. *Nature* **464**(1), 2010.

[36] J.A. Walker, Estimating velocities and accelerations of animal locomotion: a simulation experiment comparing numerical differentiation algorithms. *J. Exp. Biol.* **201**(7), 1998.

[37] E.F. Adolph, Measurements of water drinking in dogs. *Am. J. Physiol.* **125**(1), 1938.

[38] M.W. Westneat, A biomechanical model for analysis of muscle force, power output, and lower jaw motion in fishes. *J. Theor. Biol.* **223**(3), 2003.

[39] K.T. Bates, P.L. Falkingham, Estimating maximum bite performance in Tyannosaurus rex using multi-body dynamics. *Biol. Lett.* **8**(4), 2012.

[40] L. Vincent, L. Duchemin, E. Villermaux, Remnants from fast liquid withdrawal. *Phys. Fluids* **26**(3), 2014.

[41] D. Fukui, M. Murakami, T. Aoi, Effect of emergent aquatic insects on bat foraging in a riparian forest. *J. Anim. Ecol.* **75**(6), 2006.

[42] A.M. Boonman, M. Boonman, F. Bretschneider, W.A. van de Grind, Prey Detection in Trawling Insectivorous Bats: Duckweed Affects Hunting Behaviour in Daubenton's Bat, Myotis daubentonii, Behav. Ecol. Sociobiol. **44** (2), 1998.

[43] B. Li, L. Heng, K. Kser, M. Pollefeys, A multiple camera system calibration toolbox using a feature descriptor-based calibration pattern. In International Conference on Intelligent Robots and Systems (IROS), 2013.

[44] M.J. Bender, H.G. McClelland, G. Bledt, A. Kurdila, T. Furukawa, R. Mueller, Trajectory estimation of bat flight using a multi-view camera system. *AIAA SciTech: Modeling and Simulation Technologies Conference, AIAA*, 2015.

[45] H.D.J.N. Aldridge, Flight kinematics and energetics in the little brown bat, Myotis lucifrcgcls (Chiroptera: Vespertilionidae), with reference to the influence of ground effect. *J. Zool. Lond.* **216**, 1988.

[46] G.K. Taylor, R.L. Nudds, A.L.R. Thomas, Flying and swimming animals cruise at a Strouhal number tuned for high power efficiency. *Nature* **425**(6959), 2003.

[47] W. Johnson, S.R. Reid, Ricochet of spheres off water. *J. Mech. Eng. Sci.* **17**(2), 1975.

[48] M. Greenhow, W. Lin, Nonlinear free surface effects: Experiments and theory, M.I.T. Dept. of Ocean Engineering, Rept. No. 83-19, 1983.

[49] M. Greenhow, Wedge entry into initially calm water, *Appl. Ocean. Res.* **9**(4), 1987.

[50] A.A. Korobkin, A. Iafrati, Jetting by floating wedge impact. *Proc. 19th Intern. Workshop on Water Waves and Floating Bodies*, 01-01-2004.

[51] S. Abrate, Hull Slamming. *Appl. Mech. Rev.* **64**(6), 2011.

[52] L. Bocquet, C. Clanet, The mystery of the skipping stone. *Phys. World* **19**(2), 2004.

[53] C. Clanet, F. Hersen, L. Bocquet, Secrets of successful stone-skipping. *Nature* **427**(6969), 2006.

[54] C. Duez, C. Ybert, C. Clanet, L. Bocquet, Making a splash with water repellency. *Nat. Phys.* **3**, 2007.

[55] A. Iafrati, A.A. Korobkin, Initial stage of flat plate impact onto liquid free surface. *Phys. Fluids* **16**(2214), 2004.

[56] H. Sun, O.M. Faltinsen, Water impact of horizontal circular cylinders and cylindrical shells. *Appl. Ocean Res.* **28**(5), 2006.

[57] I.R. Peters, D. van der Meer, J.M. Gordillo, Splash wave and crown breakup after disc impact on a liquid surface. *J. Fluid. Mech.* **724**(6), 2013.

[58] R.F. Allen, The role of surface tension in splashing. *J. Colloid Interface Sci.* **51**(2), 1975.

[59] S.T. Thoroddsen, J. Sakakibara, Evolution of the fingering pattern of an impacting drop. *Phys. Fluids* **10**(1359), 1998.

[60] L. Xu, W.W. Zhang, S.R. Nagel, Drop splashing on a dry smooth surface. *Phys. Rev. Lett.* **94**(184505), 2005.

[61] N. Bremond, E. Villermaux, Atomization by jet impact. *J. Fluid Mech.* **549**, 2006.

[62] A.M. Worthington, R.S. Cole, Impact with a liquid surface studied by the aid of instantaneous photography. *Proc. R. Soc. London A* **180**, 1897.

[63] R.D. Deegan, P. Brunet, J. Eggers, Complexities of splashing, *Nonlinearity* **21**(1), 2008.

[64] L.V. Zhang, P. Brunet, J. Eggers, R.D. Deegan, Wavelength selection in the crown splash. *Phys. Fluids* **22**(122105), 2010.

[65] R. Krechetnikov, G.M. Homsy, Crown-forming instability phenomena in the drop splash problem. *J. Colloid Interface Sci.* **331**(2), 2009.

[66] R. Krechetnikov, Stability of liquid sheet edges. *Phys. Fluids* **22**(092101), 2010.

[67] J.J. Charonko, P.P. Vlachos, Estimation of uncertainty bounds for individual particle image velocimetry measurements from cross-correlation peak ratio. *Meas. Sci. Tech.* **24**(6), 2013.

[68] I.V. Roisman, K. Horvat, C. Tropea, Spray impact: Rim transverse instability initiating fingering and splash, and description of a secondary spray. *Phys. Fluids* **18**(102104), 2006.

[69] T. Rabinowitz and B. Tandler, Papillary morphology of the tongue of the American chameleon: Anolis carolinensis. *Anat. Rec.* **216**(4), 1986.

[70] R. Sexton, J.A. Roberts, Cell biology of abscission, *Ann. Rev. Plant Physiol.* **33**(1146), 1982.

[71] B. Rubinstein, A.C. Leopold, The nature of leaf abscission, *Quarterly Rev. of Bio.* **39**(4), 1964.

[72] A.G. Gawadi, G.S. Avery Jr., Leaf abscission and the so-called "abscission layer," *Am. J. Botany* **37**(2) 1950.

[73] C. Neinhuis, W. Barthlott, Seasonal changes of leaf surface contamination in beech, oak, and ginkgo in relation to micromorphology and wettability, *New Phytol.* **138**(1), 1998.

[74] T.W. Brakke, W.P. Wergin, E.F. Erbe, and J.M. Harnden, Seasonal variation in the structure and red reflectance of leaves from yellow poplar, red oak, and red maple, *Rem. Sens. of Env.* **43**(2), 1993.

[75] F. Bussotti, M. Ferretti, Air pollution, forest condition and forest decline in Southern Europe: an overview, *Env. Poll.* **101**(1), 1998.

[76] M.D. Thomas, Effects of air pollution on plants, *Air Poll.* **46**, 1961.

[77] M. Turunen, M. Huttunen, A review of the response of epicuticular wax of conifer needles to air pollution, *J. Env. Qual.* **19**(1), 1990.

[78] J. Burkhardt, S. Pariyar, Particulate pollutants are capable to 'degrade' epicuticular waxes and to decrease the drought tolerance of Scots pine (Pinus sylvestris), *Env. Poll.* **184**, 2014.

[79] G.H. Tomlinson, Air pollutants and forest decline, *Env. Sci. Technol.* **17**(6), 1983.

[80] E.A. Baker, G.M. Hunt, Erosion of waxes from leaf surfaces by simulated rain, *New Phytol.* **102**(1), 1986.

[81] J. Wolfenden, T.A. Mansfield, Physiological disturbances in plants caused by air pollutants, *Proc. R. Soc. Edinburgh B* **97**, 1990.

[82] R. Blossey, Self-cleaning surfaces – virtual realities, *Nat. Mat.* **2**(5), 2003.

[83] D.W. Bechert, M. Bruse, W. Hage, R. Meyer, Fluid mechanics of biological surfaces and their technological application, *Naturwissenschaften* **87**(4), 2000.

[84] W. Barthlott, C. Neinhuis, Purity of the sacred lotus, or escape from contamination in biological surfaces, *Planta* **202**(1), 1997.

[85] K.J. Niklas, Research review: a mechanical perspective on foliage leaf form and function, *New Phytol.* **143**(1), 1999.

[86] A. Yarin, Drop impact dynamics: splashing, spreading, receding, bouncing..., *Ann. Rev. Fluid Mech.* **38**, 2006.

[87] E. Villermaux, Fragmentation, *Ann. Rev. Fluid Mech.* **39**, 2007.

[88] L. Xu, Liquid drop splashing on smooth, rough, and textured surfaces, *Phys. Rev E* **75**(5), 2007.

[89] I.V. Roisman, E. Berberovic, C. Tropea, Inertia dominated drop collisions. 1. On the universal flow in the lamella, *Phys. Fluids* **21**(052103), 2009.

[90] J. Fukai, Y. Shiiba, T. Yamamoto, O. Miyatake, D. Poulikakos, C.M. Megaridis, Z. Zhao, Wetting effects on the spreading of a liquid droplet colliding with a flat surface: Experiment and modeling, *Phys. Fluids* **7**(2), 1995.

[91] R. Guigon, J.J. Chaillout, T. Jager, G. Despesse, Harvesting raindrop energy: theory, *Smart Mat. Struct.* **17**(015039), 2008.

[92] R. Guigon, J.J. Chaillout, T. Jager, G. Despesse, Harvesting raindrop energy: experimental study, *Smart Mat. Struct.* **17**(015038), 2008.

[93] P.V. Biswas et al. in *Harvesting raindrop energy in Bangladesh*, Proceedings of the International Conference on Mechanical Engineering, Dhaka, Bangladesh, 2009.

[94] G.J. Amador, Y. Yamada, M. McCurley, D.L. Hu, Splash-cup plants accelerate raindrops to disperse seeds, *J. R. Soc. Interface* **10**(79), 2012.

[95] T. Gilet, L. Bourouiba, Rain-induced ejection of pathogens from leaves: revisiting the hypothesis of splash-on-film using high-speed visualization, *Int. Comp. Biol.* **54**(5), 2014.

[96] R.E. Pepper, L. Courbin, H. Stone, Splashing on elastic membranes: The importance of early-time dynamics, *Phys. Fluids* **20**(082103), 2008.

[97] T. Gilet, J.W.M. Bush, The fluid trampoline: droplets bouncing on a soap film, *J. Fluid Mech.* **625**, 2009.

[98] D. Soto, A.B. De Larivière, X. Boutillon, C. Clanet, D. Quéré, The force of impacting rain, *Soft Matter* **10**(4929) 2014.

[99] S. Mangili, C. Antonini, M. Marengo, A. Amirfazli, Understanding the drop impact phenomenon on solf PDMS substrates, *Soft Matter* **8**(10045), 2012.

[100] R. Rioboo, M. Voué, H. Adão, J. Conti, A. Vaillant, D. Seveno, J. De Coninck, Drop impact of soft surfaces: beyond the static contact angles, *Langmuir* **26**(7), 2009.

[101] E. Villermaux, B. Bossa, Single-drop fragmentation determines size distribution of raindrops, *Nature Phys.* **5**, 2009.

[102] C.W. Ulbrich, IEEE Trans. A review of the differential oscillation of inviscid drops and bubbles, *Geoscience Rem. Sens.* **24**(6), 1986.

[103] L. Meirovitch, *Fundamentals of Vibrations* (McGraw-Hill, New York, 2001), pp. 419-420.

[104] R. L. Chazdon, The costs of leaf support in understory palms: economy versus safety, *Am. Soc. Naturalists* **127**(1), 1986.

[105] J. E. Mates, T. M. Schutzius, I.S. Bayer, J. Qin, D. E. Waldroup, C. M. Megaridis, Water-based superhydrophobic coatings for nonwoven and cellulosic substrates, *Ind. Eng. Chem. Res.* **53**(1), 2014.

[106] J. E. Mates, T. M. Schutzius, J. Qin, D. E. Waldroup, C. M. Megaridis, The fluid diode: tunable unidirectional flow through porous substrates, *ACS Appl. Mater. Interfaces* **6**(15), 2014.

[107] L. Gao, T. J. McCarthy, Contact angle hysteresis explained, *Langmuir* **22**(14), 2006.

[108] D. Quéré, Wetting and roughness, *Annu. Rev. Mater. Res.* **38**(71), 2006.

[109] K. Naeli, O. Brand, Dimensional considerations in achieving large quality factors for resonant silicon cantilevers in air, *J. Appl. Phys.* **105**(014908), 2009.

[110] H. Hosaka, K. Itao, S. Kuroda, Damping characteristics of beam-shaped micro-oscillators, *Sens. Actu. A* **49**(1), 1995.

[111] L.D. Laundau, E.M. Lifshitz, *Fluid Mechanics* (Pergamon, London, 1959), p 95.

[112] P.G. Simpkins, V.J. Kuck, On air entrainment in coatings *J. Coll. Int. Sci.* **263**(2), 2003.

[113] G.G. Nasr, A.J. Yule, L. Bendig L, *Industrial sprays and atomization: design, analysis and applications*, Springer Verlag, London, 2002.

[114] P.S. Shah, L.T. Fan, I.C. Kao, L.E. Erickson, Modeling of Growth Processes with Two Liquid Phases: A Review of Drop Phenomena, Mixing, and Growth *Adv. Appl. Microbiol.* **15**, 1972.

[115] E. Villermaux, B. Bossa, Single-drop fragmentation determines size distribution of raindrops, *Nature Physics* **5**, 2009.

[116] H.E. Edgerton, *Stopping time: the photographs of Harold Edgerton*, Abrams, New York, 1977.

[117] R. Rioboo, C. Bauthier, J. Conti, M. Voue, J. De Coninck, Experimental investigation of splash and crown formation during single drop impact on wetted surfaces *Experiments in fluids* **35**(6) 2003.

[118] S.T. Thoroddsen,T.G. Etoh, K. Takehara, Crown breakup by Marangoni instability, *J. Fluid. Mech.* **557**, 2006.

[119] Z. Levin, V. Hobbs, Splashing of Water Drops on Solid and Wetted Surfaces: Hydrodynamics and Charge Separation *Phil. Tran. R. Soc. Lon. A.* **269** (1200), 1871.

[120] A.L. Yarin, D.A. Weiss, Impact of drops on solid surfaces: self-similar capillary waves, and splashing as a new type of kinematic discontinuity, *J. Fluid. Mech.* **283**, 1995.

[121] T.T. Truscott, A.H. Techet, Water entry of spinning spheres *J. Fluid Mech.* **625**, 2009.

[122] G.I. Taylor, The Dynamics of Thin Sheets of Fluid. I. Water Bells, *Proc. R. Soc. A.* **253**(1274), 1959.

[123] G.I. Taylor, The Dynamics of Thin Sheets of Fluid. II. Waves on Fluid Sheets, *Proc. R. Soc. A* **253**(1274), 1959.

[124] G.I. Taylor, The Dynamics of Thin Sheets of Fluid. III. Disintegration of Fluid Sheets, *Proc. R. Soc. A* **253**(1274) 1959.

[125] C. Clanet, Dynamics and stability of water bells *J. Fluid. Mech.* **430**, 2001.

[126] J. Aristoff, C. Lieberman, E. Chan, J.W.M. Bush, Water bell and sheet instabilities, *Phys. Fluids* **18**(091109), 2006.

[127] C. Clanet, Waterbells and Liquid Sheets, *Annu. Rev. Fluid Mech.* **39**, 2007.

[128] A.M. Worthington, *A study of splashes*,(Longmans, Green, and Co., London, 1908).

[129] A.M. Worthington, Impact with a Liquid Surface, Studied by the Aid of Instantaneous Photography *Phil. Tran. R. Soc. Lon. A.* **189**, 1897.

[130] A.M. Worthington, One the forms assumed by drops of liquids falling vertically on a horizontal plate, *Proc. Roy. Soc. Lon.* **25**, 1876.

[131] S. Chandra, C.T. Avedisian, On the Collision of a Droplet with a Solid Surface, *Proc. Math. Phys. Sci.* **432**(1884), 1991.

[132] C. Josserand, S. Zaleski, Droplet splashing on a thin liquid film, *Phys. Fluids* **15**, 2003.

[133] E. Villermaux, B. Bossa, Drop fragmentation on impact, *J. Fluid Mech.* **668**, 2011.

[134] G. Juarez, T. Gastopoulos, Y. Zhang, M.L. Siegel, P. E. Arratia, Splash control of drop impacts with geometric targets, *Phys. Rev. E* **85**(026319), 2012.

[135] C. Clanet, E. Villermaux, Life of a smooth liquid sheet, *J. Fluid Mech.* **462**, 2002.

[136] *CRC Handbook of Physics and Chemistry, 72 ed.*, CRC Press, Boca Raton, USA, 1991.

[137] G.K. Batchelor, *An introduction to fluid dynamics*, Cambridge Univ. Press, New York, 1967.

[138] Experimental measurement with a force sensor shows the linear relation between the impact force and the disk velocity (Impact force (dyne) = 7.27×10^{-1} V_{disk} (cm/s) with $R^2 = 0.736$).

[139] R.B. Bird, W.E. Stewart, E.N. Lightfoot, *Transport Phenomena, 2nd ed.*, John Wiley and Sons, New York, 2001.

[140] R. Clift, J. R. Grace, M. E. Weber, (*Bubbles, Drops, and Particles*, Dover Press, New York, 1978.)

[141] L. Rayleigh, On the capillary phenomena of jets, *Proc. Roy. Soc. Lon.* **29**,1879.

[142] J. Eggers, E. Villermaux, Physics of liquid jets, *Rep. Prog. Phys.* **71**(036601), 2008.

[143] C. Weber, Z. Angew. Zum Zerfall eines Flüssigkeitsstrahles, *Math. Mech.*, **11**(2), 1931.

[144] M. Song, G. Tryggvason, The formation of thick borders on an initially stationary fluid sheet, *Phys. Fluids* **11**, 1999.

[145] S. Gart, J. Mates, C.M. Megaridis, S. Jung, Droplet impacting a cantilever: A leaf-raindrop system. *Phys. Rev. Applied* **3**(044019), 2015.

[146] S. Gart, J.J. Socha, P.P. Vlachos, S. Jung, Dogs lap using acceleration-driven open pumping. *Proc. Nat. Acad. Sci.* **112**(52), 2015.

[147] S. Gart, B. Chang, B. Slama, R. Goodnight, S.H. Um, S. Jung, Dynamcis of squeezing fluids: clapping wet hands. *Phys. Rev. E* **88**(023007), 2013.